# Image Based Analysis and Modeling of the Detailed Cardiac Ventricular Anatomy

Bruno Paun

TESI DOCTORAL UPF / ANY 2017

DIRECTOR DE LA TESI

Dr. Bart Bijnens and Dr. Constantine Butakoff

Department of Information and Communication Technologies

# Acknowledgments

The research leading to these results has received funding by EU FP7 for research, technological development and demonstration under grant agreement VP2HF (no. 611823), Spanish Ministry of Economy and Competitiveness (grant TIN2011-28067, TIN2014-52923-R, the Maria de Maeztu Units of Excellence Programme MDM-2015-0502) and FEDER. B. Paun is supported by the grant FI-DGR 2014 (2014 FI B01238) from the Generalitat de Catalunya.

The Dicom datasets used in Chapter 3 and 4 were provided by the Visible Heart® Laboratory (University of Minnesota), they were obtained by MRI scanning perfusion fixed hearts that were graciously donated by the organ donors and their families through LifeSource.

The High Resolution Episcopic Microscopy (HREM) datasets used in Chapter 5 were provided by Dr. T. J. Mohun from the Francis Crick Institute, London.

# Abstract

The role of trabeculations and their normal morphological expression in the human heart is still unclear. It is known that, at adulthood, the amount of trabeculae increases from the base to apex and that they are absent along the outflow tract towards the aorta in the left ventricle and toward the pulmonary vein in the right ventricle. The influence of the excessive trabeculations (Left Ventricular Non-Compaction - LVNC) on cardiac function is important for clinical diagnosis and subject of many clinical studies. There are several hypotheses about their function, such as reduction of local wall stress and strain, and providing pathways of faster conduction (the Purkinje conduction system passes on top of the larger trabeculations and can also be found in the thinner structures such as false tendons). Clinical studies have shown that excessive trabeculation can cause heart failure due to diastolic and systolic dysfunction, thromboembolism and arrhythmias. Quantifying and modeling those structures could provide us insights into their function, their influence on cardiac performance and also their connection with cardiomyopathies, in particular Dilated Cardiomyopathy (DCM) and Hypertrophic Cardiomyopathy (HCM).

Imaging modalities available in clinical practice are not able to provide images of sufficient resolution suitable to capture information about detailed cardiac anatomy. Therefore, our ability to analyze them is limited to either histological studies, ex-vivo imaging and computational modeling. Recent advances in ex-vivo imaging technologies, such as magnetic resonance imaging (MRI), micro computed tomography ($\mu$CT) and high resolution episcopic microscopy (HREM), have led to an increased quality of the acquired scans and thus resulted in visibility of complex cardiac fine-scale structures such as trabeculations and small blood vessels. Such highly-detailed images are unveiling a large amount of information about the detailed cardiac structures, and most importantly, make their segmentation, analysis and translation into models feasible.

In this thesis, I present the results of my investigation into the role of cardiac trabeculations and their quantification in populational studies.

The contributions of the thesis can be summarized as follows:

- A simplified model of the trabeculated left ventricle (LV) to study the impact of trabeculations on stroke volume, strain and pump capacity of LVs of different geometries. I use this model to demonstrate how trabeculations can help the cardiac ventricles to be efficient and adapt to changes in loading conditions.
- A simple as well as a more elaborate method for geometry independent parametrization of the detailed cardiac left and right ventricular anatomy to facilitate population studies of cardiac anatomy and function. These methods allow establishing a one-to-one mapping between the cardiac ventricles of different individuals.
- A framework for convenient visualization and statistical analysis of the trabeculations, both longitudinally over time as well as transversally over individuals in a population. This framework uses a ventricular parameterization approach to consistently define a subdivision of the myocardium into 3D regions, where volumetric measures can be readily calculated.
- A longitudinal analysis of the cardiac trabeculations in a mouse embryo at different gestational stages. To the best of my knowledge this is the first study to quantify the regional progression of the myocardial trabeculations. Additionally I extend the fractal analysis, commonly carried out in cardiac 2D slices, to 3D, and propose new measures of myocardial complexity: regional myocardial volume and area.

# Resumen

El papel de las trabéculas cardíacas y su morfología normal en el corazón humano es todavía desconocido. Es sabido que en la etapa adulta la cantidad de trábeculas aumenta desde la base al ápex, no se encuentra a lo largo del tracto de salida hacia la aorta en el ventrículo izquierdo ni hacia la vena pulmonar en el ventrículo derecho. La influencia de una excesivas trabéculas (LVNC) en la función cardíaca es importante para el diagnóstico clínico y es objeto de múltiples investigaciones clínicas. Existen varias hipótesis sobre su función, como la reducción del estrés y la deformación local de la pared, o su capacidad de proporcionar una rápida conducción eléctrica (el sistema de conducción de Purkinje pasa por encima de las trabéculas más grandes y también puede encontrarse en estructuras más delgadas como falsos tendones). Estudios clínicos han demostrado que la trabeculación excesiva puede causar insuficiencia cardíaca debido a disfunción diastólica y sistólica, tromboembolismo y arritmias. El modelado y cuantificación de estas, nos puede dar una idea de su función, su influencia en el rendimiento cardíaco y también su conexión con cardiomiopatías, en particular la cardiomiopatía dilatada (DCM) y la miocardiopatía hipertrófica (CMH).

Las modalidades de imagen disponibles en la práctica clínica son incapaces de proporcionar imágenes con resolución suficiente como para captar información detallada de la anatomía cardíaca. Por lo tanto, nuestra capacidad para analizarlos se limita a estudios histológicos, imágenes ex-vivo y al modelado computacional. Los avances en las tecnologías de imagen ex vivo, como la resonancia magnética (MRI), la micro tomografía computarizada ($\mu$CT) y la microscopía episcópica de alta resolución (HREM), han aumentado considerablemente la calidad de las imágenes adquiridas. Estas modalidades permiten adquirir imágenes con un nivel de detalle suficiente como para distinguir y analizar las estructuras cardiacas finas como trabéculas y vasos sanguíneos pequeños. Estas imágenes altamente detalladas revelan una gran cantidad de información sobre dichas estructuras cardíacas y, lo que es más importante, hacen factible su segmentación, análisis y traspaso a modelos.

En esta tesis, explicaré los resultados de mi investigación sobre el papel de las trabéculas cardíacas y su cuantificación en estudios poblacionales. Las contribuciones de la presente tesis son los siguientes:

- Un modelo simplificado del ventrículo izquierdo trabeculado para estudiar el impacto de las trabéculas sobre el volumen, la deformación y el gasto cardíaco de los ventrículos con diferentes geometrías. Este modelo ha sido utilizado para demostrar como las trabéculas pueden ayudar a los ventrículos cardíacos a ser eficientes y adaptarse a los cambios en condiciones de carga.

- Un método simplificado, así como un método más complejo para la parametrización independiente de la geometría cardíaca detallada de los ventrículos izquierdo y derecho para facilitar los estudios poblacionales de la anatomía y la función cardíaca. Estos métodos permiten establecer una correlación uno a uno entre los ventrículos cardíacos de diferentes individuos.

- Un framework para la visualización cómoda y el análisis estadístico de las trabeculaciones, tanto longitudinalmente a lo largo del tiempo como transversalmente sobre individuos en una población. Este framework utiliza mi parametrización ventricular para definir consistentemente una subdivisión del miocardio en regiones 3D, donde las medidas volumétricas pueden calcularse fácilmente.

- Un análisis longitudinal de las trabéculas cardíacas en un embrión de ratón en diferentes etapas gestacionales. Según mi saber, este es el primer estudio para cuantificar por regiones la progresión de las trabeculaciones miocárdicas. Además, el análisis fractal, comunmente realizado en cortes 2D ha sido extendido a 3D, y nuevas medidas de la complejidad miocárdica tales como volumen y área regional del miocardio han sido así mismo propuestas.

# Preface

The following chapters represent the work done along the process of my PhD. None of this would have been possible without support of my supervisors Dr. Bart Bijnens and Dr. Constantine Butakoff. I would like to express my gratitude to them for their guidance and support. I would like to thank Dr. Oscar Camara, who together with my supervisors, have seen a potential in me and accepted me to be a part of PhySense research group and making this journey of obtaining a PhD possible.

I would like to thank Dr. Andrew Cook, my supervisor during my research stay at UCL Institute of Cardiovascular Science in London, for giving me opportunity to be part of his research group and, together with Mr. Vi Tran, providing me an hands-on insights of cardiac morphology on their base of real specimens.

I would also like to thank all my coauthors, my work and office colleagues for contributing to my research. And last but not least, I would like to thank my family and friends, who stood beside me and gave me unconditional support when the times were hard.

# Contents

# List of Figures

# List of Tables

# Acronyms

| | |
|---|---|
| LV | Left Ventricle |
| RV | Right Ventricle |
| LVNC | Left Ventricular Non-Compaction |
| CHD | Congenital Heart Disease |
| DCM | Dilated Cardiomyopathy |
| HCM | Hypertrophic Cardiomyopathy |
| MRI | Magnetic Resonance Imaging |
| $\mu$CT | Micro Computed Tomography |
| CMR | Cardiac Magnetic Resonance |
| HREM | High Resolution Episcopic Microscopy |
| LVEF | Left Ventricular Ejection Fraction |
| Nt-ProBNP | N-terminal Prohormone of Brain Natriuretic Peptide |
| SV | Stroke Volume |
| FD | Fractal Dimension |
| NCC | Non-Compaction Cardiomyopathy |
| ES | End Systole |
| ED | End Diastole |
| EDV | End-Diastolic Volume |
| ESV | End-Systolic Volume |
| CO | Cardiac Output |
| HR | Heart Rate |

| | |
|---|---|
| CGI | Computer Generated Imagery |
| CMRI | Cardiac Magnetic Resonance Imaging |
| TPS | Thin Plate Splines |
| AHA | American Heart Association |
| VTK | Visualization Toolkit |
| 2D | Two-Dimensional |
| 3D | Three-Dimensional |
| E | Embryonic Day |
| GA | Gestational Age |
| LAX | Long Axis |

# Chapter 1

# GENERAL INTRODUCTION

## 1.1 Cardiac Trabeculations

The ventricular cavities of the heart are characterized by the presence of numerous myocardial protrusions into their lumen, known as cardiac trabeculations (*trabeculae carneae*). The trabeculations represent fine-scale endocardial structures, which protrude from the inner ventricular walls of all the cardiac chambers. There is a visible difference in the morphology and extent of the trabeculations between the different chambers (Wessels and Sedmera, 2003). In the left ventricle of the heart, the trabeculations are relatively thin, while in the right ventricle, they are more pronounced or coarse, as we can see from Fig. 1.1(a). Within the same ventricle, they also differ greatly in their morphology, with bigger trabeculations that are attached to the inner ventricular wall by their whole length forming prominent ridges, as can be seen in Fig. 1.1(b), while others are thin and mutually interconnected, forming a complex meshwork of structures, such as those dominant in the apical part of the ventricles (Fig. 1.1(c)). Their pattern is ventricle and species specific and differs greatly between these - we could say that they are like fingerprints of a heart. The pattern they form, and their extent, depend on the outcome of the process of compaction of myocardium during embryonic stage.

In addition to the trabeculations, there are other endocardial structures

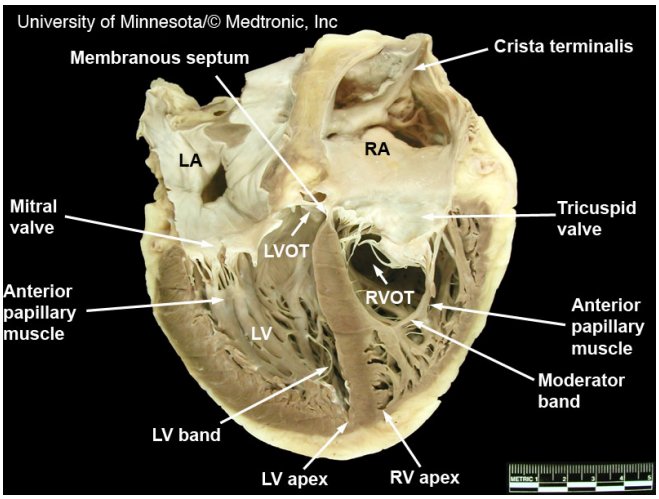


(a) Anterior half of coronal slice of the human heart.

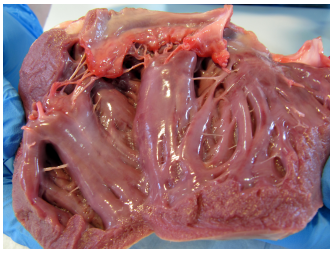

(b) Big trabeculations.

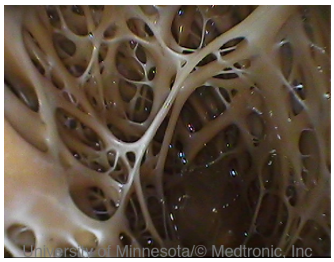


(c) Thin trabeculations.

Figure 1.1: Images of the anterior part of the coronal two chamber slice of the human heart and different trabecular morphologies of a heart. Fig. (a), (c) courtesy of Atlas of Human Cardiac Anatomy - University of Minnesota.

present inside the ventricular cavities. The most pronounced structures would be the papillary muscles (*musculi papillares*) projecting from inner ventricular walls with their bases at the wall of the ventricles, while their apices are attached to the leaflets of the mitral (bicuspid) valve in the left ventricle (LV) and tricuspid valve in the right ventricle (RV) via tendinous chords (*chordae tendineae*). Their function is to prevent prolapse towards the atria of the tricuspid valve leaflets in the RV and mitral valve leaflets in the left ventricle (LV) during ventricular systole and thus prevent regurgitation of the blood. There are two papillary muscles in each ventricle: anterior and posterior. In the RV, the anterior papillary muscle is larger than the posterior, while in the LV they are roughly of the same size.

Additionally, there is a moderator band in the RV (*trabecula septomarginalis*), a band that traverses through the right ventricle. It carries Purkinje fibers, coming from the right bundle branch, to the outer wall of the ventricle and it frequently extends from the base of the anterior papillary muscle to the ventricular septum. Given its attachments to the two opposite walls, it may assist in preventing overdistension of the right ventricle (Gray, 1918).

Within the LV and RV, we can also find thin, cord-like structures that look like the tendinous chords connecting the larger trabeculations between themselves, while some may be attached to the papillary muscles. Despite of their resemblance, these structures are not really tendons, but are actually extensions of the subendocardial ventricular network of the cardiac conduction system, and are therefore called "false tendons" which can be seen in Fig. 1.1(c). They consist almost exclusively of Purkinje cells (Wessels and Sedmera, 2003).

## 1.2 Formation of Trabeculations

Until 2011, general knowledge about trabeculations and their developmental stages came from studies of fixed tissues of mouse and chick embryos done by Sedmera et al. (2000). Then, Peshkovsky et al. (2011) pub-

lished their studies of live zebrafish embryos. Optical transparency of the fish allowed them to spatially and temporarily observe trabeculations and define morphologically discrete stages of their development. The stages in zebrafish were comparable with the stages characterized in the work of Sedmera et al. (2000).

The developmental pattern of the heart is the same in all vertebrates (upper part of Fig. 1.2). During the embryogenesis, the heart develops from a simple tubular shape, starts to loop rightward, and further evolves into a complex 4-chamber organ, specialized for efficient pumping of blood. The development of a heart is naturally accompanied by the myocardial development, which is characterized by a change in the myocardial architecture. During development, myocardium goes through four distinct phases (Sedmera et al., 2000):

1. early primitive tubular heart,
2. emergence of trabeculations,
3. trabecular remodeling or myocardial compaction and
4. development of the layered spiral system of the compact myocardium.

An important step for the development of the myocardium is the formation of the trabeculations, which start to emerge along the luminal part of the apical region of a primitive heart ventricle, soon after it starts to loop. The trabeculations increase the myocardial surface area and serve to increase myocardial oxygenation and nutrient delivery trough diffusion, thus enabling the myocardium to increase its mass in absence of a coronary circulation. Before they start to compact, trabeculations can form up to $80\ \%$ of the myocardial mass in the embryonic human heart (Wessels and Sedmera, 2003).

In the following stages of the myocardium development, which coincide with the invasion of the coronary circulation, the trabecular layer starts to solidify or compact, thus increasing thickness of the compact

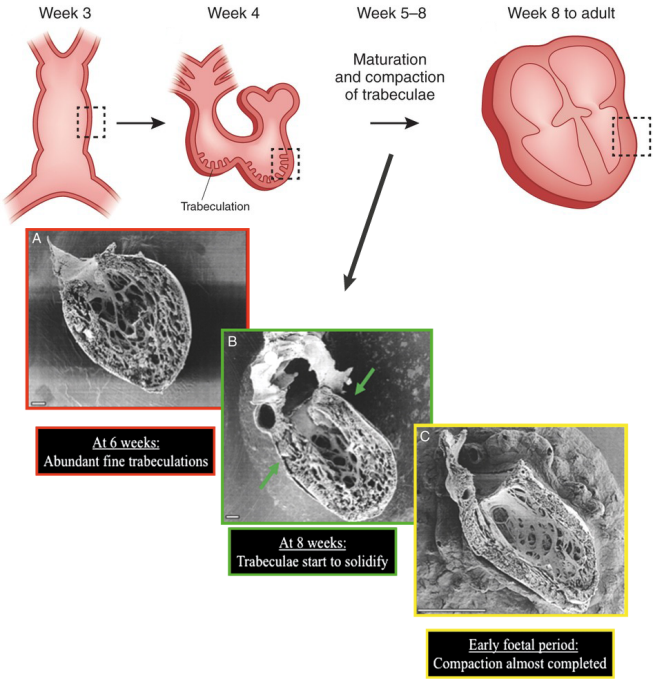


Figure 1.2: Development of a heart and the process of compaction. Image courtesy of Oechslin and Jenni (2011); Sedmera et al. (2000); Misra and Garg (2013).

layer of ventricular myocardium. The process of compaction or solidification (bottom part of Fig. 1.2) can be divided into three steps (Oechslin and Jenni, 2011):

1. appearance of abundant trabeculations,

2. beginning of trabecular remodeling (compaction) and

3. completion of compaction process.

At the third stage, the compact myocardial layer forms most of the myocardial mass. The increase of pressure inside the ventricles results

in an increase of ventricular volumes and cause a compression of the trabeculations, leading to an increase in the thickness of the compacted myocardium. The compaction process progresses from base to apex, from epicardium to endocardium and from septum to the free wall of a heart in LV (Oechslin and Jenni, 2011), and is more pronounced in the left ventricle than in the right one because of greater intracavitary pressure.

After the completion of compaction the remaining layer next to the ventricular lumen retains its trabeculations, with a pattern specific to the ventricle and species. The ventricular apex always stays trabeculated. If the process of compaction is altered and prematurely stops, the time of arrest of the compaction process determines how pronounced trabeculations will be in ventricles.

The above mentioned hypothesis of trabecular development suggests that the formation of the trabeculations is an initial step of myocardial compaction. The trabeculae undergo a process of compaction, transforming the intertrabecular spaces into capillaries, and are accompanied by the appearance of the coronary artery tree (Agmon et al., 1999; Bernanke and Velkey, 2002; Freedom et al., 2005). On the other hand, more recent studies on myocardial cell growth suggest, that after the trabeculations are formed, the cell proliferation concentrates only in the outer myocardial wall, forming the compact layer (de Boer et al., 2012).

Trabeculations can also be found in both atrial appendages at a later stage than in the ventricles. Initially, a smooth luminal surface starts roughening into a relief. Roughening coincides with an increase of the atrioventricular pressure gradient and it can thus be regarded as a means of increasing atrial contractility (Sedmera et al., 2000). The pattern of roughening forms the pectinate muscles - muscular columns running mostly parallel to each other, giving a comb-like appearance. The extent of the pectinate muscles in the appendages is a morphological marker for differentiation between the left and the right side of a heart, as they are more pronounced in the right appendage. There is a difference in extent of the pectinate muscles between species and certain parts of the atrial chambers, like the venous sinuses and the atrioventricular vestibules, always remain smooth (Sedmera et al., 2000).

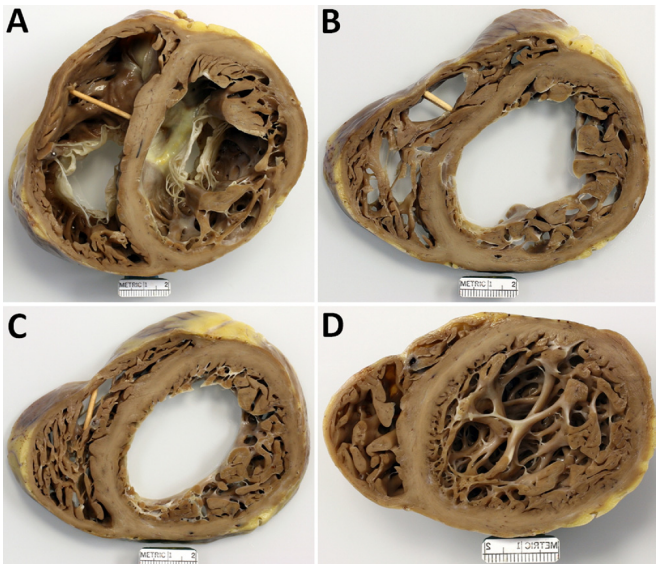


Figure 1.3: Four histological slices of a heart from a patient with LVNC: (A) basal level, (B, C) intermediate levels and (D) apical level. The non compacted portion of the left ventricular free wall is thicker than the compacted portion. Image courtesy of Roberts et al. (2011).

## 1.3 Excessive Trabeculations - Left Ventricular Non Compaction (LVNC)

The presence of prominent excessive trabeculations in the postnatal heart represent a condition, called left ventricular non-compaction (LVNC). LVNC is characterized by two layered myocardium, consisting of a thick non compacted layer (trabeculations), thin compacted layer of myocardium and large intertrabecular spaces, occurring primarily in the LV (Fig. 1.3). The exact causes of development of LVNC are still unclear, but the widely accepted hypothesis is that LVNC develops due to an arrest of the myocardial compaction process during embryogenesis.

The trabeculated appearance of myocardium was first described by Grant (1926), in the presence of congenital heart disease (CHD), and

from then on it had a variety of different names such as apical web, hypertrabeculation, spongy myocardium, spongiform cardiomyopathy, left ventricular abnormal trabeculation, non compaction syndrome of the myocardium, non compaction of ventricular myocardium, persistent myocardial sinusoids, fetal myocardium and hypertrabeculation syndrome. Chin et al. (1990) recognized the underlying arrest of the myocardial compaction process during embriogenesis and set the name that is currently used. The authors also found and described the condition in its isolated form without CHD and proposed echocardiographic diagnostic criteria for the LVNC.

At the beginning, it was thought that LVNC is a rare condition, but as the imaging modalities improved and diagnosis moved from autopsy to non invasive technologies (especially echocardiography), the excessive trabeculations were observed *in vivo* more frequently and became classified as cardiomyopathy. During the last 30 years, there was en increasing interest in this condition, which can be seen from the rapid increase of publications related to it. The diagnosis of LVNC in patients is usually carried out using echocardiography and cardiac magnetic resonance (CMR), using one of the several existing diagnostic criteria (Oechslin and Jenni, 2011; Captur et al., 2013). In general, LVNC is defined as a state when the thickness of the trabeculations (non-compacted layer) is more than twice the thickness of the underlying ventricular myocardium (compacted layer). There is a debate whether advances in imaging modalities led to a better delineation of the non-compacted myocardium, or the existing diagnostic criteria are poor and too sensitive, which leads to overdiagnosis of LVNC (Kohli et al., 2008; Captur et al., 2013).

As already mentioned, LVNC can occur in association with CHD or neuromuscular disease or as an isolated condition and its expressions are highly variable. Its clinical manifestations are ranging from the asymptomatic to heart failure due to LV ventricular systolic and diastolic dysfunction, arrhythmias and thromboembolic events (Ganame et al., 2006; Towbin, 2010; Sarma et al., 2010).

The developmental hypothesis of LVNC is currently widely accepted in literature, supported by strong evidence of abnormality in myocardial

remodeling (failure of compaction) in embryos, supported by arguments coming from studies of genetic mutations in mice, where mutations of many genes involved in key phases of myocardial remodeling during the embriogenesis resulted in the development of LVNC. However there is controversy about whether LVNC could also be acquired. Advances in molecular genetics raised the hypothesis that LVNC could be developed later in life, as it is observed in dilated cardiomyopathy (DCM) or hypertrophic cardiomyopathy (HCM), whose morphological expression is not present at birth but is acquired postnatally. Findings that patients with LVNC, DCM and HCM share similar gene mutations support the hypothesis that LVNC could be acquired later in life, but they also set the question of whether LVNC is a distinct cardiomyopathy or it is just a morphological expression shared between other cardiomyopathies (DCM, HCM).

## 1.4 Relationship Between the Trabeculation Pattern and Cardiac Function

The non-compacted myocardium can appear in association with some cardiac abnormalities such as congenital pulmonary atresia, Ebstein's anomaly, bicuspid aortic valve, corrected transposition, isomerism of left atrial appendage and ventricular septal defects (Jost et al., 2005; Friedberg et al., 2005; Lilje et al., 2006). It has also been described in association with neuromuscular disorders - Barth syndrome, Charcot-Marie-Tooth disease 1A, Melnick-Needles syndrome and nail-patella syndrome (Stöllberger and Finsterer, 2004).

Even though the main mechanism is thought to be an arrest in myocardial morphogenesis, there is no actual proof of this theory. Pronounced hypertrabeculation may be the result of various disorders. Fig. 1.5 shows some of the disorders observed with LVNC. The implications of trabeculations on global and local cardiac function are not understood yet. Some reports state that the inclusion of trabeculations in the total LV myocardium volume may increase with respect to systolic wall thickening of the

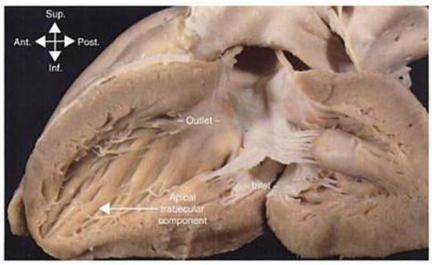


(a) Trabecular morphology in the left ventricle.

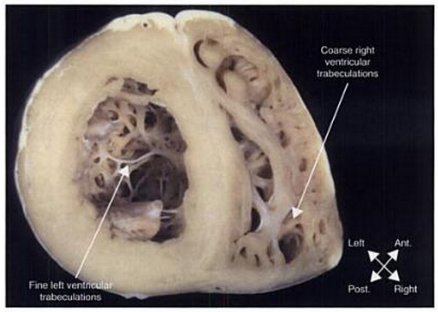


(b) Apical section of the heart showing different patterns of apical trabeculations in both ventricles.

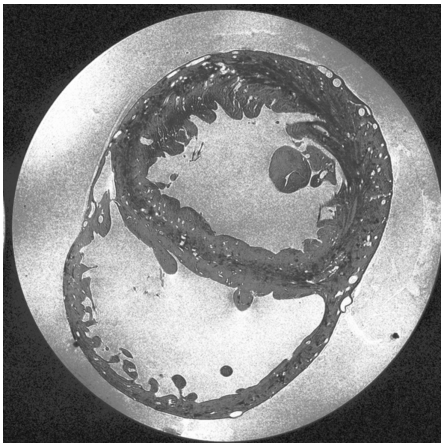

(c) Short-axis slice of Oxford rabbit dataset.

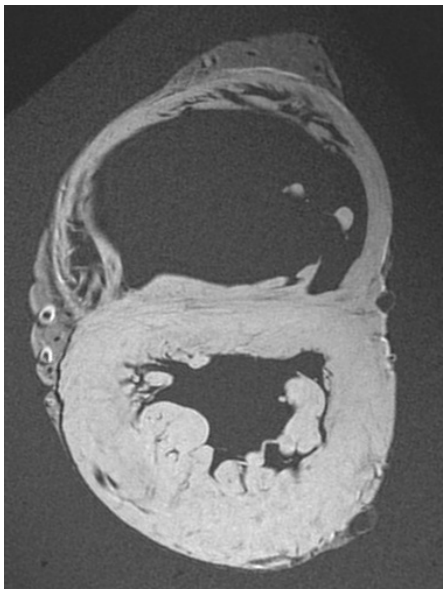

(d) Short-axis slice of cardiac atlas of Minnesota dataset.

Figure 1.4: Appearance of trabeculations inside the ventricles; short axis slices of datasets used. Images (a), (b) courtesy of Wilcox et al. (2004).

| First author Series Last Name | Chin | Ichida | Oechslin | Sengupta | Murphy | Stöllberger | Kohli | Aras | Lofiego |
|---|---|---|---|---|---|---|---|---|---|
| Number of patients, number | 8 | 27 | 34 | 32 | 45 | 140 | 199 | 67 | 65 |
| Age at diagnosis, median | 7 | 5 | 40 | 49 | 37 (mean) | 53 (mean) | 64 (mean) | 45 | 53 |
| Male gender, % | 63 | 56 | 74 | 53 | 62 | 61 | 62 | 56 | x |
| Familial concurrence, % | 50 | 44 | 18 | | | | | | |
| Follow-up, maximum in years | 5 | 17 | 11 | | 15 | 13 | | 4 | 16 |
| EKG findings | | | | | | | | | |
| Bundle Branch | 25 | 15 | 56 | | 29 | 25 | 24 | | |
| Wolff-Parkinson-white | 13 | 15 | 0 | | x | 3 | x | | |
| Ventricular Tachicardia | 38 | 0 | 41 | | 20 | 18 | 7 | | |
| Clinical manifestations | | | | | | | | | |
| Heart Failure | 63 | 30 | 68 | 63 | 62 | 45 | 19 | 30 | 32 |
| Thromboembolic events | 38 | 0 | 21 | x | 4 | x | x | x | x |
| Associated neuromuscular disorders | x | x | x | x | x | 16 | x | x | x |
| Cardiovascular death | 38 | 7 | 35 | x | 2 | 6 | x | 6 | 3 |

Figure 1.5: Clinical characteristics of the largest NCC published series. Image courtesy Tizón-Marcos (2012).

lateral wall, thus increasing ejection fraction (LVEF) (Peters et al., 2002). On the other hand, the study done by Tizón-Marcos (2012) concluded that greater amounts of trabeculations are associated with lower global LVEF, lower segmental function, and increased Nt-ProBNP (N-terminal prohormone of brain natriuretic peptide, its release increases by cardiomyocyte stretch (Hall, 2005), and it is commonly used as a marker of greater wall stress). It is recognized that asymptomatic left ventricular dysfunction is a precursor of future symptomatic heart failure and is associated with increased mortality. Increased levels of Nt-ProBNP are reliable markers of poor cardiovascular prognosis including left ventricular dysfunction, congestive heart failure, acute coronary syndromes, and atrial fibrillation (Redfield et al., 2004; Kannel, 1987; Chen et al., 1999).

## 1.5 Contributions

The main goal of this thesis was to develop tools for 3D quantification and analysis of the detailed cardiac ventricular anatomy and apply these tools to study the development and the role of the trabeculations.

My research along the lines of this goal led to the following contributions:

- A simplified model of trabeculated LV to study the impact of the trabeculations on the stroke volume, strain and performance of LVs of different geometries (Chapter 2). Using a simplified model, I show that a trabeculated ventricle can work at lower strains compared to a nontrabeculated one to produce the same stroke volume. If extra stroke volume is needed, the trabeculations can help increasing it with less strain for a given ventricle. I also show that it is possible to find an optimal amount of trabeculations, where stroke volume (SV) is optimized while LV size remains within physiological ranges. The results of our experiments demonstrate, from a geometrical point of view, why trabeculations are necessary for a more efficient cardiac function, and that even a small amount of them can be beneficial. This knowledge can help in a better diagnosis of different patients, especially those with non-compaction cardiomyopathy, as well as understand why some dilated ventricles show hypertrabeculation while others do not.

- A simple as well as a more elaborate method for geometry independent parametrization of the detailed cardiac left and right ventricular anatomies to facilitate populational studies of cardiac anatomy and function (Chapters 3-4). Reparameterization of surfaces is a widely used tool in computer graphics that only recently started to gain popularity in the field of medical imaging. By consistently mapping the 3D myocardial information to a common 3D domain, surface reparameterization techniques allow to put anatomical shapes of inherently different geometry (but same topology) into correspondence. Using a quasi-conformal flattening of the myocardial

surfaces of the left and right cardiac ventricles, and extending it to cover the interior of the cavities using the local coordinates given by the solution of the Laplace's equation, I propose a method for anatomical parameterization of cardiac ventricular anatomies that includes myocardium, trabeculations, tendons and papillary muscles. Subsequently, I define a geometry independent representation for the detailed cardiac left and right ventricular anatomies that can be used for convenient visualization and statistical analysis of the trabeculations in a population.

- A framework for convenient three-dimensional visualization and statistical analysis of the trabeculations, longitudinally over time and transversally over individuals in a population (Chapter 5). The proposed framework consists of a standardized representation and novel, physiologically meaningful, complexity measures. The representation is based on the standardized subdivision of the myocardium into 3D blocks, using the previously introduced myocardial repararameterization, whereupon different measures of structural complexity can be calculated and summarized across a population. This framework allows to apply different complexity measures, normally applied to 2D image slices, in 3D and use 3D specific measures.

- A longitudinal analysis of the cardiac trabeculations in a mouse embyo at different gestational stages (Chapter 5). To the best of my knowledge this is the first study to quantify the regional progression of myocardial trabeculations. To carry out the analysis, we extend the standard fractal dimension (FD) to 3D and propose to describe the myocardial complexity by the volume, occupied by the trabeculations in each region, and their surface area. This measure provides an intuitive characterization of the complexity given that compact myocardium will tend to occupy large volume with very little surface area and high surface area is directly related to areas of the endocardium in contact with the blood. Using mouse embryo images at different gestational stages, we demonstrate how

the proposed representation and complexity measures describe the evolution of myocardial complexity and compare our results to the commonly used fractal dimension.

# Chapter 2

# RELATIONSHIP BETWEEN THE LEFT VENTRICULAR SIZE AND THE AMOUNT OF TRABECULATIONS

The content of this chapter is adapted from the following publication: **Paun B**, Bijnens B, Butakoff C, *Relationship Between the Left Ventricular Size and the Amount of Trabeculations*, under review, 2017.

## Abstract

Contemporary imaging modalities offer the possibility of non-invasive quantification of myocardial deformation, however they make gross assumptions about internal structure of the cardiac walls. Our aim is to study the possible impact of the trabeculations on the stroke volume, strain and capacity of differently sized ventricles using a geometrical model. The cardiac ventricle is represented by an ellipsoid and the trabeculations are represented by a tissue occupying a fixed volume. The ventricular contraction is modelled by scaling the ellipsoid whereupon the

measurements of longitudinal strain, volume and stroke volume are derived and compared. When the trabeculated and a similar non-trabeculated ventricles, having the same geometry and deformation pattern, contain the same amount of blood and contract with the same strain, we observed an increased stroke volume in our model of the trabeculated ventricle. When these ventricles contain and eject the same amount of blood, we observed a reduced strain in the trabeculated case. By analyzing the relationship between the amount of trabeculations and stroke volume we also identified the optimal thickness for the trabeculated layer of about $1\ cm$ (for end-diastolic volume of about $150\ ml$), assuming that about $50\ \%$ of the trabeculated layer are recesses filled with blood. A trabeculated ventricle can work at lower strains compared to a non-trabeculated ventricle to produce the same stroke volume, which could be a possible explanation why athletes and pregnant women develop reversible signs of left ventricular non-compaction, since the trabeculations could help generating extra cardiac output. This knowledge might help to assess heart-failure patients with dilated cardiomyopathies who often show signs of non-compaction.

## 2.1 Introduction

Recently, Bijnens et al. (2012) and Gabrielli et al. (2014) discussed the cardiac pump function in different cardiomyopathies from the engineering point of view, working out the relationship between the dimensions, output, and forces required to produce that output and how these factors could provoke cardiac remodelling. Although their model shed some light on the underlying mechanics of cardiac response to different conditions, the analysis assumes that the cavities are smooth, ignoring the effect that cardiac trabeculations may have, even though they are present in every heart.

One of the hypotheses of trabecular development suggests that the trabeculation formation is an initial step of myocardium compaction that allows accumulating large amount of tissue temporarily perfused by the surrounding blood. Subsequently the trabeculae undergo a process of

compaction, transforming the intertrabecular spaces into capillaries, and accompanied by the appearance of the coronary artery tree (Agmon et al., 1999; Bernanke and Velkey, 2002; Freedom et al., 2005). More recent studies on myocardial cell growth suggest, that after the trabeculations are formed, the cell proliferation concentrates only in the outer myocardial wall, forming the compact layer (de Boer et al., 2012). Once the heart has developed, the trabeculations do not disappear from the ventricles and the reason is not completely clear. The excess of trabeculations, often attributed to genetic cardiomyopathies, can lead to heart failure, atrial and ventricular arrhythmias, and thromboembolic events (stroke) (Ritter et al., 1997; Oechslin et al., 2000; Penela et al., 2013).

There is an important lack of clinical knowledge about the interior structure of the cardiac chambers. The increasing awareness of non-compaction cardiomyopathy (NCC) has awakened the need to know how the ventricular wall is organized and understand the role of the trabeculated myocardium, which can be seen in normal hearts. The trabeculations are more frequently seen at younger ages, with gender differences (Dawson et al., 2011) and were found to diminish with aging. The highest volume of trabeculated myocardium was found in the anterior and apical segments and was best visible during diastole. Another population with increased trabeculations are athletes (Gati et al., 2013), where a high proportion of young athletes exhibit conventional criteria for left ventricular non-compaction (LVNC), highlighting the non-specific nature of current diagnostic criteria if applied to elite athletic populations. LV hypertrabeculation was also more common in athletes of African/Afro-Caribbean origin.

In the last years, studies started to appear analyzing cardiac morphogenesis in zebrafish (Peshkovsky et al., 2011; Staudt et al., 2014), showing how the myocytes form protrusions and interconnect to become trabeculations. A very important role in the formation of trabeculations is played by the blood flow. The weak atrium mutant embryos (Peshkovsky et al., 2011) with non-contractile atrium exhibited substantially inhibited blood flow through the ventricle, in which case the initial protrusions did not progress toward creating myocardial ridges (trabeculations). Simi-

larly, disrupting flow into the left ventricle of embryonic chick hearts by left atrial ligation decreased left ventricular trabecular volume (Sedmera et al., 1999). Finally, mice that do not have primary cilia in their endothelial cells showed decreased cardiac trabeculation and abnormal outflow tract development, suggesting a role of shear stress sensing in chamber maturation (Captur et al., 2015; Samsa et al., 2013).

In this chapter, we focus on the relation between the trabeculations and the cardiac performance. Ashikaga et al. (2008) demonstrated that myocardial volume decreases in end systole (ES) more than accounted for by the vasculature inside the myocardium. The authors argued that the myocardial volume change during the cardiac cycle in the LV anterior wall of normal canine heart in vivo, using transmurally implanted markers and biplane cineradiography, is due to existence of additional mechanisms besides coronary blood volume movement that regulates myocardial volume. One of the anatomical structures that would potentially constitute the blood-filled spaces within the myocardium is the ventricular trabecular tissue. Peshkovsky et al. (2011) argue that trabeculae increase the amount of myocardial mass in the chamber and also create elaborate lacunae through which blood flows, which is also supported by Sedmera et al. (2000). Trabeculated myocardium has a markedly different viscoelastic behaviour, influencing the rate and magnitude of contraction and relaxation, than the compact myocardium (Miller and Wong, 2000). The abundance of observational papers point to the fact that the trabeculations could be serving as a mechanism for efficient filling and emptying of the chambers. Therefore we have developed a geometrical model of a trabeculated ventricle and analyzed its performance in the presence and absence of trabeculae.

## 2.2 Results

### 2.2.1 2D Visual Calculations

The ventricle ejects a certain amount of blood with each heartbeat by an overall contraction of the cavity. The stroke volume (SV) is affected by

both the amount of contraction and the size of the ventricle with the intricate relationships shown in Bijnens et al. (2012), which allows the ventricle to adapt to changing conditions. If more SV is required (e.g. with valve regurgitation or shunts), dilatation will provide a way to increase stroke volume with the same amount of deformation. In the case of decreased contractility (e.g. with ischemia or genetic alterations), dilatation provides a way to generate the same amount of stroke volume with less deformation (Fig. 2.1, first row).

There is one more mechanism, however, that allows the ventricle to adapt to the changing conditions – the trabeculations. Fig. 2.2a shows the initial configuration with trabeculations (dark blue represents compact myocardium, light blue – trabeculations) with interior area of 18 squares at end diastole (ED). The ES in Fig. 2.2a - b was obtained by fixing the strain: contraction by 1 square radially and 2 longitudinally. The resulting "SV" (change in cavity areas) is 16 squares for the trabeculated ventricle and 13 squares for the smooth ventricle. If SV is fixed instead of the strain, Fig. 2.2c shows the contraction that preserves the SV (18 squares), then the radial contraction increases to 1.5 squares and the longitudinal to 2.5 with respect to the trabeculated ventricle. This model shows how trabeculations can contribute to ejecting more blood out of the ventricle.

### 2.2.2 Relationship Between EDV, SV and Strain for Smooth and Trabeculated Ventricle

Fig. 2.1 - 2.4 illustrate the relationship between end-diastolic volume (EDV), SV and strain for smooth and trabeculated ventricle. The amount of trabeculations was chosen as to occupy $60\ ml$ ($8\ mm$ layer in ES) for the ventricle with end-systolic volume (ESV) of about $50\ ml$ (the blue interior in Fig. 2.3).

Two dots (red and blue) are shown on the plots to help compare them:

- The blue point corresponds to the condition when two cardiac chambers (trabeculated and non-trabeculated) contain the same amount of blood ($125\ ml$) and contract with the same strain ($10\ \%$). In

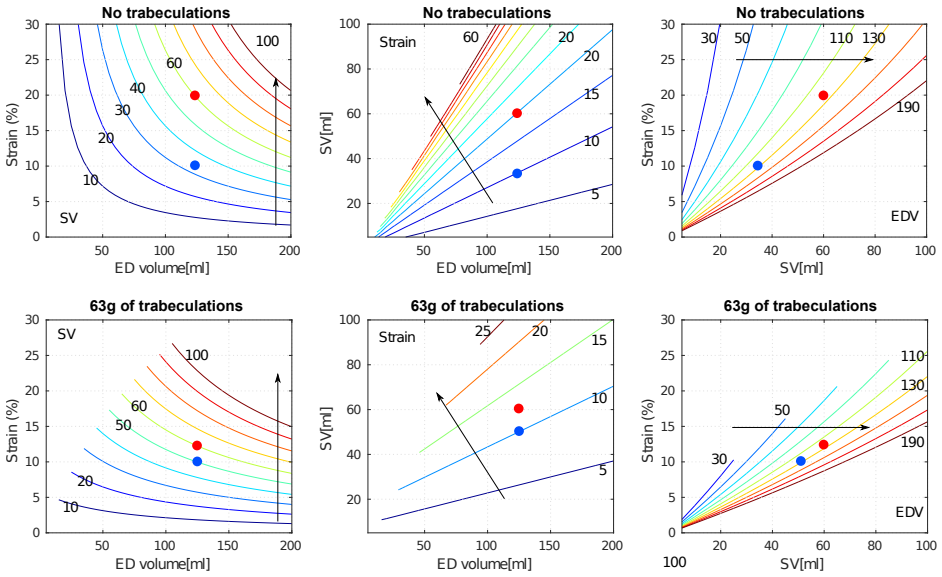


| Ventricle | Fixed EDV & Strain | | | Fixed EDV & SV | | |
|---|---|---|---|---|---|---|
| | EDV[ml] | Strain[%] | SV[ml] | EDV[ml] | Strain[%] | SV[ml] |
| Trabeculated | 125 | 10 | 50 | 125 | 12 | 60 |
| Nontrabeculated | 125 | 10 | 34 | 125 | 20 | 60 |

Figure 2.1: Results of simulating the ventricular contraction for the ventricle with and without trabeculations. The 2D plots show the isolines of the 3D plot (Fig. 2.4). One can see that the trabeculated ventricle can generate more SV than non-trabeculated one given constant EDV and strain (blue dot), and on the other hand the trabeculated ventricle needs less strain to generate the same SV as the non-trabeculated, given constant EDV (red dot). The arrows indicate the direction of the increase of the isoline values.

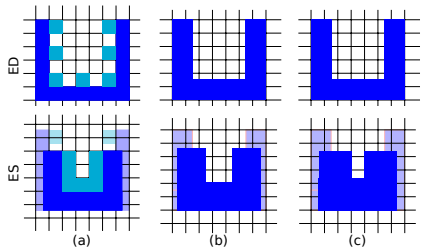


Figure 2.2: The impact of the trabeculations on the SV and strain for constant myocardial mass. The ventricle is represented by a rectangular 2D cavity overlaid over a grid to allow for visual calculations. Fig (a) shows the initial configuration with trabeculations (dark blue represents compact myocardium, light blue – trabeculations) the interior area is 18 squares at ED, at ES the compact endocardium is contracted by 1 square radially and 2 longitudinally, the resulting “SV” (change in areas) is 16 squares. Fig. (b,c) show the contraction of the cavity that only has compact myocardium. Fig. (b) shows the same contraction as (a) but without the trabeculations, as the result the SV is 13. Fig. (c) shows the contraction that preserves the SV (18 squares), however then the radial contraction is 1.5 squares and the longitudinal is 2.5. The grid in every sub-figure is positioned independently to simplify strain and area calculations, the apex is fixed and the base is moving towards the apex.

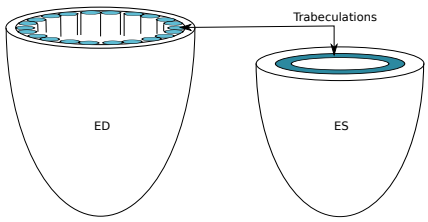


Figure 2.3: Schematic representation of the geometrical LV model used to study the relationship between EDV, SV and strain in trabeculated ventricle. Trabeculations are shown in blue.

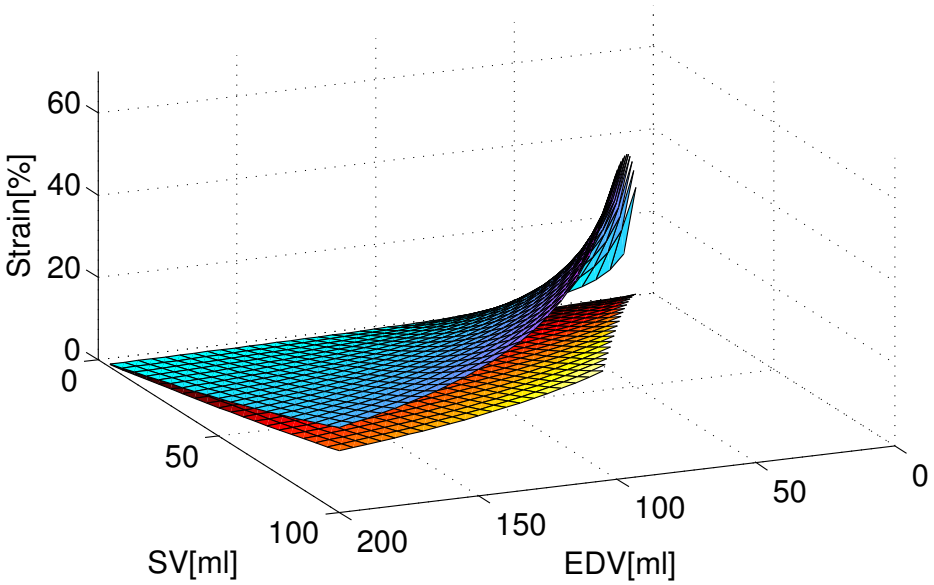


Figure 2.4: Results of simulating the ventricular contraction for the ventricle with (red surface) and without trabeculations (blue surface), showing the relationship between the EDV, SV and strain.

this case one can see the increased SV (about $47\ \%$ more) in the trabeculated ventricle.

- The red dot on the other hand represents two cardiac chambers (trabeculated and non-trabeculated) that contain ($100\ ml$) and eject ($20\ ml$) the same amount of blood. One can see that the trabeculated chamber requires less strain (about $40\ \%$ less) to perform the ejection.

The surfaces in Fig. 2.4 show a strong increase in strain required to generate high stroke volume in smooth-walled heart. In order to completely empty the cardiac chamber, in the absence of trabeculations, the required strain increases exponentially, while with trabeculations it is possible to completely empty the chamber using much lower strains.

We can conclude therefore that an increase in the amount of trabeculations can lead to reduced strains if SV and EDV are maintained constant. However, to accommodate the same EDV of blood with an increased amount of tissue within (trabeculations), the cavity has to dilate, effectively reducing the strain required to generate the same SV, but with a possibly higher wall stress. This dilatation leads to the observations similar to Bijnens et al. (2012):

- If an increased SV is required (e.g., during exercise), it can be generated by either adding more trabeculations or increasing strain (or both).
- If EDV increases (e.g., increased preload), the same SV can be generated with less strain by adding trabeculations to the ventricle.

### 2.2.3 Relationship Between SV and the Amount of Trabeculations

In this experiment, we wanted to see the tendency in SV reduction as the amount of trabeculations (expressed as a fraction of the volume within compact myocardium) increases. We have fixed the EDV and strain to normal values of $140\ ml$ and $20\ \%$, respectively. Fig. 2.5(a) shows that when the amount of trabeculations is not large (up to about $30\ \%$ of the cavity) the trabeculations do not change the overall chamber capacity a lot, still allowing it to contain approximately a constant volume of blood at ED. However, when the amount of trabeculations exceeds $30\ \%$, the capacity of the ventricle decreases rapidly. Fig. 2.5(a) shows that the theoretical limit for the amount of trabeculation is at about $50\ \%$, after which the ventricle with $60\ ml$ of trabeculations cannot contract any more with $20\ \%$ strain.

The relationship between the amount of trabeculations and the corresponding maximum strain (corresponding to $ESV = 0$) that a ventricle can achieve can be seen in Fig. 2.5(b). We can see a rapid drop in the maximum strain when the trabeculations occupy up to about $25\ \% - 30\ \%$ of the cavity and approximately linear drop with more trabeculations. The

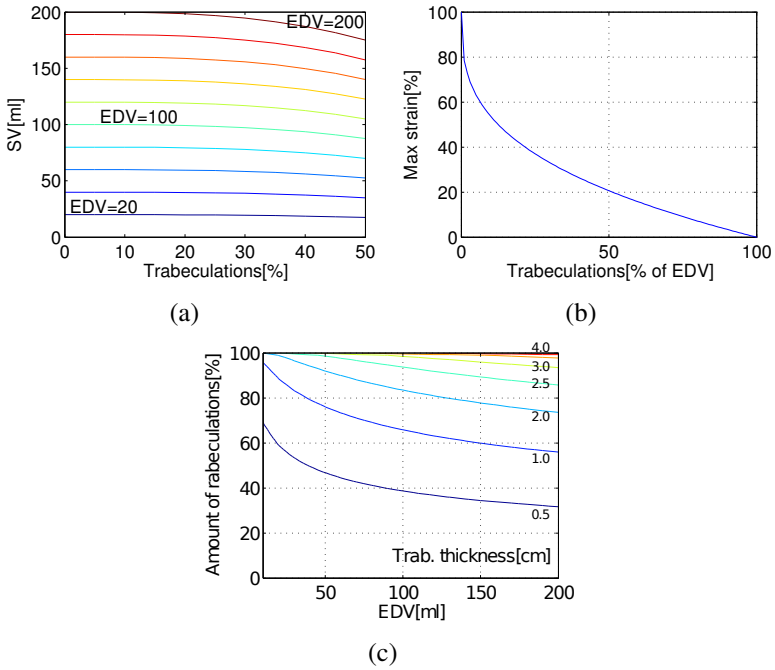


Figure 2.5: Relationship between the amount of trabeculations (as percentage of the EDV) and maximum stroke volume (a), amount of trabeculations and maximum strain (b), amount of trabeculations expressed in terms of thickness and EDV (c). EDV is the total volume of the space occupied by both blood and trabeculations. The thickness of the trabeculated layer is calculated assuming that the trabeculations do not have recesses (if one would add recesses as it is in reality, the thickness would be larger)

Fig. 2.5(c) shows an approximate thickness of the trabeculated layer for the different cavity volumes and the amount of trabeculations.

From the Fig. 2.5(b) we can see that the trabeculations have the highest impact when their amount is between $0$ and $25$ $\%$ of EDV. As seen from the Fig. 2.5(c) this would correspond to a trabeculated layer of about $0.5$ $cm$ (for EDV of about $150$ $ml$), or $1.0$ $cm$, if one could assume that about $50$ $\%$ of the trabeculation volume are recesses. The latter confirms the measurements of the typical thickness of the trabeculated layer of Dawson et al. (2011), where the thickness in ED was reported to vary from $0.3$ to $0.8$ $cm$.

The above plots suggest that mild trabeculations, as long as they are not interfering with the blood flow, can help reducing the ventricular strain, while providing the same amount of blood to the body. The excessive trabeculations however bring a risk of cardiac insufficiency by either hampering the development of the necessary strain or simply by reducing the space occupied by the blood, possibly leading to higher blood pressures. In both scenarios the ventricle may be forced to dilate, if possible.

## 2.3 Discussion

In this chapter we presented an analysis of the relation of ventricular size, trabeculations, deformation and the resulting stroke volume. We found that:

- trabeculations increase SV with less strain for a given ventricle and
- there is an optimal amount of trabeculations (with a value close to what is found in clinical measurements of the left ventricles), where SV is optimized while LV size is still within physiological ranges.

We believe that in the cardiac development there is a search for an optimum. Nature tries to reduce both stress (related to ventricular size) and strain (related to energy consumption) while adapting the stroke volume to the necessities of the body. The strain can be reduced by adding trabeculations. However, adding too many trabeculations requires dilation

to accommodate a certain volume of blood. The literature seems to point out that the trabeculations were most often observed in the subjects with increased preload, where the significant amount of trabeculations seem to be easily identified even in echocardiography. In particular, in chick embryos, experimental changes in loading conditions have been shown to lead to changes in ventricular myoarchitecture: increased pressure load resulted in an accelerated development of the compact layer with thicker, coarser trabeculae and diminished intertrabecular spaces. On the other hand, volume loading resulted in an increased number of thinner trabeculae (Sedmera et al., 1999). Patients with heart failure and chronic anaemia frequently demonstrate increased LV trabeculations, which may be compatible with the diagnosis of LV non-compaction. Due to reduced ability of the heart to contract, the heart could be trying to produce additional SV by adding trabeculations. A similar effect was noticed in pregnant women, where, due to increased requirement on cardiac output and increased preload (Melchiorre et al., 2012), the heart seems to generate more trabeculations to cope with the new requirements, which disappear in approximately 2 years post partum (Gati et al., 2014).

Intense and regular physical exercise is responsible for various cardiac changes, some associated to enlargement of the cardiac chambers and an increased amount of trabeculae, sometimes meeting the criteria for the LVNC (Dores et al., 2015). For instance, Gati et al. (2013) showed a higher prevalence of LV trabeculation in athletes compared to controls ($18.3\ \%$ vs. $7.0\ \%$), with $8.1\ \%$ fulfilling criteria for LVNC. In this particular population, the increased level of trabeculations would allow for increased rates of ventricular emptying and ventricular filling of the trained subjects (about $20\ \%$ and $71\ \%$ greater) (Gledhill et al., 1994).

The amount of trabeculations is also directly related to the cardiac output (CO), the latter being a product of heart rate (HR) and SV. The CO of trained endurance athletes may increase from $5 - 6\ L/min$ at rest to up to $40\ L/min$ during maximal exercise (Pluim et al., 2000) with the HR between $160$ and $220\ bpm$. In pregnancy, the CO increases by about $1L/min$ (Sanghavi and Rutherford, 2014) with HR increasing to about $85 - 90\ bpm$. Increase of CO can be achieved by either increas-

ing HR or SV. HR increase provides an acute increase of CO while SV increase is predominantly due to chronic cardiac remodeling. From the graphs presented in this chapter, it can be seen that to reach a certain CO in a non-trabeculated ventricle one would require either stronger contraction (higher strain), than in the trabeculated one, or higher HR (or both). Higher strain, given a fixed EDV would provide an additional SV, but in order to generate more strain, chronic beta-adrenergic stimulation or hypertrophy of the myocardium might be required. On the other hand, increasing trabeculation together with dilatation of the ventricle (to accommodate the same amount of blood) would lead to either: a) maintenance of normal strain and an increase in SV, or b) smaller strains to output the same SV.

While non-compaction cardiomyopathy (NCC) has been related to genetic mutations and similarities have been found with hypertrophic cardiomyopathy (HCM) (Arbustini et al., 2014), from our analysis, the hypertrabeculation in HCM might find their origin in an adaptive mechanism to optimize cardiac performance in the presence of altered tissue microstructure or cellular contractility. This would partially explain the wide variety of phenotypes of NCC seen in different genotypes.

## 2.4 Materials and Methods

### 2.4.1 2D Visual Calculations

The effect of the trabeculations on the ventricular performance can be shown using a simple theoretical model. We represent a ventricle by a 2D rectangle on a grid (Fig. 2.2), where we can easily measure enclosed area, strain, and easily model contraction. We consider 2 cases: smooth ventricle (the blue "U" shape) and a ventricle with trabeculations ("U" shape with squares on the interior). The top row shows the ventricle at ED and the bottom row – the same ventricle at ES, overlaid over the ED shape (shaded).

### 2.4.2 Ellipsoidal Model of the Left Ventricle

To quantify the relationship of the LV size and performance, the left ventricular endocardium was modelled as a half of an ellipsoid with two of the three radii equal and fixed ratio between the short and long radii. Trabeculations were modelled as a certain volume, that does not change during the cardiac cycle (non-contracting tissue), inside of the ventricle that is not occupied by the blood (see Fig. 2.3). The longitudinal strain is defined as the relative difference between the ellipse circumferences in ED and ES. The shapes in ED and ES are modelled by scaling. The detailed description of the model can be found in Section 2.6.

## 2.5 Conclusions

In this chapter we presented a theoretical analysis of how cardiac trabeculations relate to the stroke volume and strain for the chamber of different sizes. The main conclusion that we can draw is that the trabeculations can serve to aid the heart in increasing its stroke volume without increasing the strain. The analysis has been carried out on an ellipsoidal representation of a cardiac chamber. The proposed model does not assume any specific shape or localization of the trabeculations. For our analysis and derivations we considered the trabeculations as a piece of tissue that occupies some volume in the interior of the chamber. Nevertheless, in reality, the shape and the distribution of the trabeculations is likely very important as well, having considerable impact on haemodynamics of the blood. For instance, the left ventricle tends to have all the trabeculations accumulated towards the apex and mostly on the lateral walls, having most of the cavity clean so that the blood can efficiently circulate from the inlet to the outlet. In the right ventricle on the other hand, there are much more trabeculations in the middle of the cavity, and given that the RV walls exercise much lower radial strain than LV, the extra trabeculations help keeping the SV sufficiently high. Finally, for our experiments we have imposed a given ventricular deformation, independent on the whole dynamics of the contraction, so it is impossible to specify and control the

preload and afterload. In pathologies, the deformation might be larger or smaller and the rate of deformation is not taken into account in our simulations, but this will likely not influence the conclusions.

## 2.6 Appendix: Ellipsoidal Model of the Left Ventricle

### 2.6.1 Ellipsoidal Model of the Left Ventricle

In order to quantify the relationship of the LV size and performance, the left ventricular endocardium was modeled as a half of an ellipsoid. Wall thickness was not considered. Trabeculations were modeled as a certain volume, that does not change during the cardiac cycle (non-contracting tissue), inside of the ventricle that is not occupied by the blood (Fig. 2.3).

In order to find a unique relationship between the ventricle volume and the dimensions of the ventricle, the short axis radii of the ellipsoid were assumed equal and proportional to the long axis radius with the coefficient of proportionality $k = 1.3$, as in Bijnens et al. (2012) (based on a patient population).

The strain measure in this chapter, $\varepsilon$, is the longitudinal strain, defined as the relative difference between the ellipse circumferences in ED and ES (the ellipse is the intersection of the LV ellipsoid with a plane passing through the long axis).

In order to simulate the contraction, ESV for the nontrabeculated ventricle was calculated simply as a rescaled ellipsoid. When the trabeculations are present, we model them as an incompressible and shapeless tissue occupying some volume inside the ventricular cavity. In the plots, where the amount of trabeculations is fixed, the volume they occupy is $60\ ml$. This corresponds to about $8\ mm$ trabeculation layer in ES (in every region) for the ventricle with ESV of about $50\ ml$ (assuming ellipsoidal LV, the blue interior in Fig. 2.3).

**Relationship Between EDV, SV and Strain for Smooth and Trabeculated Ventricle**

For the analysis of the influence of the trabeculations, they are expressed as a fraction $t$ of the volume enclosed by the compact myocardium. We assume that the ventricle is maximally capable of ejecting all the blood out, meaning that at ES $ESV = 0$, this condition also corresponds to the maximum longitudinal strain of the ventricle.

All the plots were generated by the model for the ventricles with EDV taken in the interval $[5, 200]$, and SV – $[5, 100]$, both with a step of $5\ ml$.

### 2.6.2 Model Equations

**Relationship Between EDV, SV and Strain in a Trabeculated Ventricle**

In order to study the relationship of the LV size and performance, the left ventricular endocardium was modelled as half an ellipsoid. Wall thickness was not considered. Trabeculations were modelled as a fixed, not changing, volume (non-contracting tissue) inside of the ventricle that is not occupied by the blood.

In order to find a unique relationship between the ventricle volume and the dimensions of the ventricle, the short axis radii of the ellipsoid were assumed equal and proportional to the long axis radius with the coefficient of proportionality $k$:

$$R_l = kR_s \tag{2.1}$$

where $R_l$ and $R_s$ are the long and short radii respectively.

The strain $\varepsilon$ is defined as the relative difference between the circumferences in ED and ES:

$$\varepsilon = \frac{C_{ES} - C_{ED}}{C_{ED}} \tag{2.2}$$

The circumference $C$ is calculated according to:

$$C = \pi \left(R_l + R_s\right) \left(1 + \frac{3h}{10 + \sqrt{4 - 3h}}\right) \tag{2.3}$$

$$h = \left(\frac{R_l - R_s}{R_l + Rs}\right)^2 \tag{2.4}$$

which using (2.1) simplifies to:

$$C = \pi R_s \left(1 + k\right) \left(1 + \frac{3h}{10 + \sqrt{4 - 3h}}\right) \tag{2.5}$$

$$h = \left(\frac{k - 1}{k + 1}\right)^2 \tag{2.6}$$

The longitudinal strain can then be estimated from the change of the circumference between ED and ES as:

$$\varepsilon = \frac{C^{ES} - C^{ED}}{C^{ED}} = \frac{R_s^{ES}}{R_s^{ED}} - 1 \tag{2.7}$$

where $R_s^{ES}$ and $R_s^{ED}$ are the short-axis radii in ES and ED respectively.

The short radius can be calculated from the volume of the encapsulated blood $V$ according to:

$$R_s = \left(\frac{3V}{2k\pi}\right)^{\frac{1}{3}} \tag{2.8}$$

In order to model the trabeculations and do the plots we have taken EDV in the interval $[5, 200]$, SV – $[5, 100]$, both with a step of $5\ ml$. $k = 1.3$ was taken as in (Bijnens et al., 2012) (based on a patient population).

In order to simulate the contraction, ESV for the nontrabeculated ventricle was taken as:

$$ESV = EDV - SV \tag{2.9}$$

For the trabeculated ventricle the process was modified a little. In order for the cavity to contain the volume $V$ of blood and volume $V_t$ of trabeculations the cavities were estimated for the volume equal to:

$$EDV' = EDV + V_t \tag{2.10}$$
$$ESV' = EDV - SV + V_t \tag{2.11}$$

We used $V_t = 60\ ml$ in this study.

**Relationship Between SV and Amount of Trabeculations**

In order to analyse the relationship between the amount of trabeculations expressed as a percentage $t$ of the volume enclosed by the compact myocardium $EDV'$, given strain $\varepsilon$ and stroke volume $SV$. The following identities can be derived. Let $EDV$ be the end-diastolic volume (in the trabeculated ventricle). Then

$$EDV = EDV' - t \cdot EDV' \tag{2.12}$$
$$ESV = ESV' - t \cdot EDV' \tag{2.13}$$

or with the assumptions from Section 2.6.2

$$EDV = 2/3 \cdot \pi k(1-t) \left(R_s^{ed}\right)^3 \tag{2.14}$$
$$ESV = 2/3 \cdot \pi k \left((R_s^{es})^3 - t \left(R_s^{ed}\right)^3\right) \tag{2.15}$$

From (2.2) and (2.5) we can deduce that

$$R_s^{es} = R_s^{ed}(1+\varepsilon) \tag{2.16}$$

Then the maximum strain that would correspond to $ESV = 0$ can be related to the amount of trabeculations $t$ in the following way from (2.15) and (2.16):

$$2/3 \cdot \pi k \left((R_s^{es})^3 - t \left(R_s^{ed}\right)^3\right) = 0 \tag{2.17}$$
$$(1+\varepsilon)^3 \left(R_s^{ed}\right)^3 - t \left(R_s^{ed}\right)^3 = 0 \tag{2.18}$$
$$t = (1+\varepsilon)^3 \tag{2.19}$$

Valid values for the amount of trabeculations given a strain will be (so that $ESV \geq 0$): $t \in \left[0, (1+\varepsilon)^3\right]$ or

$$0 \leq t \leq \left(\frac{R_s^{es}}{R_s^{ed}}\right)^3 \tag{2.20}$$

And the maximum $SV$ that corresponds to $ESV = 0$ ($t$ - amount of trabeculations as a percentage of cavity volume:

$$SV = EDV = 2/3 \cdot \pi k(1-t^3)\left(R_s^{ed}\right)^3 \tag{2.21}$$

**Amount of Trabeculations and Maximum Strain**

Equation (2.20) allows establishing the relationship between the amount of trabeculations $t$ (or $100 \cdot t\%$) and the maximum strain that the ventricle could produce assuming that it ejects all the blood out. Reshuffling the terms gives us:

$$\varepsilon_{max} = t^{1/3} - 1 \tag{2.22}$$

Notice that when the amount of trabeculations is expressed in terms of percentage of the cavity that contains both blood and the trabeculations, the dimensions of the cavity disappear from the equation.

**Thickness of the Trabeculated Layer**

To calculate the thickness of the trabeculated layer we assume that the layer has no recesses and the tissue completely fills the space. It is not a realistic assumption but it gives a lower bound on the thickness. Adding recesses will increase the thickness. Given a ventricle with a certain EDV (volume that includes both blood and the trabeculations), and assuming the $100 \cdot t\%$ of trabeculations fill all the space along the endocardial wall, the thickness of the trabeculated layer can be calculated from (2.8) according to:

$$\begin{aligned} WT_{trab} &= R_s - R_s^{trab} \\ &= \left(\frac{3EDV}{2k\pi}\right)^{1/3} - \left(\frac{3EDV(1-t)}{2k\pi}\right)^{1/3} \end{aligned} \tag{2.23}$$

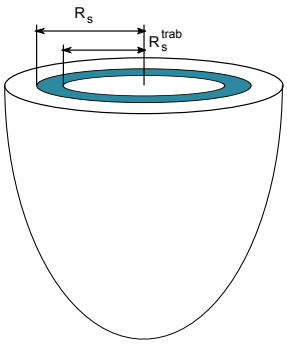


Figure 2.6: Definition of the symbols in equation (2.23).

where $R_s^{trab}$ is the short radius of the ellipsoid that represents the interface between the trabeculations and the blood and $R_s$ is the short radius of the ellipsoid that represents the interface between the trabeculations and the compact myocardium (see Fig. 2.6).

The calculated thickness represents the thickness in ED.

# Chapter 3

# SUBJECT INDEPENDENT REFERENCE FRAME FOR THE LEFT VENTRICULAR DETAILED CARDIAC ANATOMY

The content of this chapter is adapted from the following publication: **Paun B**, Bijnens B, Butakoff C, *Subject Independent Reference Frame for the Left Ventricular Detailed Cardiac Anatomy*, In Lecture Notes in Computer Science, 2015, Vol. 9126, pp. 240-247, Springer.

## Abstract

Mapping of surfaces to a parametric domain is a widely used tool in medical imaging for analysis and localization of injured tissue. By assigning the same coordinate values to specific anatomical landmarks, parametrization allows us putting into correspondence surfaces of anatomical shapes with inherently different geometry and facilitates integration of data ac-

quired by different imaging modalities. In this chapter we propose a method for subject independent anatomical parametrization of the left ventricular (LV) wall that includes trabeculations, papillary muscles and false tendons. The method relies on a disk parametrization of the LV smooth epicardium and mapping the interior of the ventricular cavity using ray casting. In this way we define a common reference frame whereupon any LV is mapped in a consistent way thus allowing for statistical analysis and comparisons between different patients.

## 3.1 Introduction

The role of trabeculations and their normal morphological expression in a heart is still unclear. The amount of trabeculae increases in both cardiac ventricles from base to apex everywhere except for the outflow tracts which are smooth (Wilcox et al., 2004). The interest in the trabeculations started to arise mostly due to the phenomenon of excessive trabeculations known as LVNC (Left Ventricular Non-Compaction), which is currently considered a heart disorder and can lead to heart failure, arrhythmias, including sudden cardiac death (Oechslin and Jenni, 2011). Nevertheless every heart has a trabeculated inner layer whose function is not completely clear. Additionally to the lack of understanding of the role of the trabeculations, there is also a lack of *in vivo* imaging data where the trabeculations are visible and could be either monitored through imaging or extracted to be included in cardiac model studies. Modeling those structures could provide an alternative way of analyzing their function and their relation to cardiomyopathies. Although advances in imaging techniques made extraction of detailed cardiac structures feasible, their accurate segmentation is still a challenging task. For instance, recently, M. Gao et al. proposed a method for a topologically accurate segmentation by restoring missing topological structures of a initially given segmentations (Gao et al., 2013) which allowed them to preform morphological analysis of such structures in LV (Gao et al., 2014).

Due to the above difficulties, when it comes to the computational mod-

els of the heart, most of them use a smooth endocardial surface for the cardiac chambers. An exception is the work of Bishop et al. (2010) where the authors attempted to investigate the effect of trabeculations in the rabbit heart. The analysis is carried out on the data extracted *ex vivo* as the only way of obtaining the highly detailed dataset. However if one wants to include detailed cardiac anatomy in the modeling studies of human hearts, most of the time one is limited to the *in vivo* data acquired using a 1.5T/3T MRI scanner for a reasonably short period of time. In the latter case, the resolution of the images is not sufficient to visualize the trabeculations and a different approach is necessary.

One of the possibilities to overcome this limitation is the extraction of the trabeculations from the *ex vivo* studies and using them in the computational models. This approach however requires establishing a mapping between the domains represented by the meshes. There is a wide spectrum of mesh parametrization methods applicable to different shape topologies: Least Squares Conformal Maps (Lévy et al., 2002), Discrete Surface Ricci Flow (Jin et al., 2008), Intrinsic Parameterizations (Desbrun et al., 2002) and Teichmüller Maps (Ng et al., 2013) to name a few. Surface parametrization is an active research field with applications to a wide range of problems. In the medical field, they have been applied to the problems of analysis and visualization of brain surfaces (Gu et al., 2004; Joshi et al., 2007; Wang et al., 2012), creation of inter-patient liver coordinate systems (Vera et al., 2014), visualization and mapping of functional information from ventricular cavities onto a discretized or continuous bull's-eye plot (Karim et al., 2014), creation of normalized parametric domain for comparison of LV function across subjects (Garcia-Barnes et al., 2010).

In this chapter we propose a method for mapping of detailed cardiac anatomy extracted from human hearts acquired *ex vivo* to any smooth surface either representing different cardiac geometry or a patient independent geometry. The proposed approach produces a *reference frame* where the detailed cardiac anatomy of different subjects can be represented in a manner independent of the overall shape of the heart. We show how this representation can be used for statistical analysis of the distribution and

differences in trabeculations.

## 3.2 Methods

The proposed method operates on two triangle surface meshes: $M$ and $S$ where $M$ represents the LV endocardial structures (trabeculations) and $S$ represents its bounding surface (tight surface on which the trabeculations reside). The preprocessing steps to obtain these meshes are explained in Subsection 3.2.4. Depending on the application, mesh $M$ can represent just endocardial structures of interest or all structures within the ventricular cavity, and can include a part or the whole myocardial wall which implies that a different base mesh $S$ has to be used. The whole process can be represented by 3 steps:

1. Mapping $S$ to the planar domain with the LV apex at the center.
2. Due to symmetry of the LV, orientation ambiguity is eliminated.
3. Mapping $M$ into the cylinder defined by the flattened $S$.

Prior to applying a mapping function $\rho$ to different subject meshes $M$, we are locating two anatomical landmark points on their corresponding base meshes $S$. As cardiac landmarks we use the apex and the mid-septal point of the *mitral annulus* $\delta S$. The mid-septal point of $\delta S$ is manually defined by the user, while the apex is defined as the furthest point from the centroid $c_{\delta S}$ of $\delta S$.

### 3.2.1 Mapping of the Anatomical Base Mesh to a Planar Domain

As the planar domain for $S$ we used a unit disk following the approach of De Craene et al. (2012). As implied by the Riemann Mapping Theorem, any surface homeomorphic to a disk can be conformally mapped into any simply-connected region of the plane. The only requirement is that our

mapping is harmonic, meaning that every surface coordinate has to have a vanishing Laplacian. Therefore we are computing a bijective mapping $\varphi : S \subset \mathbb{R}^3 \longrightarrow D \subset \mathbb{R}^2$, where $S$ is the anatomical base surface mesh of the LV and $D$ is a unit disk. The boundary $\partial D$ of $D$ is defined by uniformly sampling a unit circle with the number of samples equal to the number of points on the boundary $\partial S$ and the following system of linear equations is solved for the coordinates of the points inside the disk:

$$\begin{cases} L_{S\setminus\partial S} \cdot \mathbf{x}_{D\setminus\partial D} = 0 \\ \mathbf{x}_{\partial D} = \mathbf{x} \end{cases} \tag{3.1}$$

The boundary $x$, $y$ coordinates are given by the columns of matrix $\mathbf{x}$. $L_{S\setminus\partial S}$ represents the Laplacian matrix of the mesh $S$ with the rows corresponding to its boundary $\partial S$ removed. $\mathbf{x}_{\partial D}$ and $\mathbf{x}_{D\setminus\partial D}$ are the matrices of coordinates of the points on the disk (the one we are calculating and that define our mapping) corresponding to the boundary and the interior, respectively. The desired mapping is then given by (3.1), while the connectivity information is retained from the mesh $S$. An example of the mapping can be seen in Fig. 3.1.

As a result of this mapping, the position of the apex in the planar domain will still be variable and depend on the specific anatomy. However in order to define a subject independent frame we must make sure that the apex is consistently mapped to the same point which is achieved using thin plate splines, mapping the boundary to itself and the apex to the center of the disk. This additional step will enforce a more consistent localization of the cardiac regions among different subjects, but reduce the conformal map to quasi-conformal.

### 3.2.2 Elimination of Orientation Ambiguity

To assure correspondence of parametrized meshes $N$ and $D$ between subjects we are removing orientation ambiguity by assigning the same coordinate values to their mid-septal landmarks. Thus during the mapping to a unit disk we are placing these landmarks at the same location $\mathbf{x}_l = (1, 0)$ ($l$ is the index of the landmark in the array of all the points).

### 3.2.3 Mapping the Detailed LV Anatomy

Once we have the outer surface $S$ of the LV mapped to the disk $D$, we have provided a base of a subject independent reference frame on top of which we want to map a detailed mesh $M$. To do so, we first project the vertices of $M$ onto $S$. The common way of achieving this would be to locate the closest point $v_S^{'}$ for every vertex $v_M$. As the LV has structures traversing thorough the whole cavity, the closest point projection will not project the neighbourhoods of $v_M$'s to the neighbourhoods of $v_S^{'}$'s. Such projection will cause the mapping function $\rho$ to be non-bijective and result in a highly distorted mesh $N$.

To alleviate the above problem, we project the points by casting rays through all vertices $v_M$ from a fixed point $c_{\delta S}$ and locate the corresponding intersection points $v_S^{'}$. As the fixed point $c_{\delta S}$, we take a centroid of the surface boundary $\delta S$. The choice of the centroid of the *mitral annulus* as the origin of the rays is motivated by the fact that its location is free of any detailed structures we want to parametrize.

Subsequently, $v_S^{'}$ points are mapped to $v_D^{'}$ points using the map calculated in Subsection 3.2.1. Finally, for every $v_M$, we calculate its distance $d_{v_M v_S^{'}}$ along the ray to the corresponding $v_S^{'}$ normalized by the length $d_{c_{\delta S} v_s^{'}}$ of the ray segment between $v_S^{'}$ and $c_{\delta S}$. Then the vertices $v_M$ are mapped to our reference frame by placing them along the normal direction of $v_D^{'}$ at the distance $d_{v_N v_D^{'}} = d_{v_M v_S^{'}} / d_{c_{\delta S} v_s^{'}}$. The transformed vertices $v_N$ of $N$ have the same connectivity as $v_M$ of $M$.

### 3.2.4 Datasets and Preprocessing

The input meshes were obtained from 3T MRI datasets (Siemens Tim Trio, Erlangen, Germany) with $0.44 \times 0.44\ mm$ in-plane resolution and slice thickness of $1 - 1.17\ mm$. The Dicom datasets (as in Fig. 3.2(a), 3.2(b), 3.2(c)) were provided by the Visible Heart® Laboratory Laboratory (2015).

The meshes of the detailed LV anatomy including the part of the myocardial wall, are shown in Fig. 3.2(d), 3.2(e), 3.2(f). The meshes were

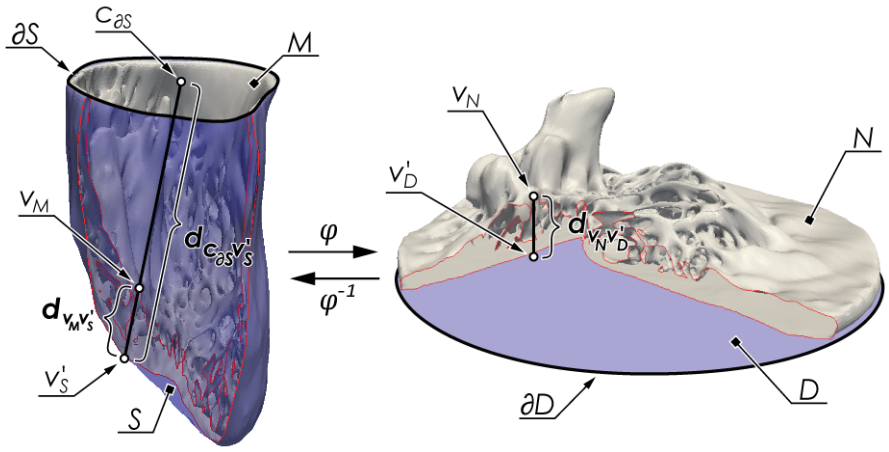


Figure 3.1: Illustration of the mapping of a trabeculated mesh vertex $v_M$ to the reference frame.

generated from the segmentations of the MRI data (Seg3D CIBC (2015)). The segmentations were cut at the basal part of the heart at the level of the valves, meshed using marching cubes of ParaView (Squillacote, 2008) and smoothed and uniformly remeshed using ReMesh (Attene and Falcidieno, 2006).

Base surface meshes $S$ were extracted from the above meshes of detailed anatomy using VTK (Schroeder et al., 2006) introducing a cut in the basal part along the boundary rim, separating the mesh into inner and outer open surfaces.

## 3.3 Results

The method proposed in the previous section was applied to six human LV datasets. Parametrized meshes $N$ of 3.2(d), 3.2(e), 3.2(f) are shown in Fig. 3.2(g), 3.2(h), 3.2(i). For every subject, max, mean and standard deviation of a height of $N$ (namely distance $d_{v_N v'_D}$ of their corresponding

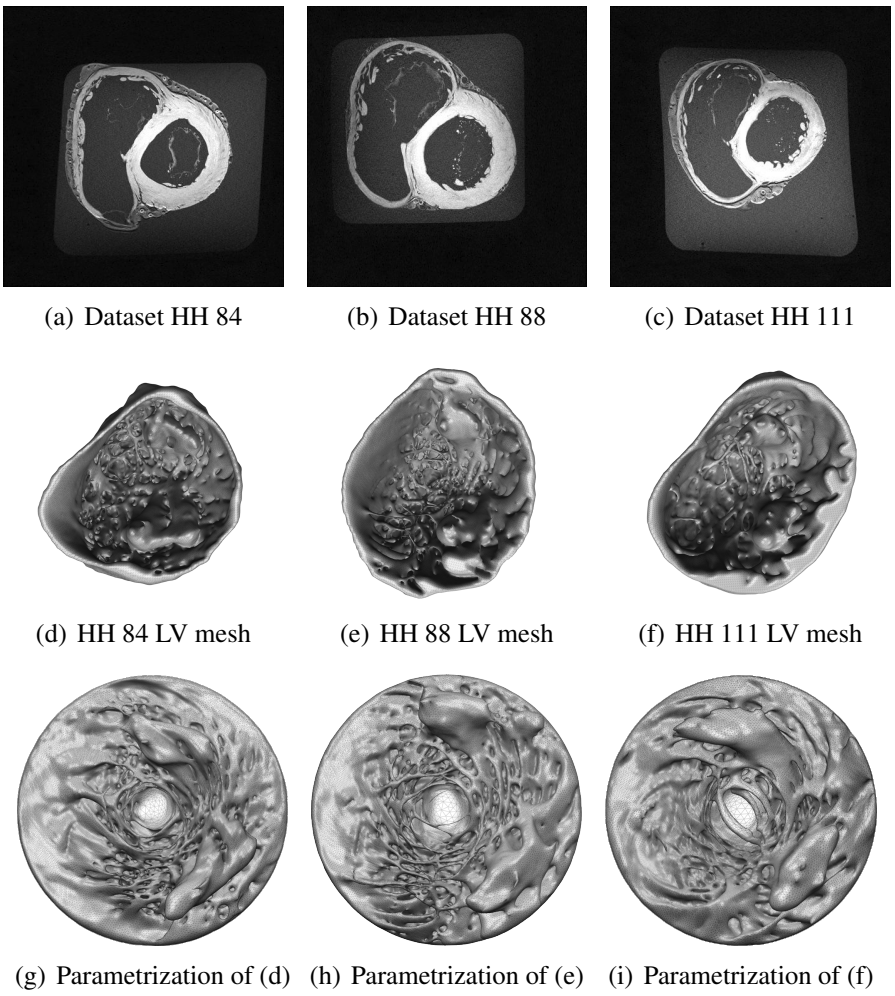

(a) Dataset HH 84 (b) Dataset HH 88 (c) Dataset HH 111

(d) HH 84 LV mesh (e) HH 88 LV mesh (f) HH 111 LV mesh

(g) Parametrization of (d) (h) Parametrization of (e) (i) Parametrization of (f)

Figure 3.2: (a), (b), (c) - middle stack short axis view slices of MRI human heart datasets; (d), (e), (f) - corresponding LV meshes; (g), (h), (i) - corresponding parametrized LV meshes.

vertices $v_N$) was calculated for the defined segments and averaged over all subjects. The corresponding plots are shown in Fig. 3.3. Calculations were obtained from non-normalized distances ($d_{v_N v'_D} = d_{v_M v'_S}$). The vertices $v_N$ residing on the outer surface of $N$ were excluded. The segments were arbitrarily defined to best show variability of measurements in plots. As the meshes $N$ include part of myocardial wall, we corrected the results by subtracting the value of the segment with min value which represent the cardiac wall.

From Fig. 3.2(g), 3.2(h), 3.2(i) one can observe unique trabecular morphology inherent to each subject. From the plots in Fig. 3.3 we observe an increase in the amount of trabeculations as we move from the base towards the apex of the LV. The basal part of the septal wall is free of trabeculations and they start to emerge in its middle part while, on the lateral wall, we have them present along the whole wall. The trabeculations present in the basal part of the lateral wall are attached to the wall along their whole length and they form big prominent ridges. The segments with maximal values correspond to locations where papillary muscles reside. Having this in mind, one can observe from the standard deviation plot that coarseness of trabeculations or sponginess of the heart increases toward the apex. That coincides with observations of a highly trabeculated apical region where trabeculations form a complex interwoven network.

## 3.4 Discussion

We proposed an bijective mapping of the detailed LV anatomy to a common reference frame represented by a cylinder with unit disk base. Every point inside the LV cardiac chamber is characterized by 3 coordinates: two coordinates characterizing the point's projection onto the anatomical bounding surface of the chamber and the normalized distance to that surface along a ray. The surface is then flattened by a quasi-conformal transformation to a disk whereupon any point is characterized by two coordinates. The choice of the disk as a parametric domain was motivated

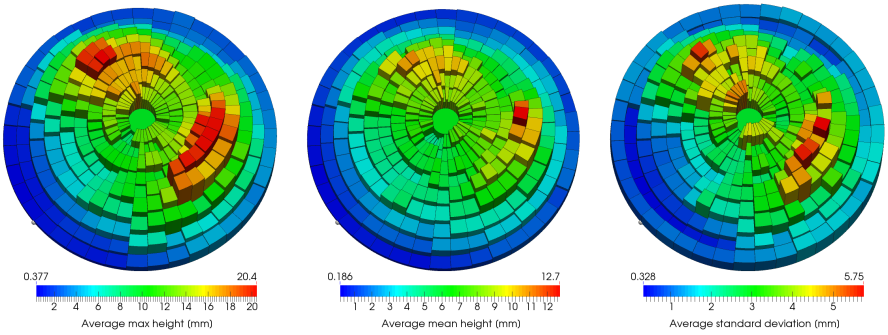


Figure 3.3: Max, mean and standard deviation of parametrized meshes heights per segment averaged over all the cases.

by the fact that such domain is well suited, and is traditional, for visualizations or mapping of any information from LV cavities onto a discretized or continuous bulls-eye plot Cerqueira et al. (2002).

## 3.5 Conclusion

The proposed method represents a major step forward in the analysis and quantification of different detailed cardiac morphologies among patients in a common framework with the potential application in computational cardiac models and construction of the atlas of trabeculations.

# Chapter 4

# PATIENT INDEPENDENT REPRESENTATION OF THE DETAILED CARDIAC VENTRICULAR ANATOMY

The content of this chapter is adapted from the following publication: **Paun B**, Bijnens B, Iles T, Iaizzo PA, Butakoff C, *Patient Independent Representation of the Detailed Cardiac Ventricular Anatomy*, Medical Image Analysis, 2017, 35:270-87.

## Abstract

Reparameterization of surfaces is a widely used tool in computer graphics known mostly from the remeshing algorithms. Recently, the surface reparameterization techniques started to gain popularity in the field of medical imaging, but mostly for convenient 2D visualization of the information initially represented on 3D surfaces (e.g. continuous bulls-eye plot). However, by consistently mapping the 3D information to the same 2D domain, surface reparameterization techniques allow us to put into cor-

respondence anatomical shapes of inherently different geometry. In this chapter, we propose a method for anatomical parameterization of cardiac ventricular anatomies that include myocardium, trabeculations, tendons and papillary muscles. The proposed method utilizes a quasi-conformal flattening of the myocardial surfaces of the left and right cardiac ventricles and extending it to cover the interior of the cavities using the local coordinates given by the solution of the Laplace's equation. Subsequently, we define a geometry independent representation for the detailed cardiac left and right ventricular anatomies that can be used for convenient visualization and statistical analysis of the trabeculations in a population. Lastly we show how it can be used for mapping the detailed cardiac anatomy between different hearts, which is of considerable interest for detailed cardiac computational models or shape atlases.

## 4.1 Introduction

Surface parameterization is a bijective mapping from a suitable parameter domain to the surface. As the parameter domain itself is usually a surface, the parameterization represents a mapping from one surface onto another, providing that the surfaces have the same topology (Sheffer et al., 2006; Floater and Hormann, 2005). In computational geometry the surfaces are approximated by 3D triangulated meshes and their parameterization is a process of creating piecewise linear mappings between the mesh and simpler triangulated domains such as planar regions, simplicial complexes or spheres (Sheffer et al., 2006). Surface parameterization is most frequently used in the field of computer generated imagery (CGI) as a method for mapping textures onto surfaces to add realism to the simplified polygonal meshes. There are also many applications in numerous problems such as texture synthesis, detail transfer, mesh completion, mesh editing, remeshing, mesh compression, object morphing and others.

Planar parameterization of general surfaces always introduces distortion in either angles or areas as stated by *theorema egregium*, and isometric (distance preserving or zero distortion) mappings are possible only for

developable surfaces with zero Gaussian curvature. Thus, parameterization of arbitrary surfaces used in practice are mappings which minimize these distortions, such as conformal (angle preserving), equiareal or authalic (area preserving) and mappings which minimize some combinations of angle and area distortion. Planar mapping methods can be additionally divided into free and fixed boundary mappings. Fixed boundary mappings transform the boundary of a mesh to a predefined boundary in the 2D domain while boundary free methods compute the boundary of 2D domain as part of the solution that reduces the distortion.

Many of the planar parameterization methods are built upon Tutte's formulation of graph embedding, which directly applies to the meshes (Tutte, 1963). These parameterizations normally are performed in two stages. First, the boundary vertices of the 3D surface mesh are mapped to the boundary of the predefined 2D region. Afterwards, the positions of the remaining vertices are obtained by solving a system of linear equations (Pinkall and Polthier, 1993). Every mesh, which satisfies the Delaunay criterion, will have a bijective flattening map as suggested by Kharevych et al. (2006).

In medical imaging, harmonic mappings were first applied in neurology for the analysis and visualization of brain surface, where the complex brain structure was mapped to a sphere or a planar domain (Hurdal et al., 2000; Haker et al., 2000; Gu et al., 2004; Joshi et al., 2007; Wang et al., 2012). In cardiology, reparameterization is mostly used to visualize any functional information of the ventricular cavities on a discretized or continuous bull's-eye plot (Cerqueira et al., 2002). Such information can be coming from imaging modalities or electro-physiological measurements (Soto-Iglesias et al., 2013). A similar approach has recently been applied to the description of atria using a standardized unfold map or rectangular unfold map for the analysis of atrial fibrillation patients (Tobon-Gomez et al., 2015; Karim et al., 2014). Recently, harmonic spherical mapping was applied in hepatology for definition of an inter-patient liver coordinate system (Vera et al., 2014). Surface parameterization was also employed for creation of a normalized parametric domain for comparison of left ventricular function across subjects (Garcia-Barnes et al., 2010).

Young et al. (2006) developed a finite element parameterization method for regional analysis of 3D myocardial function and construction of a 3D model of infarct geometry combined with 3D strain information, which was also used by Zhang et al. (2014) for mapping of left ventricular regional remodeling due to myocardial infarction. Another example of normalized domain is a tissue sampling map proposed by Young et al. (2011) used for coregistration of CMRI and ex-vivo tissue sampling.

When talking about detailed cardiac anatomy, it is necessary to mention that, although the current imaging techniques made screening of those structures feasible ex vivo, their accurate segmentation still represents a challenging task. M. Gao et al. recently proposed a method for a topologically accurate segmentation by restoring missing topological structures of initially given segmentations (Gao et al., 2013), which allowed them to preform morphological analysis of such structures in the left ventricle (LV) (Gao et al., 2014).

In this chapter, we propose a method for a patient independent anatomical parameterization of the interior of cardiac ventricles for the representation of the detailed ventricular anatomy (myocardium, trabeculations, papillary muscles, etc.). The proposed method represents a generalization of the parameterization procedure proposed by Paun et al. (2015) used for parameterization of the detailed cardiac anatomy of left ventricles, which in general have a ellipsoidal-like shape. Unfortunately, that method introduces unwanted distortion and folding when applied to the more complex shapes such as the right ventricle (RV). To overcome such limitations we propose a general method that can be applied to objects of an arbitrary shape.

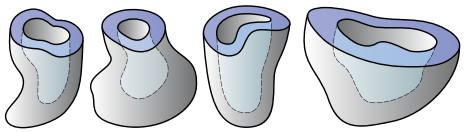

Figure 4.1: Examples of different shapes of thick shell structures.

## 4.2 Methods

### 4.2.1 Overview of the Geometry Independent Representation

In this section we will introduce a general framework for representing any object $M$ with an overall shape of a thick hemispherical shell (in the following text we will call them shell-like objects for simplicity) based on the fact that it is homeomorphic to a cylinder. A number of examples of such objects can be seen in Fig. 4.1. In order to establish the homeomorphism, apart from the object $M$ itself, represented by either a surface or volumetric mesh, we will also require an enclosing surface $S$, usually represented by a triangulated mesh, that contains the whole $M$ in its interior.

The whole procedure of calculating the mapping can be described by the following steps (explained in the following sections and illustrated in Fig. 4.2):

1. Mapping of $S$ to a suitable planar domain $D$.
   (a) Specifications of landmarks on $S$ to impose a consistent orientation.
   (b) Conformal or quasi-conformal flattening.
2. Mapping of $M$ to the volumetric domain defined by the base $D$ (usually a cylinder or a prism).

For convenience, the most common symbols used in this chapter are listed in Table 4.1.

### 4.2.2 Specification of the Landmark Points on the Enclosing Surface

In order to define a common representation for the shell-like objects and achieve a unique correspondence between different instances of such objects, we propose to fix three landmark points on $S$ (see Fig. 4.2). These

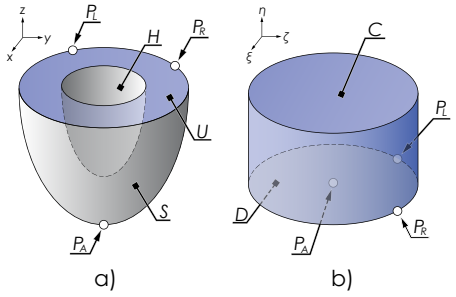


Figure 4.2: Illustration of domain of interest with corresponding surfaces and landmark points. a) Domain $U$ defined by enclosing surface $S$, interior surface $H$, and landmark points $P_A$, $P_L$ and $P_R$. b) Cylinder domain $C$ of unit height defined by planar domain $D$ and corresponding landmarks. Symbols: $P_L$ - left boundary landmark; $P_R$ - right boundary landmark; $P_A$ - apical landmark; $S$ - enclosing surface; $H$ - interior surface; $U$ - domain between $S$ and $H$; $D$ - planar domain; $C$ - cylinder.

| **Table of symbols** | |
|---|---|
| $S$ | enclosing surface |
| $H$ | interior surface |
| $U$ | domain between $S$ and $H$ |
| $\partial S$ | boundary of $S$ (curve) |
| $M$ | shell-like object |
| $D$ | surface $S$ mapped to the planar domain |
| $\partial D$ | boundary of $D$ (curve) |
| $N$ | object $M$ mapped to the cylinder |
| $P_i$ | a landmark (specified by the subscript) |

Table 4.1: List of symbols used in this chapter

points will be mapped to predefined locations in the planar domain, thus removing orientation ambiguity due to rotational and mirror symmetry. Two points, $P_L$, $P_R$, related to some easily identifiable features of the object, should be located on the boundary $\partial S$. The third point, $P_A$, should represent the position of the pole (apex) of the surface $S$.

### 4.2.3 Mapping of the Enclosing Surface to the Planar Domain

The identification of the landmarks on $S$ is followed by the mapping step of the surface $S$ to the planar domain. The planar domain represents the base of the corresponding normalized reference frame and can be represented by any convex planar shape. As implied by Riemann Mapping Theorem (Riemann and Wilkins, 1851), any surface homeomorphic to a disk can be conformally mapped into any simply-connected region of the plane. The method we use here is the same as the one used in the paper of De Craene et al. (2012).

A bijective mapping $\varphi : S \subset \mathbb{R}^3 \longrightarrow D \subset \mathbb{R}^2$, where $S$ is the enclosing surface and $D$ is the corresponding planar domain, can be computed by solving the following system of linear equations:

$$\begin{cases} L_{S\setminus\partial S} \cdot X_{D\setminus\partial D} = 0 \\ X_{\partial D} = X \end{cases} \tag{4.1}$$

$$X = \begin{pmatrix} \cos(t_0) & \sin(t_0) \\ \cos(t_1) & \sin(t_1) \\ \vdots & \vdots \\ \cos(t_B) & \sin(t_B) \end{pmatrix} \tag{4.2}$$

where $t_i \in [0, 2\pi]$ and $B$ is the number of vertices on $\partial S$.

The desired (fixed) boundary coordinates $\xi$, $\zeta$ are given by the columns of matrix $X$. $L_{S\setminus\partial S}$ represents the Laplacian matrix of the surface $S$ with the rows corresponding to its boundary $\partial S$ removed. $X_{\partial D}$ and $X_{D\setminus\partial D}$ are the $\xi$, $\zeta$ coordinates of the points on the planar domain corresponding to the boundary and the interior, respectively.

The above methodology provides a simple method for mapping $S$ to the planar domain $D$ where its corresponding boundary edge $\partial S$ is mapped to the perimeter of $D$. To impose a unique correspondence between different enclosing surfaces their landmarks $P_L$, $P_R$ and $P_A$ are mapped to the same predefined locations on the planar domain.

### 4.2.4 Mapping of the Shell-like Objects to a Cylinder

Let $\psi : M \to C$ be the bijective mapping of the object $M \subset \mathbb{R}^3$ onto a cylinder $C \subset \mathbb{R}^3$. Let $\psi(v_M) = v_C \in C$ for any $v_M \in M$. In this section we will provide the procedure to calculate the $\psi$ using the ideas of Yezzi and Prince (2003).

Let $S$ be the enclosing surface of the object $M$, $H$ the interior surface of $M$, $U = M \setminus (S \cup H)$ the domain between the $S$ and $H$ (see Fig. 4.2). Let $f(x, y, z)$ be a scalar field, the solution to the Laplace's equation in $U$:

$$\Delta f(x, y, z) = 0 \tag{4.3}$$

with the following boundary conditions

$$f(x, y, z) = -1, \forall (x, y, z) \in S \tag{4.4}$$
$$f(x, y, z) = 1, \forall (x, y, z) \in H \tag{4.5}$$

Then for every point $v_U \in U$ we can find a unique integral curve $c(t) = (c_x(t), c_y(t), c_z(t))$ of the vector field $\nabla f$ such that $v_U \in c(t)$. The curve $c(t)$ can be calculated by solving the following system of equations:

$$\frac{dc(t)}{dt} = \nabla f(c(t)) \tag{4.6}$$

with the condition

$$c(t_v) = v_U \tag{4.7}$$

By solving (4.6) in both directions, apart from the solution $c(t)$, we also will obtain the points $v_H$ and $v_S$ where $c(t)$ intersects $H$ and $S$ respectively and the corresponding values for the parameter $t$:

$$c(0) = v_S, v_S \in S \tag{4.8}$$

$$c(t_{max}) = v_H, v_H \in H \tag{4.9}$$

Thus we propose to represent any point $v_U \in U$ by the point $v_S \in S$ and the normalized distance $d(v_U)$ along the corresponding integral curve $c(t)$:

$$d(v_U) = \int_0^{t_v} \left\| \frac{dc(t)}{dt} \right\| dt \Big/ \int_0^{t_{max}} \left\| \frac{dc(t)}{dt} \right\| dt \tag{4.10}$$

Having calculated the parameterization of $S$ and the normalized distance $d(v_U)$, and assuming $\varphi(v_S) = (\xi, \zeta)$, then every point $v_U \in U$ can represented inside the cylinder $v_C = (\xi, \zeta, d(v_U)) \in C$. If necessary, the same point can also be represented using cylindrical coordinates.

## 4.3 Geometry Independent Representation of the Cardiac Ventricles

The motivation for development of the proposed method was the parameterization of the cardiac ventricles for the representation of the detailed ventricular anatomy of the heart (Fig. 4.3).

The following subsections will explain how the proposed mapping framework can be applied to two meshes, $M_{LV}$ and $M_{RV}$ (in this chapter – triangulated surface meshes), that represent detailed endocardial structures of the LVs and RVs, respectively. The outer bounding surfaces $S_{LV}$ and $S_{RV}$ are the corresponding anatomical bounding surface meshes extracted from $M_{LV}$ and $M_{RV}$. We define the anatomical bounding surface as the concave hull of the cardiac structures that we want to map onto the geometry independent representation. The process of obtaining meshes $M_{LV}$, $M_{RV}$, $S_{LV}$ and $S_{RV}$ is described in subsections 4.4.2 and 4.4.2.

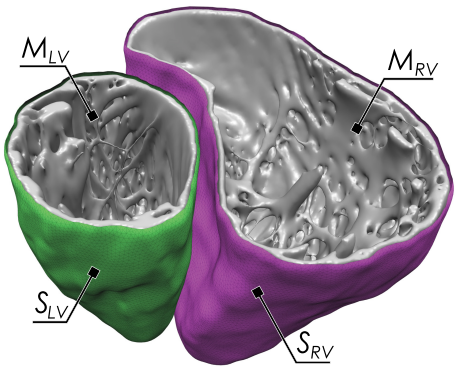


Figure 4.3: Visualization of detailed anatomical meshes and their extracted anatomical bounding surface meshes. The bounding surfaces are concave hulls of the trabeculated layer.

Depending on the application, detailed anatomy meshes $M_{LV}$ and $M_{RV}$ can represent just endocardial structures of interest or all the structures within the ventricular cavity, and can include a part or the whole myocardial wall,therefore different anatomical boundary meshes $S_{LV}$ and $S_{RV}$ can be used, representing different meaningful anatomical bounding surfaces such as endocardium or epicardium.

For the interior surface $H$ we use a hemisphere of $5\,mm$ radius located at the centroid of mitral(tricuspid) annulus. The choice of the centroid of the mitral (tricuspid) annulus as the origin and the size of the interior surface $H$ is motivated by the fact that this area is free of any detailed structures we want to parameterize. The whole pipeline can be seen in the Fig. 4.4.

### 4.3.1 Specification of the Landmark Points

We propose to use the following landmarks for the ventricles: the ventricular apices and two points on the boundary of the septal wall that correspond to the locations where RV is attached to LV. Specifically, we

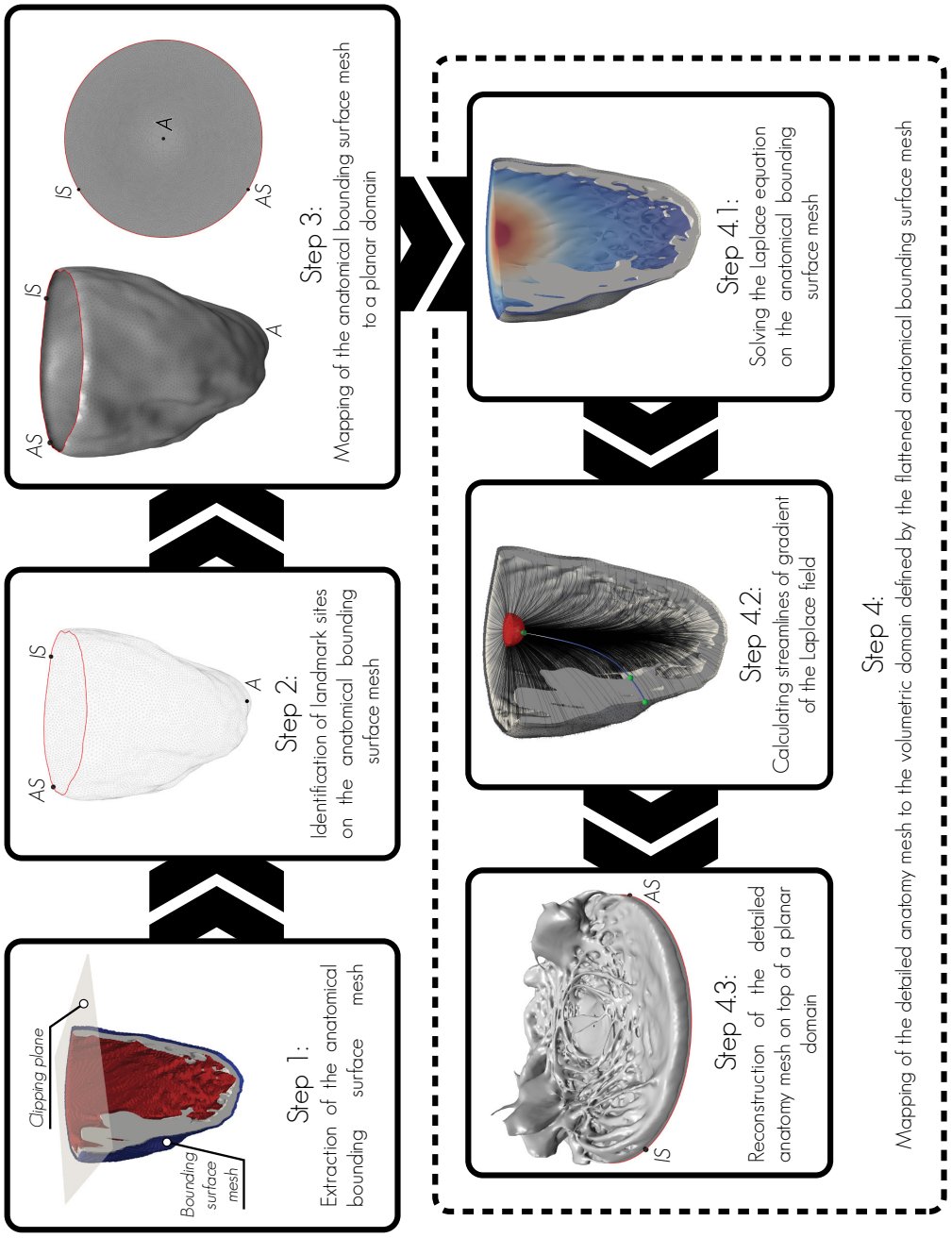


Figure 4.4: Pipeline of proposed method for generation of patient independent representation of ventricles. Landmarks: IS - inferoseptal, AS - anteroseptal, A - apex.

manually define two landmark points $P_{LRV}$ and $P_{RRV}$ at the basal part of the RV ridges which divide the wall into lateral and septal part while all other landmarks are located automatically. From the two manually selected landmark points and the centroid of the LV boundary edge $\partial S_{LV}$ two vectors are constructed and their intersections with $S_{LV}$ are calculated. As those vectors do not necessarily intersect $S_{LV}$ at $\partial S_{LV}$ we locate closest points to intersections points on $\partial S_{LV}$ and use them as the landmarks $P_{LLV}$ and $P_{RLV}$. Both apical landmarks $P_{ARV}$ and $P_{ALV}$ are calculated as the furthest points from the corresponding centroids of the anatomical boundary mesh edges $\partial S_{RV}$ and $\partial S_{LV}$. All the landmarks can be seen in Fig. 4.5.

### 4.3.2 Mapping of the Anatomical Bounding Surface Meshes to the Planar Domain

We chose the following planar domains for the bounding surfaces of the ventricles based on their typical representation encountered in the medical literature: $S_{LV}$ is mapped to a unit disk $D_{LV}$ and $S_{RV}$ to half of another unit disk $D_{RV}$ where their corresponding boundary edges $\partial S_{LV}$ and $\partial S_{RV}$ are mapped to $\partial D_{LV}$ and $\partial D_{RV}$ (Fig. 4.5b)).

However, it is in our interest to map the different subjects' cardiac landmarks $P_{LLV}$, $P_{RLV}$ and $P_{ALV}$ to the same predefined locations on the disk. Thus after mapping $S_{LV}$ to a unit disk $D_{LV}$ (centered at the origin), we calculate the bisector of the angle between the center of the disk and the two septal landmarks $P_{LLV}$ and $P_{RLV}$. Subsequently all the points are rotated to align the bisector with the positive sense of the axis x. The result is shown in Fig. 4.5b). After correcting the orientation we fit the Thin Plate Splines (TPS) to the interior vertices of $D_{LV}$ to displace the apical point $P_{ALV}$ to the center of the disk, leaving the boundary $\partial S_{LV}$ vertices intact. The results of the above mentioned alignment of the landmark points can be seen in Fig. 4.5c).

The half disk shape $D_{RV}$ was constructed from the unit circle centered at $(1.25, 0)$ (this point was chosen for a convenient visualization of both ventricles, assuming $D_{LV}$ is at $(0, 0)$), using only the points whose

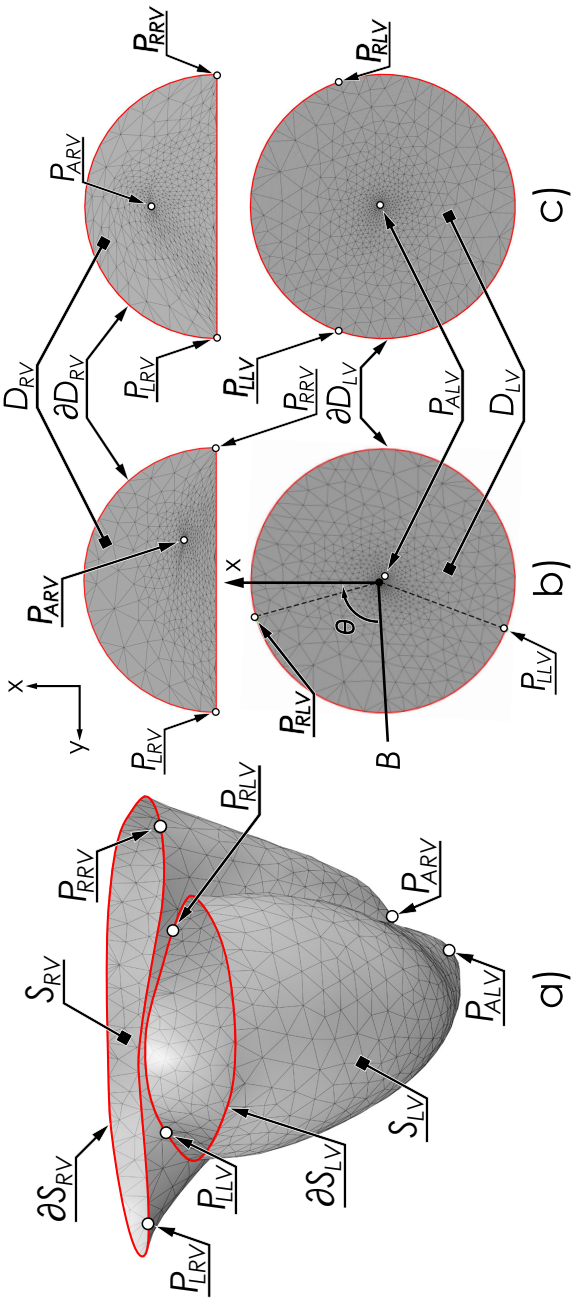


Figure 4.5: Illustration of the mapping procedure of the anatomical bounding surface meshes $S_{LV}$, $S_{RV}$ to the planar domains $D_{LV}$, $D_{RV}$ and alignment of the landmarks in the planar domain. a) Meshes $S_{LV}$, $S_{RV}$ with their corresponding landmarks. b) Meshes $S_{LV}$, $S_{RV}$ mapped to a planar domains $D_{LV}$, $D_{RV}$. c) Alignment of the landmarks to predefined places on planar domain.

$x$ coordinates satisfy $x \geq 1.25$. The procedure of mapping $S_{RV}$ is the same as for $S_{LV}$ except the steps of alignment of landmarks and defining Dirichlet conditions. In this case we place two septal landmarks $P_{LRV}$ and $P_{RRV}$ at the corners of the half disk, namely $P_{LRV} = (1.25, 1)$ and $P_{RRV} = (1.25, -1)$. The apex is again displaced using TPS to a predefined location $P_{ARV} = (1.75, 0)$ (the point in the middle of the lateral and septal boundaries).

### 4.3.3 Improved Visualization of LV Structures

From the Fig. 4.5b) and Fig. 4.5c) we can see that the generated mapping increases the density of the vertices of $D_{LV}$ towards the apex which is visually unpleasant and hampers visual analysis of the information close to the apex. Thus, purely for visualization and for better correspondence of our representation to the AHA regions (Cerqueira et al., 2002), we radially displaced the interior vertices of $D_{LV}$ using the following equations:

$$\begin{aligned} x' &= (x^2 + y^2)^{n/2} \cos[\tan^{-1}(y/x)] \\ y' &= (x^2 + y^2)^{n/2} \sin[\tan^{-1}(y/x)] \end{aligned} \tag{4.11}$$

where $(x, y)$ and $(x', y')$ are the original and modified vertex coordinates. For the value of exponent $n$ we chose $1/3$, which results in a visually more homogeneous distribution of information. Fig. 4.6 illustrates how points at different geodesic distances from the apex are mapped to the flat domain in the case of $n = 1$ and $n = 1/3$. The colors represent different regions of geodesic distance field from an apex calculated on $S_{LV}$. Fig. 4.6a) and b) shows how the distances along the geodesics reduce towards the center, which is corrected in Fig. 4.6c) using (4.11).

### 4.3.4 Mapping of the Detailed Anatomy to Cylinder

After obtaining $\varphi$, that maps meshes $S_{LV}$ and $S_{RV}$ to the corresponding planar domains, we proceed with mapping of the detailed anatomy meshes $M_{LV}$ and $M_{RV}$ to the cylinder defined by the corresponding planar domain as its base.

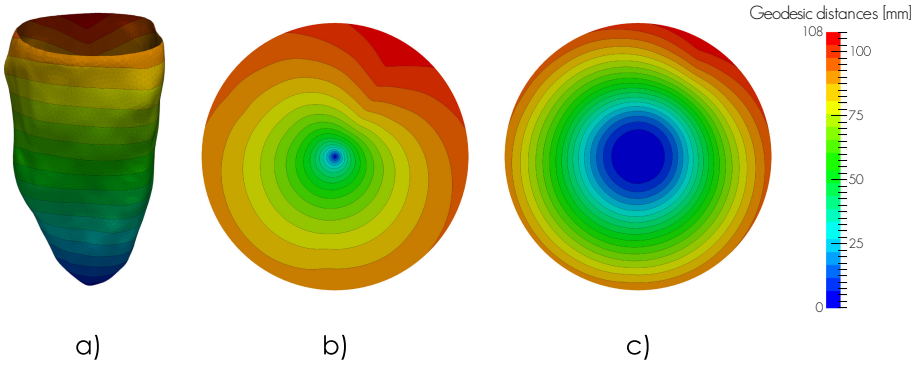


Figure 4.6: Radial displacement of the vertices of $D_{LV}$ for better visualization and correspondence with AHA segments. Colors represent different regions of geodesic distance field from an apex calculated on $S_{LV}$. a) Mesh $S_{LV}$ with calculated geodesic distance field and its isolines. b) Mesh $D_{LV}$ before radial displaced of its inner vertices. c) Mesh $D_{LV}$ after radial displacement of its inner vertices.

The whole procedure is summarized in Algorithm 1, where the enclosing surface $S$ and inner surface $H$ are represented by triangulated meshes. The resulting points $v_N$ define the parameterized surface $N$ – a shell-like object mapped to the reference frame. The application of the Algorithm 1 to the $M_{LV}$ is illustrated in Fig. 4.7.

### 4.3.5 Inverse Mapping and Mapping to a Different Geometry

We require our mapping to be bijective, thus we have to make sure that its inverse exists. To map the parametrized mesh $N$ back to its original shape or any other, we employ the procedure described in Algorithm 2, which simply reverses the steps of the Algorithm 1.

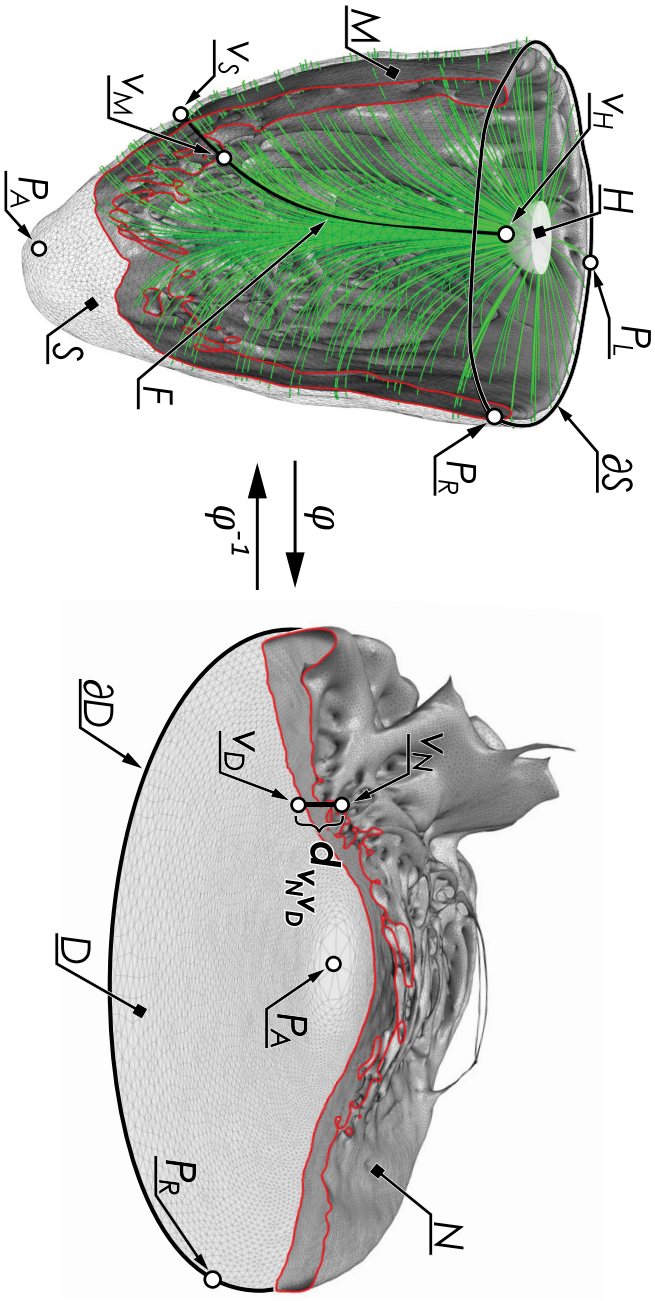


Figure 4.7: Illustration of a mapping procedure of a detailed anatomical LV mesh vertex $v_M$ to the patient independent reference frame.

**Algorithm 1** Mapping algorithm (see Fig. 4.5)

**Input:** Mesh $M$ (surface of volumetric) and $S$ (surface)

1: Define a hemispherical mesh $H$ of a certain radius within $M$ such that the centroid of $\partial H$ coincides with the centroid of $\partial S$
2: Solve the Laplace's equation within the region $S \setminus H$
3: Compute the gradient field of the Laplace's equation solution
4: Map the mesh $S$ to the planar domain $D$
5: **for** each vertex $v_M \in M$ **do**
6: Compute the streamline $F$ that passes through $v_M$
7: Find the intersection point $v_S$ of the streamline $F$ with the mesh $S$ and $v_H$ with $H$
8: Compute the barycentric coordinates of $v_S$ in terms of vertices of $S$
9: Calculate the normalized distance $d(v_M)$ of $v_M$ from $S$ using (4.10)
10: Find the point $v_D$ in $D$ using the barycentric coordinates of $v_S$
11: Place $v_N$ (image of $v_M$) at a distance $d(v_M)$ from the vertex $v_D$ along the normal of $D$.
12: **end for**

**Output:** Mesh $N$ consisting of vertices $v_N$ with the same connectivity as the mesh $M$.

## 4.4 Datasets

### 4.4.1 Synthetic Data

For synthetic data we generated tubular structures with two different regular patterns, circumferential and longitudinal (Fig. 4.8), similar to Karim et al. (2014).

Circumferential tubes (Fig. 4.8a)) are created by clipping the scaled down version of the anatomical bounding surface mesh $S$ by equally spaced planes, that are orthogonal to the long axis. The curves obtained by the clipping were then uniformly subdivided and used as a centerlines of tubular structures. The radius of the tubes was set to $0.7\ mm$.

**Algorithm 2** Inverse mapping algorithm

**Input:** Meshes $N$ (surface or volumetric) and $S$ (surface)

1: Define a hemispherical mesh $H$ of a certain radius within $M$ such that the centroid of $\partial H$ coincides with the centroid of $\partial S$
2: Solve the Laplace's equation within the region $S \setminus H$
3: Compute the gradient field of the Laplace's equation solution
4: Map the mesh $S$ to the planar domain $D$
5: **for** each vertex $v_N \in N$ **do**
6: Cast the ray in a normal direction towards the mesh $D$
7: Find the intersection point $v_D$ of the ray with the mesh $D$ and calculate the distance $d_{v_N v_D}$
8: Compute the barycentric coordinates of $v_D$ in terms of vertices of $D$
9: Find the point $v_S$ in $S$ using the barycentric coordinates of $v_D$
10: Compute the streamline $F$ that passes through $v_S$ and calculate the distance $d_{v_S v_H}$
11: Place vertex $v_M$ (image of $v_N$) along the streamline $F$ at a distance $d = d_{v_S v_H} \cdot d_{v_N v_D}$
12: **end for**

**Output:** Mesh $M$

Longitudinal tubes (Fig. 4.8b)) are created by clipping the same meshes by a plane defined by the ventricle's apices and centroids of the boundary edges. The plane was rotated by $30\ ^\circ$ increments and the curves obtained by the clipping were used as the centroids of the tubes generated using the same parameters as the radial tubes.

### 4.4.2 Human Hearts

#### Image Datasets

We processed six MRI datasets acquired by a $3\ T$ Siemens scanner with $0.44 \times 0.44\ mm$ in-plane resolution and slice thickness of 1 to $1.17\ mm$. The Dicom datasets (Fig. 4.9) were provided by the Visible Heart® Lab-

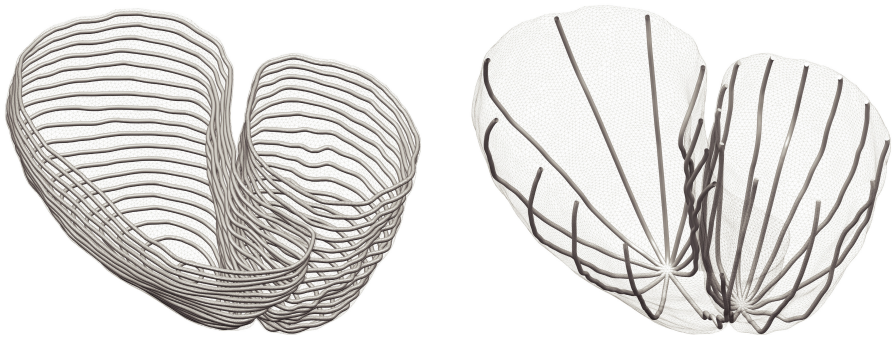


Figure 4.8: Illustration of two different patterns of tubular structures representing synthetic data. a) Circumferential tubes. b) Longitudinal tubes.

oratory, and were obtained by MRI scanning perfusion fixed hearts that were graciously donated by the organ donors and their families through LifeSource. The aorta, trachea, superior vena cava, and the inferior vena cava (when possible) of a given specimen were cannulated and attached to a perfusion fixation chamber as described previously (Anderson et al., 2009, 2008; Eggen et al., 2012; Goff et al., 2015). This approach preserved/fixed each heart in a modified end-diastolic state (atria and ventricles were fully expanded) and also lungs were dilated. The pericardium and phrenic nerves were left intact. These hearts were fixed with $10\ \%$ formalin in PBS solution for at least 24 hours under $40 - 50\ mmHg$ of pressure, and then stored in $10\ \%$ formalin.

**Segmentation**

The meshes of the detailed ventricular anatomy (Fig. 4.10) were generated from the segmentations of the MRI data with the Seg3D image processing software (CIBC, 2015). The segmentations were cut at the basal part of the heart with a plane perpendicular to the LV long axis immediately

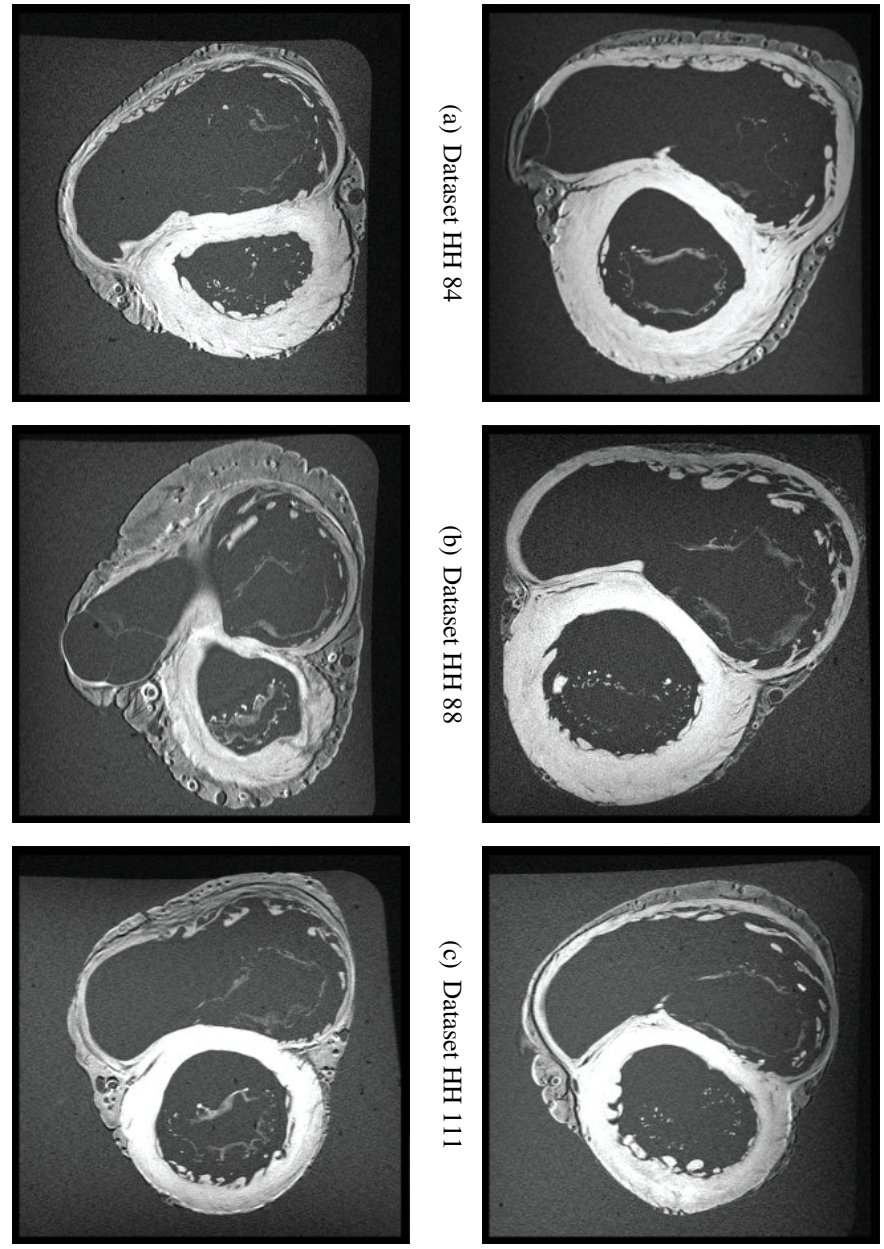

(a) Dataset HH 84 (b) Dataset HH 88 (c) Dataset HH 111

(d) Dataset HH 112 (e) Dataset HH 119 (f) Dataset HH 121

Figure 4.9: Middle stack short axis view slices of MRI human heart datasets.

under the mitral valve and the supraventricular crest. Tendinous chords as part of the valves protruding into ventricular cavities of heart ventricles were removed during the segmentation process of the ventricles. As we are focusing only on the trabeculations, the myocardium was excluded from the segmentations using the following procedure. First the blood pool was segmented and morphological dilation-erosion (Seg3D, CIBC (2015), kernel size $12\ mm$) is applied to obtain an approximation to the concave hull of the trabeculated endocardium. The blood pool image was then subtracted from the concave hull image to obtain final segmentation of detailed cardiac ventricular anatomy. The meshes of the segmentations were obtained in ParaView (Squillacote, 2008) and were smoothed and uniformly remeshed in ReMesh (Attene and Falcidieno, 2006). We used 1 iteration of uniform remesh filter and 3 iterations of Laplacian smooth filter.

**Extraction of the Anatomical Bounding Surface Meshes**

To be able to parametrize the detailed cardiac anatomy meshes $M_{LV}$ and $M_{RV}$, we need to define the domain for solving the Laplace equation in which those meshes will be embedded. The domain is defined by the anatomical bounding surface and the hemisphere placed at the centroid of the boundary of anatomical bounding surface (i.e. the centroid of the mitral/tricuspid valve in our case). From the meshes $M_{LV}$ and $M_{RV}$, we first create a binary volumetric images (1 - detailed cardiac anatomy, 0 - background) of isotropic resolution $0.5\ mm$ and slightly dilate the images by a constant value of $1.0\ mm$ (Visualization Toolkit (VTK) Schroeder et al. (2006), kernel radius of 2 voxels). The dilation is required to avoid the intersection of this bounding surface, used to define the mapping, and the structures to be mapped. From the dilated images we extract the boundary surfaces by the Marching Cubes algorithm (Lorensen and Cline, 1987). The extracted surfaces are then smoothed with VTK's window sinc filter and uniformly remeshed.

The next step is to introduce a cut separating the extracted surface into two parts. The cut is introduced at the highest point of the basal rim of

(a) HH 84 mesh (b) HH 88 mesh (c) HH 111 mesh

(d) HH 112 mesh (e) HH 119 mesh (f) HH 121 mesh

Figure 4.10: Meshes corresponding to the segmentations, representing only the trabeculated layer.

the extracted surface by clipping it with a plane orthogonal to the LV long axis, such that the surface is divided into two parts: an inner part, which is in contact with the blood pool and will be discarded, and an outer part, which will represent our enclosing surface $S$. (Fig. 4.4 Step 1). The outer part surface is then isolated and smoothed. The enclosing surfaces are then uniformly remeshed and taken as $S_{LV}$ and $S_{RV}$. Lastly we compute the boundaries (curves) $\partial S_{LV}$ and $\partial S_{RV}$ of $S_{LV}$ and $S_{RV}$.

## 4.5 Results

### 4.5.1 Algorithm Performance

Our mapping method relies on the solution of the Laplace's equation of discretized volumetric domain between the meshes $H$ and $S$. The streamlines of the gradient of the Laplace's equation solution allows us to map every point inside the discretized domain. Thus the error introduced by our mapping procedure will depend on the resolution of the discretized domain. The Laplace's equation was solved iteratively until the update between consecutive iterations for every point of the domain was smaller than or equal to a predefined threshold $\epsilon = 0.0001$. The execution time of our C++ implementation of the mapping algorithm and its reconstruction error were executed on a SNOW Linux Cluster equipped with AMD Opteron Abu Dhabi 6378 processors.

We analyzed how the performance changes with the voxel size of the discretized domain and the relationship between the speed and the reconstruction accuracy. The experiment was carried out on the dataset *HH 111* (see Fig. 4.9). The voxel sizes ranged between $0.3$ - $1.2$ $mm$ in the steps of $0.1$ $mm$ where the maximum value was chosen to be slightly bigger than the maximum slice thickness of our datasets. The reconstruction error is defined as Euclidean distance between vertices of mesh $M$ and their corresponding vertices of a mesh $M$ that underwent direct and inverse transformation $\psi^{-1}[\psi(M)]$. In Fig. 4.11 we show the calculated reconstruction errors and execution times for the whole direct mapping procedure and the time necessary to calculate the solution of the Laplace's

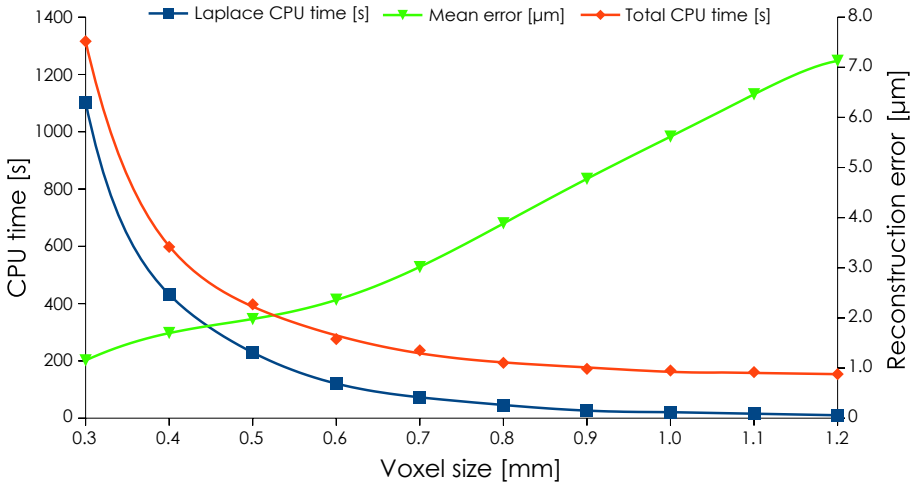


Figure 4.11: Reconstruction errors and execution times of the algorithm with respect to the size of the voxels.

equation.

As expected, the reconstruction error increases with the increase of the voxel size of discretized domain while the time to obtain the map and the time to solve the Laplace's equation decreases.

### 4.5.2 Reconstruction Accuracy Measure

In all the following experiments we measure the accuracy of our algorithm in terms of mesh *reconstruction*. The measurement is carried out by applying the direct and inverse transform $\psi$ to the mesh $M$ and calculating the average point to point distance between $M$ and $\psi^{-1}[\psi(M)]$.

### 4.5.3 Analysis of the Distortion Caused by the Mapping

#### Distortion due to the Direct Mapping

It is known that although the conformal flattening preserves angles locally, it will introduce some distortion globally. The distortion could also increase due to the use of the TPS for the left ventricle. In this experiment we wanted to assess visually the distortion introduced by the proposed method applying it to synthetic data – tubular structures with two different regular patterns: circumferential and longitudinal, similar to Karim et al. (2014). Both tubular structure arrangements were then mapped according to the proposed method.

From the Fig. 4.12 one can observe that the more the radial or circumferential curvature of the bounding mesh $D$ deviates from the one of the ellipsoid the higher will be distortion in that direction, namely there will be radial or circumferential inhomogeneities in the planar domain. Circumferential inhomogeneity can be seen in the case of LV circumferential tubes. The mapped circumferential tubes generally nicely follow the perimeter of the disk, but when approaching the apex we can observe radial inhomogeneities due to higher deviation of the mesh curvature from the curvature of the ellipse. In the RV we can observe that the tubes nicely follow the shape perimeter in lateral part, while they get more stretched when approaching RV ridges (lines connecting the apex and the reference landmarks at shape corners). Also, there is higher distortion of the tubes in the septal part caused by the stretch of ventricular septal wall.

The longitudinally oriented tubes in LV and RV also slightly deviate from straight lines. Again, this is caused by regional deviations from an ellipsoid. Those inhomogeneities are more pronounced in the LV than in the RV because of the applied radial displacement of the vertices of the disk domain due to (4.11), thus artificially compressing the vertices towards the basal segments. The longitudinal tubes in the RV planar domain deviate from straight lines due to higher stretch of the surface towards the boundary. Such inhomogeneities are particularly visible in the septal part where certain tubes make sharper turns due to the high stretch of the basal part of the septal wall close to the boundary. As the vertices of RV are not

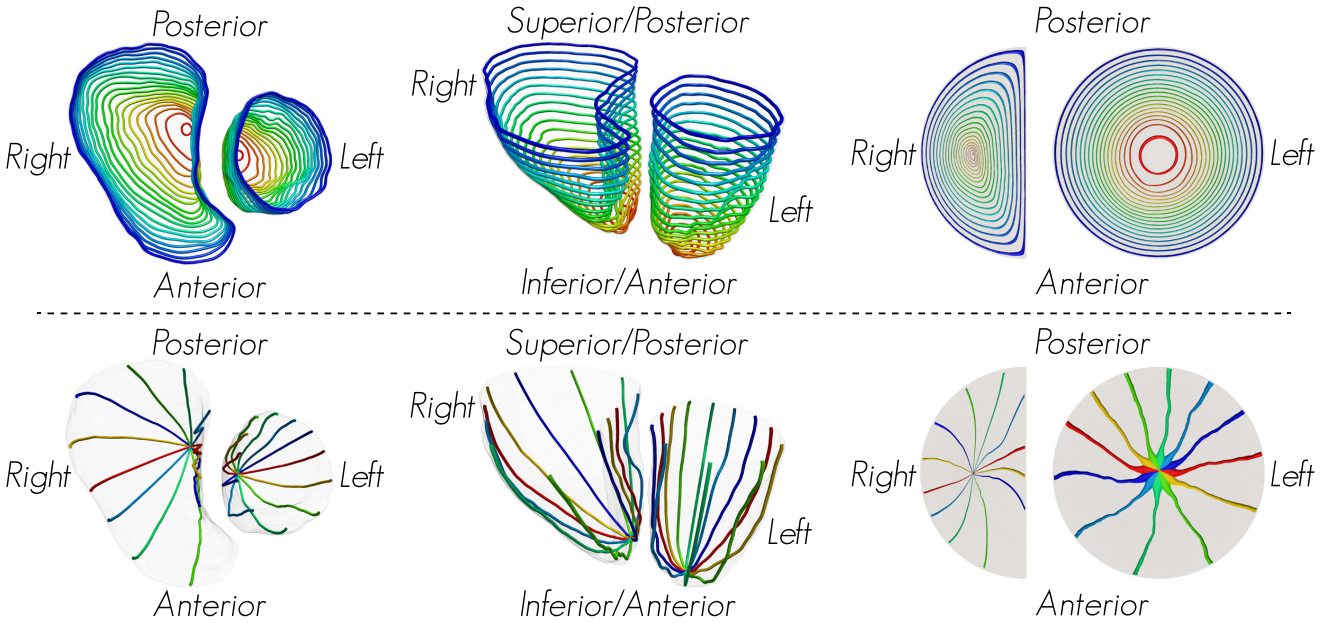


Figure 4.12: Mapping of synthetic data. The synthetic tubular structures were colored differently to aid visualization. The circumferential tubes (top row) are colored according to their position along the long axis, while the longitudinal tubes (bottom row) are colored according to the angle of the defining plane.

| | HH84 | | HH88 | | HH111 | | HH112 | | HH119 | | HH121 | | AVERAGE |
|---|---|---|---|---|---|---|---|---|---|---|---|---|---|
| | LV | RV | LV | RV | LV | RV | LV | RV | LV | RV | LV | RV | |
| Mean distance [$\mu m$] | 1.24 | 1.75 | 1.28 | 1.31 | 1.15 | 1.70 | 1.84 | 1.40 | 1.84 | 1.50 | 1.21 | 1.56 | 1.48 |
| Median distance [$\mu m$] | 0.80 | 1.15 | 0.81 | 0.90 | 0.85 | 1.16 | 1.23 | 0.92 | 1.25 | 0.97 | 0.70 | 1.02 | 0.98 |
| Standard deviation [$\mu m$] | 1.78 | 2.13 | 1.86 | 1.64 | 1.81 | 2.11 | 2.21 | 1.76 | 2.16 | 1.86 | 1.95 | 2.05 | 1.94 |

Table 4.2: Mean, median and standard deviation of the reconstruction errors for each mesh.

displaced radially outwards (as was done in LV) the longitudinal tubes appear to be more smooth than in LV.

We would like to emphasize that, although the direct map can introduce above mentioned inhomogeneities, the introduced distortions will disappear when we map those structures back to the patient anatomy.

**Distortion due to Direct and Inverse Mapping**

Since the process of mapping involves discretization of the volumetric domain enclosed by the anatomical mesh $S$, we expect some error to be introduced by the discretization. In this experiment we analyze this distortion by calculating the direct and inverse transform and analyzing the reconstruction error for all the anatomical meshes (Fig. 4.10). Fig. 4.13 depicts the reconstruction errors.

To obtain the direct and inverse transform of the $M$ meshes we calculated the solution to the Laplace's equation using a threshold value $\epsilon = 0.0001$ on the corresponding volumetric domains which we discretized to voxels of isotropic size of $0.3\ mm$. This voxel size was chosen to have the highest resolution of the volumetric domain without increasing too much the computational requirements (going below $0.3\ mm$ required significantly more computational resources and time).

The mean and median reconstruction error for each ventricle, together with their standard deviations, are shown in Table 4.2. The maximum reconstruction error between any given pair of vertices is $35.0\ \mu m$, while the average mean and median reconstruction errors are $1.40$ and $0.88\ \mu m$ with the average standard deviation of $1.90\ \mu m$.

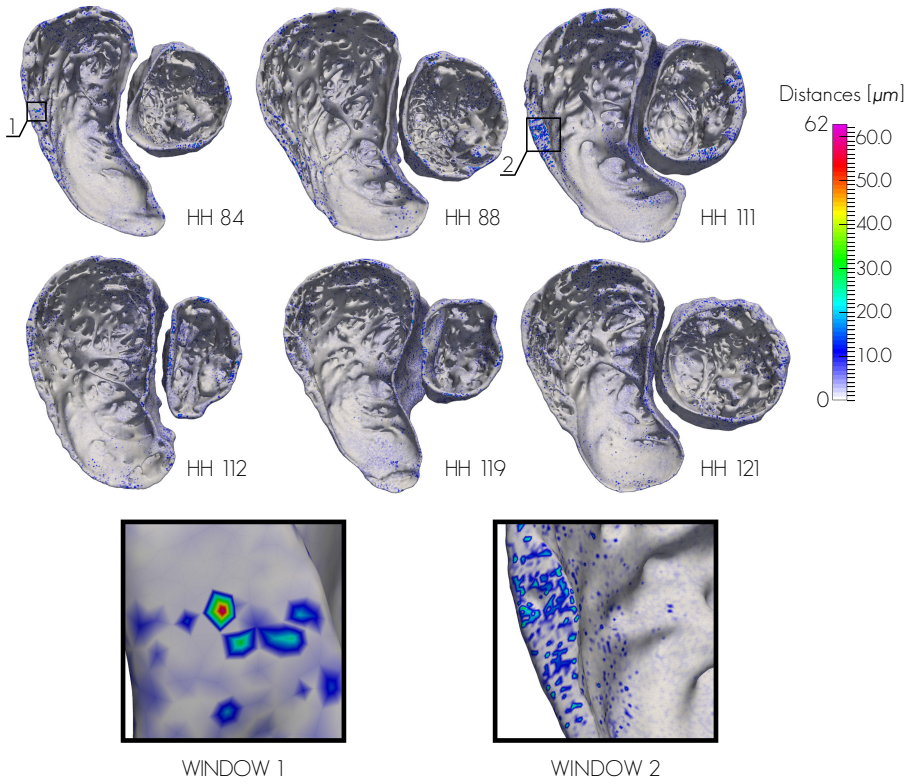


Figure 4.13: Reconstruction error per vertex. The reconstruction error is calculated as the vertex to vertex distance between original $M$ meshes and their corresponding instances after direct and inverse transform. The maximum was observed only in the RV mesh of *HH 84* dataset. Window 1 depicts the region of interest of the *HH 84* dataset's RV, showing the location of the highest error. Window 2 is the closeup of the region of interest of *HH 111* dataset's RV. One can notice that *per vertex* reconstruction errors of higher values are very localized over the meshes.

### 4.5.4 Landmark Placement Sensitivity

Our method relies on the selection of three landmark points on the anatomical bounding surfaces $S$, thus we investigated the impact of the inaccuracies of their localization. In the following experiments we used the reconstruction error, however the inverse map was calculated using the landmarks displaced with respect to the ones used for the direct transform. This approach simulates the scenario when two hearts are mapped to our patient independent representation with inexact landmark placement, except that since the same mesh is used, the change can be easily calculated.

We simulated three types landmark placement inaccuracies (in all the schemes the landmarks were displaced by fixed distances of $1$, $3$ and $5\ mm$):

- One of the boundary landmarks is displaced from the optimal position.
- Both boundary landmarks are displaced towards each other or in the opposite direction.
- The apical landmark is displaced.

In the first scheme, we displaced one boundary landmark at a time: $P_{LLV}$, $P_{RLV}$ on $S_{LV}$, and $P_{LRV}$, $P_{RRV}$ on $S_{RV}$ (LV and RV independently), while keeping the other two landmarks on $S$ fixed. Every moving landmark was displaced $1$, $3$ and $5\ mm$ clockwise and counter-clockwise along the boundary $\partial S$.

The second scheme consisted of simultaneously moving both boundary landmarks: $P_{LLV}$ and $P_{RLV}$ on $S_{LV}$, and $P_{LRV}$ and $P_{RRV}$ on $S_{RV}$, while keeping the apical landmark fixed. The boundary landmarks were displaced simultaneously $1$, $3$ and $5\ mm$ towards and away from each other along the boundary $\partial S$.

In the last scheme we displaced only the apical landmarks $P_{ALV}$ and $P_{ARV}$, while keeping the boundary landmarks fixed. These landmarks

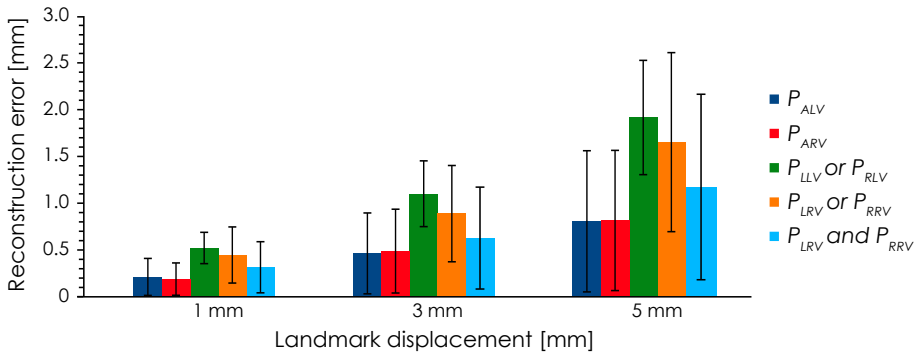


Figure 4.14: Average reconstruction errors with respect to the landmark displacement. Error bars represent one standard deviation. Plots labeled $P_{ALV}$ and $P_{ARV}$ show the reconstruction error when one of the apices is displaced; “$P_{LLV}$ or $P_{RLV}$” and “$P_{LRV}$ or $P_{RRV}$” correspond to the displacement of one of the boundary landmarks of RV and LV respectively; “$P_{LRV}$ and $P_{RRV}$” corresponds to the displacement of both boundary landmarks of the RV.

were displaced $1$, $3$ and $5$ $mm$ in four directions (orthogonal) along the surface.

Fig. 4.14 shows the average reconstruction error for different landmark displacement schemes and distances. As expected, the reconstruction error in both ventricles increases with the increase of the landmark displacement up to half the displacement magnitude.

Fig. 4.15 depicts the *per vertex* reconstruction error for a scheme where just the $P_{LLV}$ and $P_{LRV}$ were displaced counter clockwise along their boundaries. In the RV one can notice that the error is increasing both vertically from the apex $P_{ARV}$ and laterally around the wall from the $P_{RRV}$ towards the displaced landmark $P_{LRV}$. In the LV there is just vertical increase of the error from the apex $P_{ALV}$ towards $P_{LLV}$, while laterally around the wall the errors have similar values. From the figure we can observe that the error in the placement of one of the RV bound-

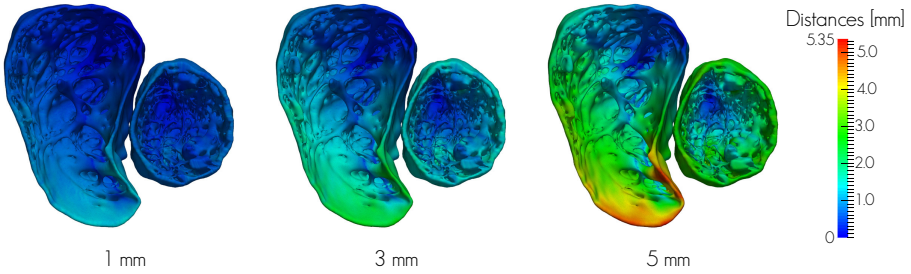


Figure 4.15: Reconstruction error per vertex for displacement of left boundary landmarks $P_{LLV}$ and $P_{LRV}$ for 1, 3, and 5 $mm$ (view from the top, *HH 88* dataset). Note the localized error in the RV and the uniformly spread errors in LV.

ary landmarks leads to the inaccuracies limited to the neighborhood of the landmark. The neighborhood also increases with the magnitude of the displacement, affecting larger part of the RV with 5 $mm$ displacement. In the case of LV, the change in one landmark $P_{LLV}$ changes the location of the bisector (see Subsection 4.3.2), which leads to the rotation of the ventricle. This rotation introduces radially uniform distortion, affecting mostly the structures in the basal parts of the LV.

In Fig. 4.16 we show *per vertex* reconstruction errors introduced by simultaneous displacement of the boundary landmarks $P_{LRV}$ and $P_{RRV}$ towards each other along the $\partial S_{RV}$. One can observe a vertical increase of the errors from the apex $P_{ARV}$ towards $P_{LRV}$ and $P_{RRV}$, while laterally they decrease around the wall from $P_{LRV}$ and $P_{RRV}$ towards the middle of septal and lateral wall. Again, we observe that the error in the placement of boundary landmarks leads to inaccuracies limited to the neighborhood of the landmarks, while the neighborhoods increase with the magnitude of the displacement.

In case of the LV, the visualization of the reconstruction errors on *HH 88* is omitted, as the left ventricles have shown invariance to this scheme of landmark displacement. The displacement of $P_{LLV}$ and $P_{LRV}$ gave

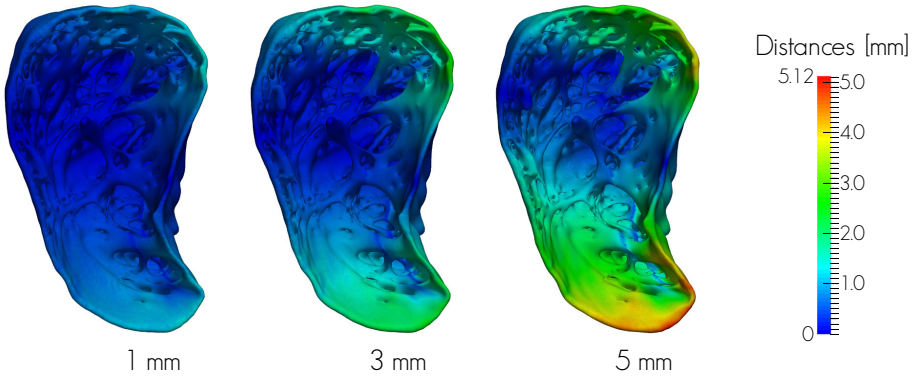


Figure 4.16: Reconstruction error per vertex for displacement of left and right boundary landmarks $P_{LRV}$ and $P_{RRV}$ simultaneously for 1, 3, and 5 $mm$ towards each other (view from the top, *HH 88* dataset).

the same result as for the case when landmarks are not displaced at all (Fig. 4.13). The invariance to the simultaneous displacement of $P_{LLV}$ and $P_{RLV}$ is caused by the fact that such displacement of the landmarks does not change the location of a bisector (see Subsection 4.3.2, Fig. 4.5), thus giving us the same reconstruction errors as in case of keeping the landmarks in place.

In the last displacement scheme, depicted in Fig. 4.17, we see that displacing the apical landmarks $P_{ALV}$ and $P_{ARV}$ cause the increase of *per vertex* reconstruction error towards the apex. As the boundaries are intact, there is no change in the reconstruction errors in lateral direction. The placement of apical landmarks leads to the inaccuracies limited to the apical region, while the neighborhood is again increasing with the magnitude of the displacement.

### 4.5.5 Application to the Human Hearts

We applied our method to twelve detailed anatomy meshes $M$ (6 of right and 6 of left ventricles) and show their corresponding normalized anatom-

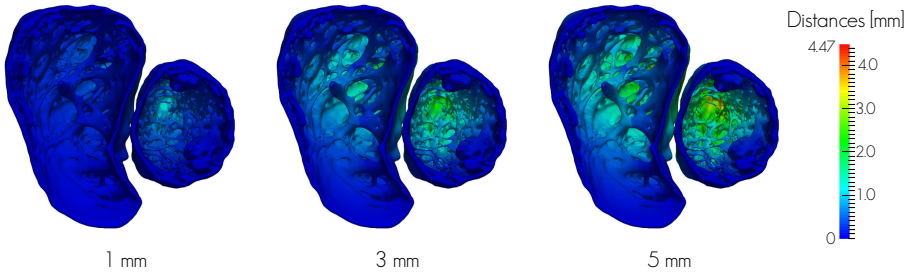


Figure 4.17: Reconstruction error per vertex for displacement of apical landmarks $P_{ALV}$ and $P_{ARV}$ for 1, 3, and 5 $mm$ (view from the top, *HH 88* dataset).

ical meshes $N$ (Subsection 4.5.5). As our mapping is bijective, it allows to map the $N$ meshes to any arbitrary shape represented by its anatomical bounding surface mesh $S$. Thus as an example in Subsection 4.5.5 we show the results of mapping of the $N$ meshes to a hemisphere.

### Mapping of the Human Heart Datasets to the Normalized Anatomical Reference Frame

The results of the proposed method are demonstrated on twelve extracted detailed anatomical meshes $M$ shown in Fig. 4.10. As mentioned in subsection 4.2.4, the RV detailed anatomical meshes were mapped to the normalized reference frame defined by half a cylinder of unit height and with the base being half the unit disk, while LV meshes are mapped to the volumetric domain defined by a unit cylinder, namely a cylinder of a unit disk base and unit height. The Fig. 4.18 depicts the obtained results.

In the Fig. 4.18 we can observe the intricate trabecular morphology inherent to each subject. An increase in the amount of trabeculations as we move from the base towards the apex can be seen in both ventricles. The basal part of the septal walls is free of trabeculations and they start to emerge in their middle parts while, on the lateral wall, we have them

present along the whole wall. The trabeculations, present in the basal part of the lateral walls, are attached to the wall along their whole length and they form big prominent ridges. The moderator bands are clearly visible and traversing through the RV cavities. In the RV, there are more trabeculae traversing through the cavity and trabeculae emerging from opposite sides of the ventricle and fuse together to form the papillary muscles. The coarseness of trabeculations or "sponginess" of the heart increases towards the apex. That coincides with the observations reported in the literature of a highly trabeculated apical region where trabeculations form a complex interwoven network.

### Inverse Mapping and Mapping to Different Subject Geometries

The proposed bijective map $\psi$ provides means to map any detailed anatomical mesh $M$ to a patient independent volumetric domain defined by the chosen planar domain as a base and unit height. Calculating such bijective map for different instances of the detailed patient anatomy allows us to map the anatomy of one patient to any other reference frame and vice versa.

The visualization in a volumetric domain with planar base may not be very visually pleasing due to trabeculas and moderator band traversing though ventricular cavities. Fig. 4.19 shows an alternative visualization, where the detailed anatomy meshes are mapped onto the domain defined by a hemisphere.

### Mapping of Human Heart Datasets Including Inflow and Outflow Tracts

In this chapter we used the segmentations of the LV and RV detailed cardiac anatomy, which were cut by a plane perpendicular to the LV long axis immediately under the mitral valve and the supraventricular crest. However the proposed approach can also be used if the parameterization up to the inflow and outflow tracts is required (such as the one used in Young et al. (2011)).

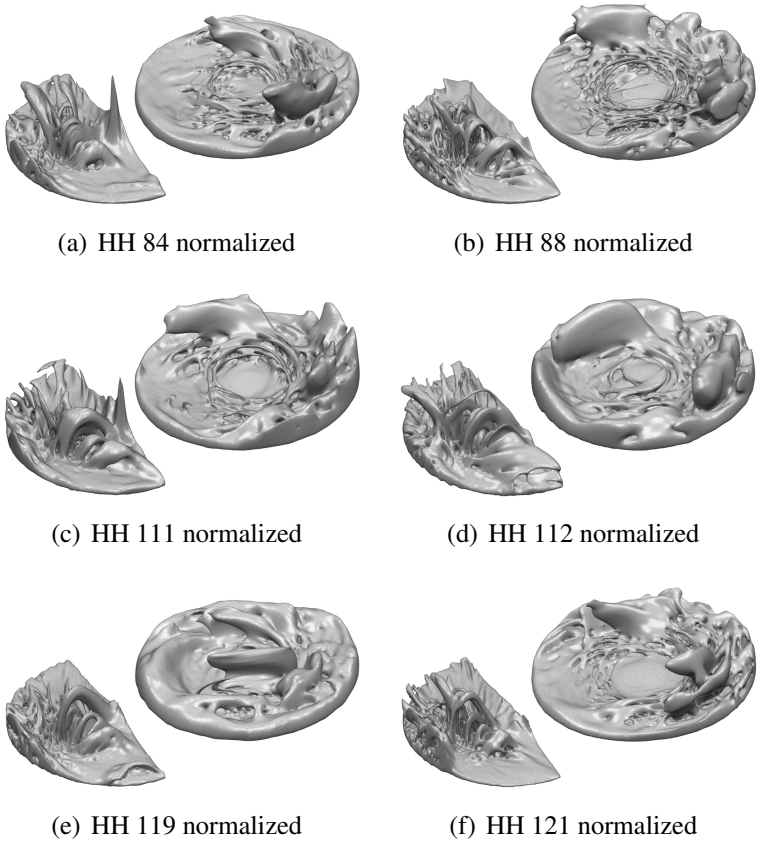

(a) HH 84 normalized (b) HH 88 normalized

(c) HH 111 normalized (d) HH 112 normalized

(e) HH 119 normalized (f) HH 121 normalized

Figure 4.18: Detailed anatomical meshes $M$ mapped to the proposed normalized anatomical reference frame.

In its proposed form, the parameterization is limited to geometries with only one opening. This limitation is based on the idea that such geometries can be conveniently flattened into a disk. However if more than one opening is present, as in the case of inflow and outflow tracts of the right ventricle (as in Gilbert et al. (2015)) the proposed approach can be modified in two ways: use one of the holes as the boundary and leave the other hole in the interior of the flat disk, similarly to Tobon-Gomez

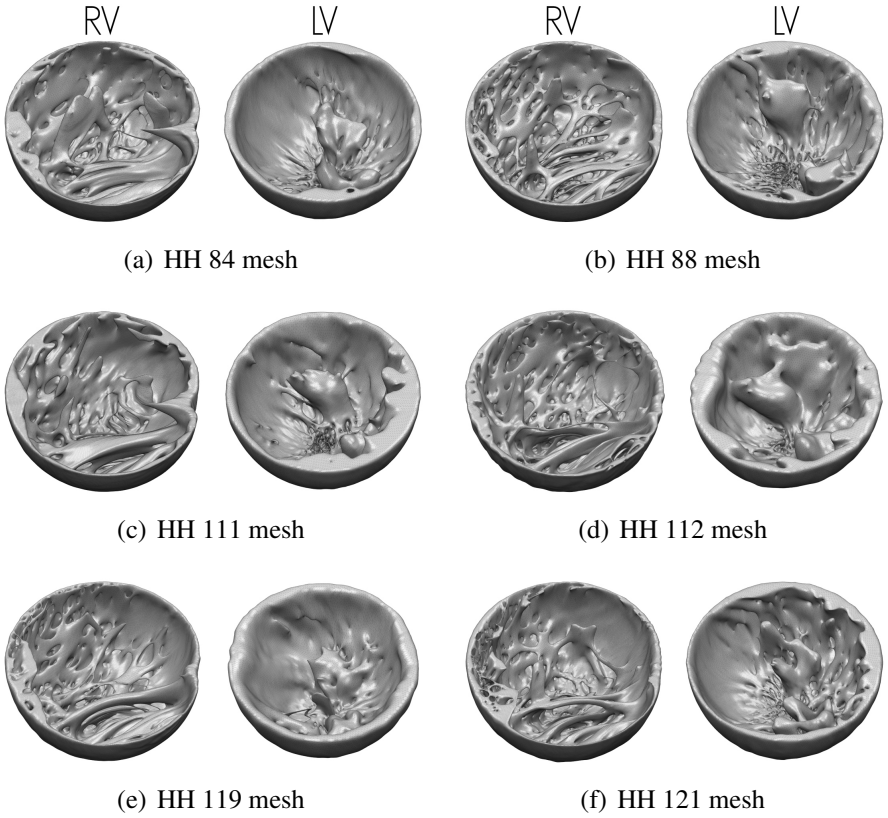


(a) HH 84 mesh (b) HH 88 mesh

(c) HH 111 mesh (d) HH 112 mesh

(e) HH 119 mesh (f) HH 121 mesh

Figure 4.19: Mapping of detailed anatomical meshes $M$ to a hemisphere.

et al. (2015); or if the 2D visualization is not crucial, the parameterization can also be achieved by mapping the whole chamber to a spherical shell using exactly the same methodology with an additional registration step to make sure the holes match on the sphere.

As an illustration, in Fig. 4.20 we show two LVs segmented up to the valves, and mapped to each other's bounding surface. Fig. 4.20a), d) depict ventricles of *HH 84* and *HH 88* segmented up to the aortic and mitral valves. Their segmentations were cut with two planes placed thorough aortic and mitral annuli. Fig. 4.20b), e) depict *HH 88* LV mapped

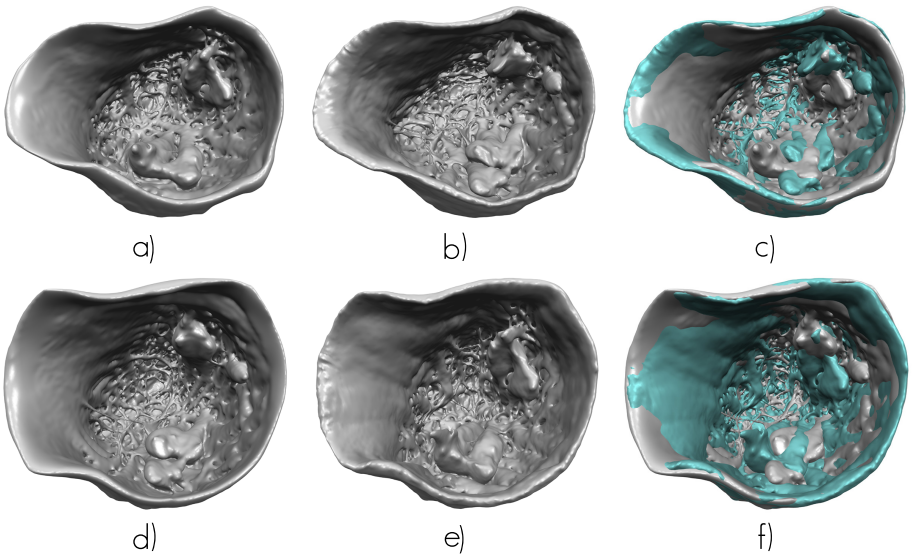


Figure 4.20: Illustration of LV of *HH 84* and *HH 88* datasets including inflow and outflow tracts, and them mapped onto each other’s bounding surface. a) Original *HH 84* LV mesh. b) Mesh *HH 88* LV mapped onto *HH 84* LV bounding surface. c) Overlap of a) (gray color) and b) (turquoise color). d) Original *HH 88* LV mesh. e) Mesh *HH 84* LV mapped onto *HH 88* LV bounding surface. f) Overlay of of d) (gray color) and e) (turquoise color).

to *HH 84* LV and vice versa, while Fig. 4.20c), f) displays the overlap of Fig. 4.20a (gray color) with Fig. 4.20b (turquoise color) and Fig. 4.20d (gray color) with Fig. 4.20e (turquoise color).

**Relationship to the Bulls-eye Plot**

In this section we discuss the relationship of the proposed mapping to a bulls-eye plot using the 17 AHA segments (Fig. 4.21). For the illustration we partitioned the LV meshes of the datasets *HH 84* and *HH 88* (Fig. 4.22 left side) into 17 segments using the method proposed by Cerqueira et al.

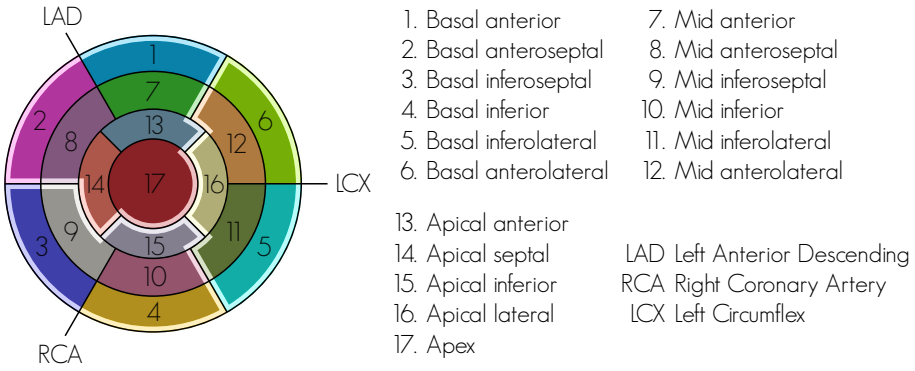


Figure 4.21: Illustration of 17 AHA segments and the coronary artery regions with corresponding names and colors used in the text.

(2002) and our method:

- *Cerqueira with equal partition*. The first and fourth row of Fig. 4.22 represent the segmentation into 17 segments obtained by equal partitioning as proposed by Cerqueira et al. In this case, the ventricle is divided into 3 equal regions between mitral valve plane and the end of a cavity. The apical cap is defined as the area beyond the end of the cavity. The slices were defined by a plane perpendicular to the long axis (the line from the apex to the center of the mitral valve). The basal and mid-cavity slices were then divided into 6 equal segments of $60\ ^\circ$. The first plane is defined by the long axis and the point in mid septum, while the other two are rotated $60\ ^\circ$ with respect to it. The 4 segments of the apical slice are defined by 2 orthogonal planes, where the first one makes $45\ ^\circ$ with respect to the mid septum.

- *Cerqueira partitions using landmarks*. The second and fifth row in Fig. 4.22 represent the ventricular segments defined using an alternative definition by Cerqueira et al., via specific landmark points.

Basal, mid-cavity, and apical vertical long axis slices were then defined by a plane perpendicular to the long axis: the basal slice was defined as the area from the tips of the papillary muscles to the mitral annulus; the mid-cavity was defined as the region that includes the entire length of the papillary muscles; the apical slice was defined from bellow the roots of the papillary muscles to just before the cavity ends; and the apical cap was defined as the area of beyond the end of the left ventricular cavity.

The six myocardial segments of basal and mid-cavity slices are then defined by three planes. The first plane is defined by the long axis and a point where the right ventricular wall attaches to left ventricular wall in the anterior side of a heart. The second plane is defined in the same way except the point is located at the heart's inferior side. The third plane is defined by the long axis and a point located radially between the first and second plane.

The four apical slice segments are defined by two orthogonal planes passing though the long axis. The first plane is defined as a plane rotated $45\ ^{\circ}$ from the mid septum and the second is orthogonal to the first.

- *Equally sized regions in the flattened domain*. The third and sixth rows of Fig. 4.22 depict the partition of the datasets into 17 segments obtained by our method. First we map the datasets to our proposed reference system and then transfer the segment labels information from the disk subdivided into regions as in Fig. 4.21. The labels are then mapped back to the original reference mesh and displayed.

The right side of Fig. 4.22 shows *HH 84* and *HH 88* LVs labeled using the above methods and mapped onto each other's bounding surfaces.

Strictly following the landmark information proposed by Cerqueira et. al. for defining the planes can be ambiguous, especially in case of high resolution images. As the roots and the tips of the papillary muscles are not located in the same plane perpendicular to the long axis, positioning of

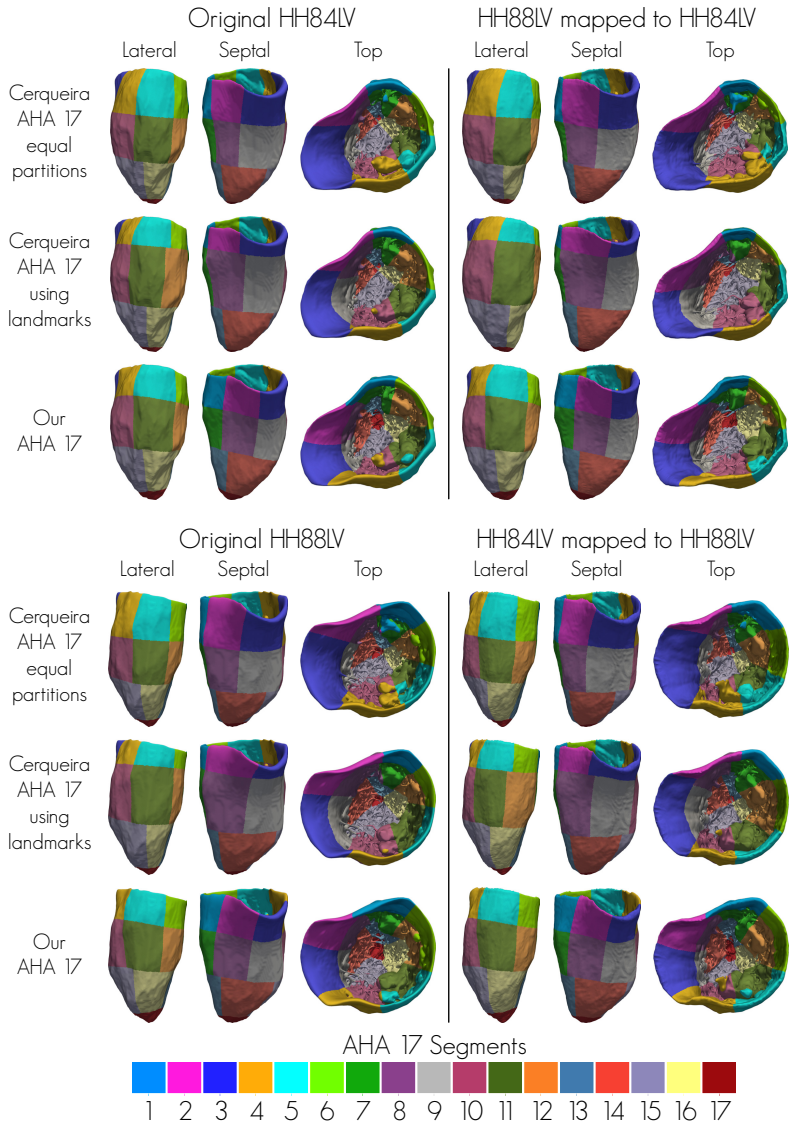


Figure 4.22: Partition of *HH84* and *HH88* LV meshes into 17 AHA segments and them mapped onto each other’s bounding surfaces.

those planes is ambiguous and will lead to highly nonuniform longitudinal length of the regions. Such result can be seen in the second and fifth row of Fig. 4.22. Furthermore, defining the roots of the papillary muscles is subject to variability due to the fact that there are many trabeculations, which merge together to form the papillary muscles at different levels.

The planes separating the septum from the LV anterior and inferior free walls are defined by the long axis and the location of attachment of the RV wall to the LV. Those locations vary along the long axis and will lead to the nonuniform definition of radial basal and mid-cavity segments.

If we follow additional guidelines proposed by Cerqueira et al. we can achieve more uniform segments as can be seen in the first and fourth row of Fig. 4.22. One can observe that partitioning by our method (Fig. 4.22, third and sixth row) produces similar results as obtained by the one proposed by Cerqueira et al. when the uniform partition is enforced.

Fig. 4.23 depicts *HH 84* and *HH 88* LVs AHA 17 segment information represented in our proposed reference frame. The first column represents the AHA segments obtained by Cerqueira method enforcing uniform partitions, the second column – AHA segments obtained by strictly following landmark locations proposed by Cerqueira et al., and the third column represents AHA segments defined by our method. We want to mention that with our method one can easily redefine the cardiac regions in any way by simply defining them on the disc, after that the regions can be easily mapped back onto any cardiac geometry. Furthermore, our method allows partitioning the ventricles in a transmural direction by labeling additional segments at different depths from the endocardium in the normalized representation.

## 4.6 Discussion

The proposed mapping allows us to define a patient independent reference frame, where populational statistical analysis can be performed or which can be used to map the detailed cardiac anatomy from one heart to another (represented by a smooth surface). To define the reference frame, we

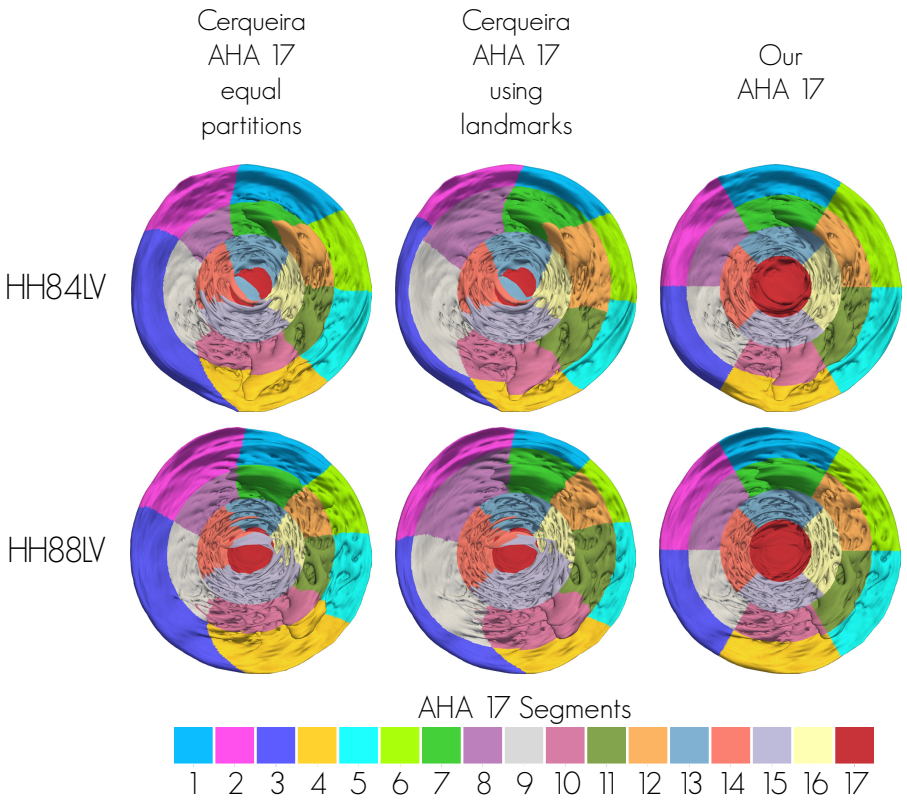


Figure 4.23: Partition of *HH84* and *HH88* LV meshes into 17 AHA represented in normalized reference frame.

chose a cylindrical volumetric domain of unit height and a unit disk base for the LV, while for the RV we chose a half cylinder domain of unit height and a half disk base as defined in section 4.2.3. The choice of the unit half disk and the unit disk as a the base parametric domain was motivated by the fact that such domains are already used by many authors for the visualization of any LV and RV information in the form of a bulls-eye plot (Cerqueira et al., 2002).

In relation to other approaches for ventricle re-parameterization, it is

worth to note two general frameworks: use of prolate spheroidal coordinates and volumetric mesh fitting.

The prolate spheroidal coordinates such as used by Young et al. (2011) provide an interesting alternative to Cartesian coordinates as they allow to characterize any point on the elliptical surface in terms of 4 parameters: two of them related to the size of the ellipsoid and two angles (related to longitudinal and circumferential position of the point on the surface). Aligning this coordinate system with the cardiac left ventricle would allow representing every point on the cardiac surface using two parameters. However it should be noted that neither of cardiac ventricles is elliptical, especially the right ventricle, thus limiting the advantages of using the prolate spheroidal coordinates instead of Cartesian. On the other hand, just in our case, expressing cardiac data using prolate spheroidal coordinates would require aligning the coordinate system with the ventricle by defining the long axis and some landmarks (for example, the centroids of valves).

On the other hand the finite element models, such as used in Young et al. (2011); Gilbert et al. (2015), are more versatile in terms of parameterization and can be used to represent the whole of the cardiac chambers up to the valves with any number of holes. In this case, the point correspondence across the population is established using registration techniques or model fitting to an image. There are however certain drawbacks to using meshes for patient independent representation. The meshes based on Bézier and Hermite elements are limited to ventricles with smooth walls – having trabeculations adds topological variability to the mesh and hampers establishing point correspondence. On the other hand using tetrahedral or hexahedral meshes might be a better option for representing the meshes with varying topology, but again establishing correspondence in the face of varying topology is not trivial. It should be noted though that the mesh representations could be used to define a domain that encloses the trabeculations, reducing the problem of establishing correspondence to the one we have proposed in this chapter.

We want to emphasize that our method is not limited to the mentioned planar domain shapes. The user can use a planar domain of any shape that

is the most convenient or suits best for the job. In particular, in situations where one is not interested in visualization or analysis of the detailed cardiac anatomy, but solely in transferring such anatomy from one case to another, or to include it in a model which does not posses such structures, one can use the same, circular, planar domain for both ventricles. The method proposed here is a generalization of our previously proposed parameterization method for the LV (Paun et al., 2015). It represents accurate and invertible mapping defined at every point inside both cardiac chambers and is not limited to any particular geometry of the chamber. Every point inside the cardiac chamber is characterized by 3 anatomically independent coordinates: two coordinates characterizing the point's projection onto the smooth anatomical bounding surface of the chamber and distance to that surface (longitudinal, circumferential positions and the depth).

The major challenge in the calculation of the coordinates is the calculation of the depth within myocardium, as depending on the shape of the cavity, trivial approaches like taking the distance along the normal will not work (this is especially true for the RV shapes). To deal with that challenge, the proposed method calculates a non-divergent vector field inside the chamber showing the flow from the bounding surface to the centroid of the mitral (tricuspid) annulus. This is achieved by solving the Laplace's equation in the interior of the chamber. The depth is then calculated from the distance along the corresponding streamline, thus providing an invertible mapping for any interior point independently of the geometry.

The main limitation of our method is the use of a discretized domain for the solution of the Laplace's equation. Normally, there is a high density of the streamlines close to the centroid of the mitral or tricuspid annulus (since this boundary is very small compared to the bounding surface). Given a fixed image and mesh resolutions in this neighborhood, whenever there are structures very close to the centroids, they tend to end up having distorted triangulation with self intersections. This problem however can be solved by increasing the resolution of meshes $M$ radially towards the centroid of the mitral or tricuspid annulus.

Another limitation is the manual landmark placement and the strategy of fixing the orientation in the proposed representation. From the experiments, one can see that the inaccuracy in landmark placement in the LV can lead to an angular error everywhere when different geometries are mapped onto our representation, while the errors are more localized in RV due to fixing the landmarks on our representation. We decided not to fix the two LV boundary landmarks on our representation to reduce possible distortion due to a more constrained mapping, however if these landmarks were fixed, just as in the case of RV, the inaccuracies in landmark placement would lead to much more localized errors. Furthermore, it is possible to automate the landmark placement using methods proposed by Karavides et al. (2010), Zheng et al. (2009a), Lu et al. (2009), Zheng et al. (2009b) or Lu et al. (2009).

The time and the accuracy of our algorithm depends on the element size of the discretized domain. The average total processing time of our algorithm executed on our 12 detailed anatomy meshes was $9\ min\ 10\ s$ on a single processor for the image size of $195 \times 228 \times 301$ voxels (isotropic voxel size of $0.3\ mm$) and $3000$ iterations. The average reconstruction error was on the level of $1\ \mu m$.

## 4.7 Conclusion

In this paper we presented a framework for mapping the meshes of right and left ventricular detailed cardiac anatomy to a common subject independent reference frame. The proposed method represents a major step towards the statistical analysis and quantification of different detailed ventricular morphologies among patients in a common framework with the potential application in computational cardiac models.

The framework allows mapping trabeculations from one heart geometry to another geometry given by a smooth surface. Thus, it is providing us the means of including different extracted trabecular morphologies to already available cardiac computational models, where the endocardial surfaces are modeled as smooth surfaces.

# Chapter 5

# QUANTIFICATION OF THE DETAILED CARDIAC VENTRICULAR TRABECULAR MORPHOGENESIS IN THE MOUSE EMBRYO

The content of this chapter is adapted from the following publication: **Paun B**, Bijnens B, Cook AC, Mohun TJ, Butakoff C, *Quantification of the Detailed Cardiac Ventricular Morphogenesis in the Mouse Embryo*, to be submitted, 2017.

## Abstract

During embryogenesis, a mammalian heart develops from a simple tubular shape into a complex 4-chamber organ, going through four distinct phases: early primitive tubular heart, emergence of trabeculations, tra-

becular remodeling and development of the compact myocardium. In this chapter we propose a framework for regional cardiac ventricular myocardial complexity analysis in 3D, consisting of a standardized, individual-independent, representation, and a novel physiologically meaningful complexity measure. The representation is based on a standardized subdivision of the myocardium into 3D blocks, similar to the 17 (American Heart Association) segments, whereupon different measures of structural complexity can be calculated and summarized across a population. This framework allows to extract different complexity measures, commonly applied to 2D image slices, in 3D and use 3D specific measures. In particular, we extend the standard fractal dimension (FD) to 3D and propose to describe the myocardial complexity by the volume occupied by the trabeculations in each region, and their surface area. This measure provides an intuitive characterization of the complexity, given that compact myocardium will tend to occupy a larger volume with little surface area while high surface area is directly related to the amount of endocardium in contact with the blood.

Using mouse embryo images at different gestational stages, we demonstrate how the proposed representation and complexity measure describes the evolution of myocardial complexity and compare our results to the previously used Fractal Dimension (FD). The mouse embryo data was acquired using high resolution episcopic microscopy (HREM). The complexity analysis per region was carried out using: 3D FD, myocardial volume, myocardial surface area and ratio between the two. The analysis of gestational ages was performed on embryos of 14.5, 15.5, 16.5, 17.5 and 18.5 embryonic days and demonstrated that the regional complexity of the trabeculations increases longitudinally from the base to the apex, with a maximum around the middle. The overall complexity decreases with gestational age, being most complex at 14.5. Radially, at stages 14.5, 15.5 and 16.5, the trabeculations show similar complexity everywhere except for the anteroseptal and inferolateral area of the wall, where it is smaller. At 17.5 days, the regions of high complexity become more localized towards the inferoseptal and anterolateral parts of the wall. At the 18.5 days, the high complexity area exhibits further localization at the

inferoseptal and anterior part of the wall.

## 5.1 Introduction

The development of the myocardium appears to be similar in many vertebrates. In particular, before the intramural cardiac vessels appear, the ventricular walls consist mainly of trabeculations. Those early trabeculations increase myocardial surface area and serve to increase myocardial oxygenation and nutrient delivery by diffusion, while sufficient tissue volume builds up for myocardium development at the later stages. However, the compaction does not lead to a disappearance of the trabeculations. A number of animal studies suggest that smooth ventricles lead to severe heart failure and elevated embryonic lethality (Captur et al., 2015). On the other hand, it was observed that excessive trabeculations can lead to heart failure, atrial and ventricular arrhythmias and thromboembolic events (stroke) (Ritter et al., 1997; Oechslin et al., 2000; Kovacevic-Preradovic et al., 2008; Penela et al., 2013; Oechslin and Jenni, 2011). Trabeculated myocardium can be seen in normal hearts and can be frequently seen at younger ages, diminishing with age, with some gender differences (Dawson et al., 2011). A high proportion of young athletes, especially of African/Afro-Caribbean origin, also exhibit an increased amount of trabeculations.

One of the animal models to investigate the developing heart and related pathologies is the mouse embryo, where genetic alteration have been found to affect normal cardiac development, leading to either decreased or increased trabeculation. The trabeculae first appear at about 9.0 - 9.5 days in the embryo, at the end of cardiac looping. By E14.5 ventricular septation is complete and a dense trabecular meshwork is established. At this moment, proliferation of the trabeculations stops and intertrabecular spaces seem to transform into the vessels (Captur et al., 2016). At the same time, papillary muscles, the moderator band, and effective arterial valves are starting to form.

Recently, a quantification of myocardial complexity of mice embryos

was presented (Captur et al., 2016). The authors proposed to use fractal dimension (FD), measured on the myocardial contours in 2D short axis and 2-chamber MRI image stacks. The authors demonstrated that trabecular profiles increase from base towards the mid/apical region and decrease towards the apex. They also demonstrated that during later development, from the establishment of the interventricular septum (IVS) at E14.5 to E18.5, trabecular complexity reduces and its decline is not proportional to the increase in compact wall volume. Even though the 2D FD measurement correlates with the visual perception of complexity, it has several drawbacks when applied to non-linear fractal structures such as natural fractals. The first and the largest problem in FD calculation is a lack of consensus with respect to the choice of its parameters. For example, in the typically used box counting, one has to decide on the minimum and maximum block size, the step for the block shift, how to perform the block shifts as well as how many to do, and finally, how to fit a line to the box counts (Foroutan-Pour et al., 1999; Jelinek et al., 2006; Karperien and Jelinek, 2016). Any variation in these parameters can significantly affect the FD. Another problem with 2D FD for analysis of myocardium is that the calculated values do not represent the 3D structure, and 2D slice-by-slice analysis inherently restricts the applicability of a larger range of methods.

In this chapter, we propose a framework for 3D myocardial assessment and a novel 3D measure of complexity. We use the proposed methodology to study the evolution of cardiac trabeculations in the left ventricle of mouse embryos across different gestational stages. The proposed framework uses the recently introduced myocardium reparameterization (Paun et al., 2017), where an individual shape-independent method for establishing point-to-point correspondence between the cardiac ventricles is proposed. Consequently, that method provides a way of subdividing the ventricles into 3D regions in a standardized way for inter-individual comparison of structural and shape properties as well as studying temporal evolution. The myocardial complexity can then be estimated on a per region basis with regions of any desired size.

To asses the myocardial complexity in each region, we propose to use

a moving window (encompassing the neighboring regions), calculating the volume of the myocardium within the window and the area of the myocardial surface in contact with the blood. The surface area is expected to increase with the amount of blood cavities within the myocardium, while the volume increases with the amount of tissue filling the region. Therefore, highly trabeculated areas will have high area and low volume measures, while compact tissue will have low area and high volume. In our experiments, we demonstrate that the regional ratio of myocardial surface area to volume increases with myocardial complexity.

The evolution of the myocardial complexity was studied in a set of mouse embryos, acquired at different gestational stages: from 14.5 days, when the ventricular septation is complete and a dense trabecular meshwork is established within the ventricular cavities, through 15.5, 16.5, 17.5, to 18.5 days, when the compact myocardium matures. We subdivided the myocardium into 361 regions (8 slices longitudinally and 40 circumferentially plus apex). In each of these regions we calculated the 3D fractal dimension, myocardial volume, myocardial surface area, and surface to volume ratio. We show how these measures represent the myocardial complexity for each gestational stage and how do they evolve from one stage to another, emphasizing the differences. Finally we discuss the advantages and disadvantages of each of the measures.

## 5.2 Data

All specimens were handled in compliance with the Guide for the Care and Use of Laboratory Animals published by the US National Institutes of Health and with the approval of the MRC National Institute of Medical Research Ethical Review Panel. Mouse (*Mus musculus*) embryos were obtained from NIMR:Parkes (a robust outbred strain maintained at the MRC National Institute of Medical Research). For approximate embryo staging, detection of a vaginal plug was taken as gestation day 0.5 (E0.5).

In order to minimize retention of blood in embryo hearts, harvested embryos were first agitated in phosphate buffered saline (PBS) solution

at $37\ ^{\circ}C$ containing heparin for approximately $15$ minutes (min), umbilical vessels being repeatedly clipped to allow blood to be pumped out. Potassium chloride was then added (final $50\ mM$) to ensure that hearts arrested in diastole. Hearts (including attached lungs and thymus) were then isolated, washed briefly in fresh PBS and after removal of at least one lung lobe, samples were fixed for $30\ min$ in fresh $4\ \%$ paraformaldehyde at $4\ ^{\circ}C$. To remove remaining blood within the heart chambers, samples were then washed in repeated changes of distilled water over $30 - 60\ min$ at room temperature with constant agitation (roller). The resulting osmotic shock lysed any remaining blood within the heart chambers without any alteration to heart structure as assessed by histology. After overnight fixation in $4\ \%$ paraformaldehyde ($4\ ^{\circ}C$), hearts were dissected away from associated lung, thymus and pericardial tissue prior to dehydration and embedding in methacrylate resin (Mohun and Weninger, 2012). Samples were positioned during embedding to ensure relatively reproducible base-to-apex sectioning during the HREM imaging process.

Prepared samples were then used for the high resolution episcopic microscopy (HREM) analysis as described in Weninger et al. (2006). Briefly, HREM uses block-face imaging to produce perfectly registered digital image stacks capturing the 3D architecture of the embryonic heart at high resolution. Resulting datasets comprise 1000-2000 digital, short-axis images, produced by repeated removal of $2\ \mu m$ (E14.5 - E16.5) or $3\ \mu m$ (E17.5, E18.5) sections (base-to-apex direction).

## 5.3 Methods

### 5.3.1 Overview

In Fig. 5.2, we depict an overview of the proposed framework. The input HREM datasets are first preprocessed, aligning them to have approximately the same orientation, and to segment the LV myocardium. We manually removed the valves and the tendinous chords, and from the cleaned segmentation, extracted the interface between the blood pool and the tissue. The cleaned segmentation and the interface images are then

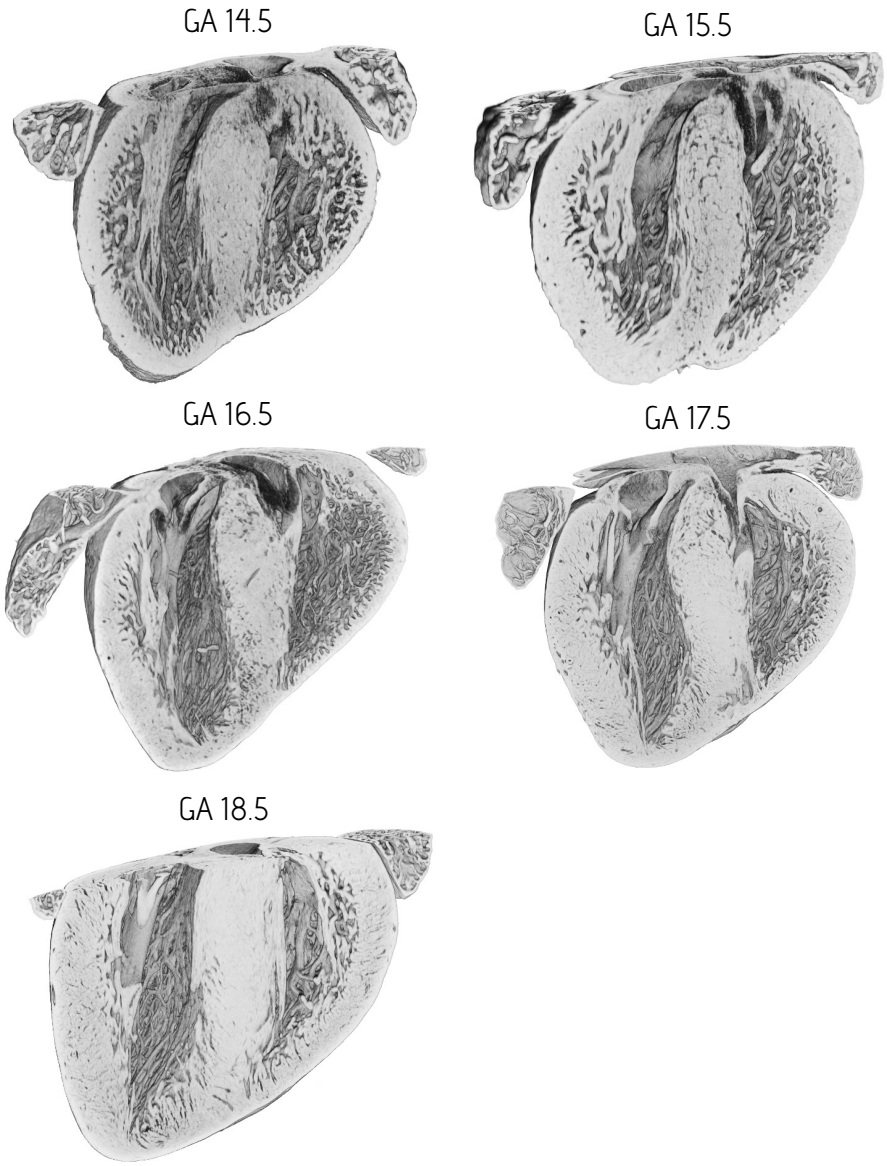


Figure 5.1: Volumetric visualization of the datasets for each GA.

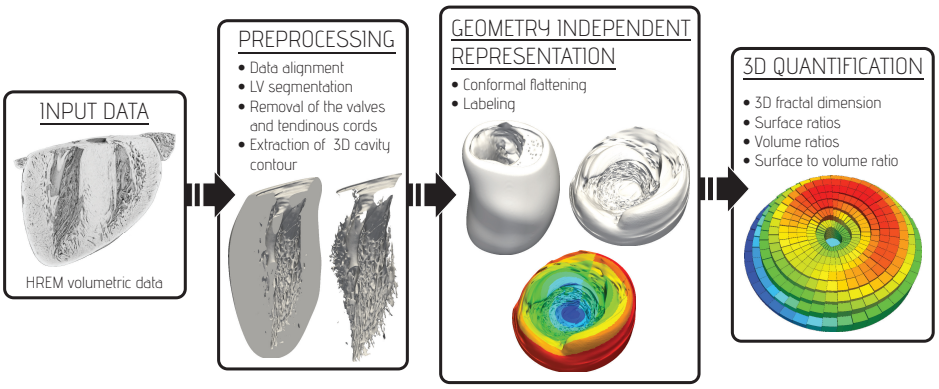


Figure 5.2: Pipeline for 3D quantification of myocardial complexity. The colors of the flattened mesh under geometry independent representation represent the labels of 361 segments. The colors of the figure under 3D quantification step represent myocardial volume values for each of 361 segments.

mapped to the standardized representation and subdivided into regions.

The tissue complexity analysis was performed on 50 subjects, 10 subjects per GA, ranging from 14.5 to 18.5 embryonic days. For each GA, mean and standard deviation of the segment complexity values were calculated and plotted on continuous bulls-eye plots. Two metrics were used:

- *Fractal dimension*, performed on the interface between the trabeculations and the blood pool.
- *Regional myocardial volume and surface area*, performed on the myocardial image masks.

To produce the plots of complexity, the analysis was performed on the neighborhood of each segment by employing a $5 \times 5$ moving window (Fig. 5.3). The values on the boundaries were calculated by zero padding. The neighborhood of the apical segment was defined as the apex and the adjacent apical ring segments.

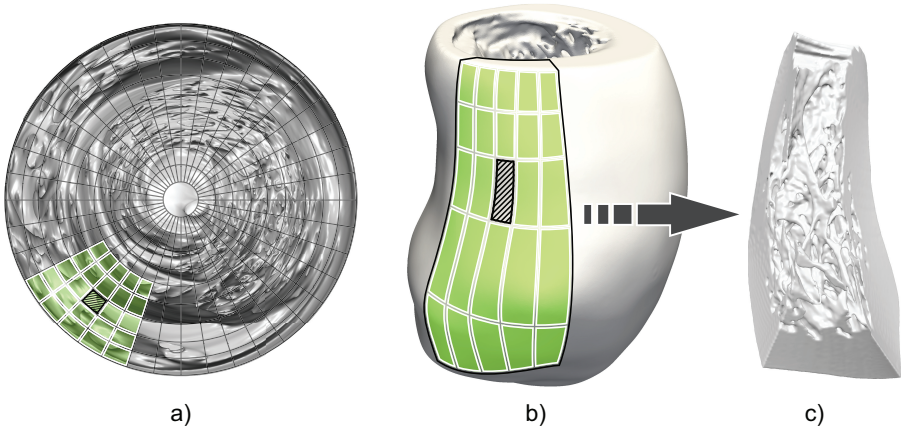


Figure 5.3: Visualization of one of the dataset's segments and its neighborhood used in the analysis. a) *Flattened* dataset divided into 361 segments. The black shaded element represents the segment for which we calculate the corresponding metrics, while the green elements represent its $5 \times 5$ neighborhood region used in calculations. b) The same element and its neighborhood region displayed on the original non-*flattened* dataset. c) Extracted segment and its $5 \times 5$ neighborhood region viewed from the inside of the cavity.

### 5.3.2 Data Preprocessing

The proposed framework for 3D assessment of myocardial complexity takes as an input aligned volumetric image segmentations of LV myocardium with all its detailed anatomy present within the blood pool (excluding valve and tendinous chords). The alignment was corrected by matching the heart's LAX (defined by the centroid of the mitral annulus and the LV apex) with the positive z direction of the image.

Subsequently, the whole hearts were segmented using the Seg3D image processing software (CIBC, 2015) following the procedure described in (Paun et al., 2017). The obtained segmentations are then clipped at the level of Mitral valve annulus to remove the atria and great vessels.

From those images, we extracted the LV blood pool mask and manually delineated and extracted the LV epicardial mask. The mitral valve and tendinous cords are manually delineated and removed from the blood pool masks. The myocardial mask, with all the detailed anatomy, is obtained as the difference of the epicardial and the cleaned blood pool mask. These are used to subdivide the myocardium into regions.

The proposed 3D fractal analysis is performed on a single voxel thick 3D contour, representing the interface between the myocardium and the blood pool, obtained using the binary contour filter (ITK (Yoo et al., 2002)) on the cleaned blood pool mask.

### 5.3.3 Geometry Independent Representation of a Ventricle

The method of Paun et al. (2017) allows establishing correspondence between different objects having an overall shape of a thick hemispherical shell. To do so, apart from the object itself (represented by either a surface or volumetric mesh), we also require an enclosing surface (represented by a triangulated mesh), that contains the whole object in its interior. The mapping is then calculated in 2 steps. First, we map the enclosing surface to a suitable planar domain. To impose a consistent orientation, we specify 3 landmarks on the enclosing surface and perform the conformal or quasi-conformal flattening to the planar domain. Secondly, we map our object to the volumetric domain defined by the planar domain (usually a cylinder or a prism). The planar domain is transformed as explained in Chapter 4, Subsection 4.3.3, to compensate for increasing triangle density towards the disk's center. In this volumetric domain, we subdivide the base (the disk) into 361 segments by introducing 8 rings of equal thickness (corresponding to the apex-to-base slices in the LV), each split equally into 40 circumferential (septal-lateral-septal) segments. The apical segment is not subdivided. The subdivision can be seen in Fig. 5.3.

### 5.3.4 Fractal Analysis

The 3D fractal analysis presented in this study was performed using an in-house implementation of the cube-counting method (3D equivalent of the box-counting method) similarly to Goñi et al. (2013), where the estimated fractal measures were obtained by the box counting method of Russell et al. (1980), suitable for objects with and without self-similarity.

The cube(box) counting method is performed by superimposing the 3D image of the object under study with isotropic grids made of regular cubes of size $\epsilon$. In the image, the object is represented by nonzero voxel values (with zero being the background).

We first find the smallest region enclosing the object (its bounding box) and randomly select the grid origin from all possible voxel locations within the region. For each grid of cube size $\epsilon$, the number of cubes necessary to fully cover the object, $N(\epsilon)$, is recorded. Let $N_i(\epsilon)$ represent the number of non-zero voxels contained in the $i$-th non-empty cube of size $\epsilon$, where $i \in [1, N(\epsilon)]$. The total number of non-zero voxels (voxels of the object) can be obtained from:

$$N_{all} = \sum_{i=1}^{N(\epsilon)} N_i(\epsilon), \tag{5.1}$$

and the probability of finding a non-zero voxel (voxel of the object) within the $i$-th non-empty cube of size $\epsilon$ is equal to:

$$p_i = \frac{N_i(\epsilon)}{N_{all}}. \tag{5.2}$$

Those measurements were then used to calculate the generalized dimension spectrum (Hentschel and Procaccia, 1983), where generalized (Rènyi) dimensions $D_q$ of order $q$ are defined by:

$$D_q = \lim_{\epsilon \to 0} \frac{1}{1-q} \frac{\log \sum_{i=1}^{N(\epsilon)} p_i^q}{\log \frac{1}{\epsilon}}, q = 0, 1, 2, \ldots \tag{5.3}$$

where $D_q$ is a non-increasing function of $q$,

$$D_{q_1} \geq D_{q_2} \quad if \quad q_1 < q_2. \tag{5.4}$$

$D_q$ for $q > 0$ will tend to be more accurate, as the higher order correlations are taken into account as $q$ increases. As can be seen from equation 5.3, for $q = 0$, the $D_0$ dimension does not distinguish boxes with high density of voxels from those containing just a single voxel. More precise dimension measurements can be obtained from $D_1$ and $D_2$, which take into account inhomogeneities or correlations of elements of the object.

We calculated the generalized dimensions for $q = 0, 1$ and $2$ which corresponds to the box counting dimension ($D_0$), the information dimension ($D_1$) and the correlation dimension ($D_2$) respectively, where:

$$D_0 = \lim_{\epsilon \to 0} \frac{\log N(\epsilon)}{\log \frac{1}{\epsilon}} \tag{5.5}$$

$$D_1 = \lim_{\epsilon \to 0} \frac{\sum_{i=1}^{N(\epsilon)} p_i \log p_i}{\log \epsilon} \tag{5.6}$$

$$D_2 = \lim_{\epsilon \to 0} \frac{\log \sum_{i=1}^{N(\epsilon)} p_i^2}{\log \epsilon} \tag{5.7}$$

As the limit $lim_{\epsilon \to 0}$ is not feasible in practical applications, $N(\epsilon)$ and $N_i(\epsilon)$ are measured for a certain range of $\epsilon$ values (Hentschel and Procaccia, 1983).

In our implementation, the grid cube size $\epsilon$ was linearly increasing by 1 voxel. The number of non-empty cubes decreases exponentially with the increase of the grid resolution $\epsilon$, where the exponent represents the corresponding fractal dimension depending on the order of correlations between image voxels taken into account. $D_0$ is estimated from the slope obtained by linear regression from the log-log plot of $\log N(\epsilon)$ versus $\log 1/\epsilon$. Similarly, $D_1$ and $D_2$ are obtained from the log-log plots of $\sum_{i=1}^{N(\epsilon)} p_i \log p_i$ versus $\log \epsilon$ and $\log \sum_{i=1}^{N(\epsilon)} p_i^2$ respectively.

Due to inter-object difference in geometry, grids of cube size $\epsilon$ do not represent the same spatial resolution between objects (Goñi et al., 2013). Moreover, it is known that using grids of too small and too big

cube sizes will lead to erroneous fractal dimension estimates (Foroutan-Pour et al., 1999). To take into account the varying geometry size and possible variation in image resolution, the range of $\epsilon$ values was taken from $2\ \%$ to $25\ \%$ of the smallest dimension of the object bounding-box. An example of the calculations can be seen in Fig. 5.4, 3rd column.

In all our experiments, the values of $D_0$, $D_1$, and $D_2$ were similar, however the values corresponding to lower $q$ tended to be noisier and sometimes underestimating the real complexity. Since the higher $q$ tends to be more accurate, in all the following sections, as a fractal dimension (FD), we report only the value of $D_2$.

### 5.3.5 Volume and Surface Area Calculations

Another type of complexity analysis is performed by utilizing volume and surface area measures of the object segments and their ratios. Given the regions defined on each dataset, we calculate the volume, occupied by the cardiac tissue for each region of the object, and the volume of the region itself. The ratio of these two volumes provides a percentage of how much volume does the cardiac tissue occupy within the region. This ratio increases with the increase of wall thickness and compactness of the myocardium.

In a similar way, we calculate the surface areas of the cardiac tissue and the enclosing segment. Surface areas are calculated from triangular surface meshes obtained form the corresponding volumetric images. The ratio of cardiac tissue surface area and segment surface area increases as the myocardial surface becomes more complex and convoluted within the segment. Examples of the calculations can be seen in Fig. 5.4, 4th and 5th columns.

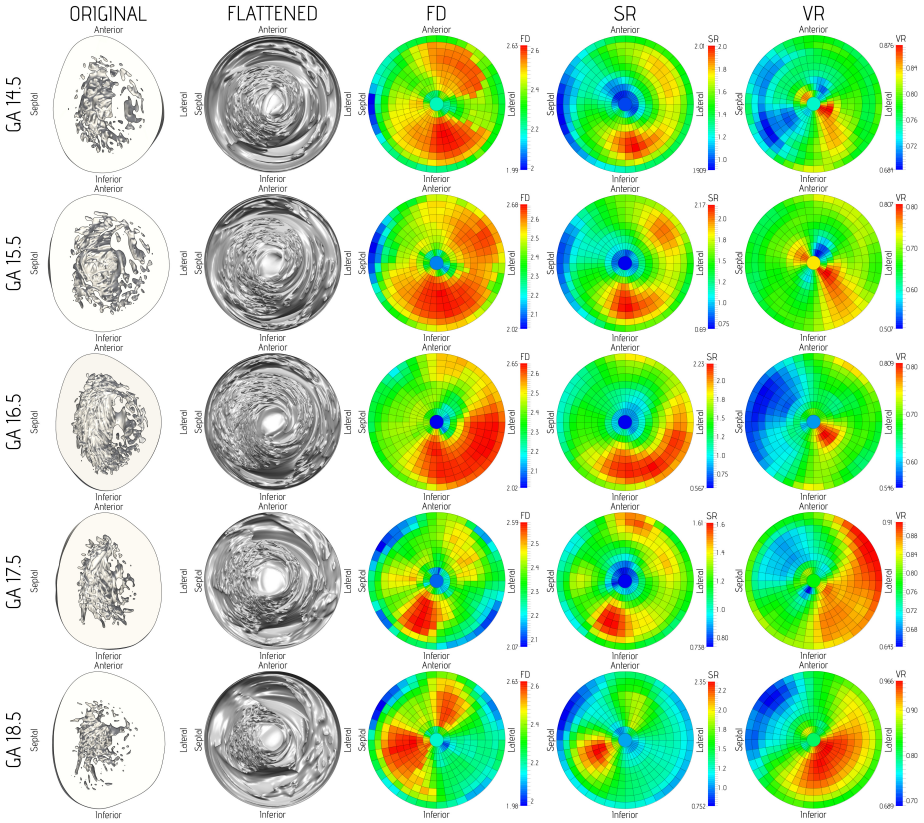


Figure 5.4: Sample datasets from each gestational stage with the *flattening*, FD ($D_2$), surface ratio (SR) and volume ratio (VR). The datasets were clipped at the middle to give a better view at the interior of the chamber.

## 5.4 Results

### 5.4.1 Complexity Analysis Using Regional Fractal Measures

The mean and standard deviation of the regional FD was calculated for each GA. In the cube-counting method, we used 50 grid offsets and the

size of the grid boxes was ranging from $2\ \%$ to $25\ \%$ of the segment's bounding box. The increment of the grid cube size was 1 voxel. Fig. 5.5 shows the mean regional correlation dimensions ($D_2$) and their corresponding coefficients of variation per GA, expressed as the percentage of the mean.

From Fig. 5.5, 2nd column, we can see that myocardial complexity globally increases as we move from the base towards mid/apical part of the heart and then decreases towards the apex. That is especially pronounced at stages E14.5, E15.5 and E16.5, where all mid and apical parts (except the anteroseptal, lateral and inferolateral wall) have similar trabecular complexity. The radial extent of the lower complexity regions increases from E14.5 to E16.5, while the lateral high complexity region, present at E14.5, gradually shifts towards the inferolateral part of the wall. By E17.5, the higher complexity is present in the mid and apical parts of the septal, inferior, and inferoseptal wall and the basal and mid parts of the anterior and anterolateral wall. The overall complexity globally decreases, which could be related to the compaction and volume increase of the compacted myocardium (Fig. 5.5, 3rd row, 1st column). At E18.5, the most complex regions are narrowed to the mid and apical parts of the anterior, septal, inferior and inferoseptal wall. The regions of low complexity in the first and second basal ring, throughout all the GAs, are due to a smoother wall close to the outflow tract and the manually removed valve. As expected, myocardial complexity decreases with gestational age, which coincide with the visual inspection of the 3D data visualizations and is in agreement with results obtained by Captur et al. (2016).

The values of the coefficient of variation are more or less similar between the cases, while the areas of high variability are present in the apex of E14.5 and apical, anterolateral regions of E18.5.

Fig. 5.6 depicts plots of mean FD per GA. Nine different graphs in each plot represent FD values as we move circularly counterclockwise from the lateral wall towards the septum and back to the lateral wall. Each line represent a different radial location (ring) in the bull's eye plot, or longitudinal location in the apex-base direction. There are 10 graphs, with the apex being a straight black line, and 9 graphs representing 9

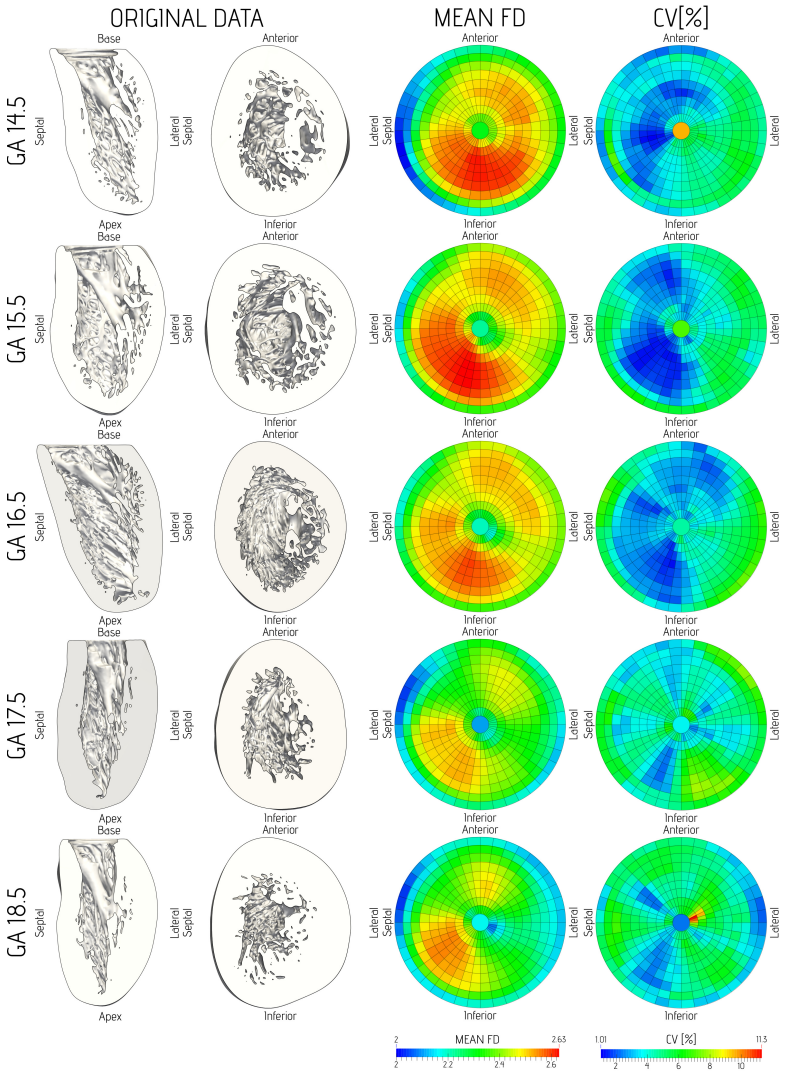


Figure 5.5: Continuous bull’s eye plots representing the average regional fractal dimension ($D_2$) per GA (2nd column) and the coefficient of variation of the regional fractal dimensions per GA (3rd column). The first column shows a sample dataset for each GA sliced at the middle.

rings from the 1st apical ring (dark blue) to the 9th basal ring (dark red). The gray bands represent the $95\ \%$ average confidence intervals over the population.

### 5.4.2 Complexity Analysis Using Regional Occupied Volume and Surface Area

The overall occupied volume increases with gestational age, mainly due to myocardial wall thickening, which can be seen from Fig. 5.7 in the 2nd column, representing the mean regional occupied volume. At 14.5 GA, the occupied volume is the highest in the apex, the basal, mid and apical parts of the inferior and inferolateral wall, the apical and mid parts of the lateral, anterolateral and anterior wall. At 15.5 GA, it increases everywhere, having the highest values at the mid and apical parts of the inferoseptal wall. By 16.5 GA we see a significant decrease in the apex, the basal and mid anterior, anteroseptal and septal wall. A further overall increase can be seen by 17.5, with highest values in the basal, mid and apical parts of the inferior, inferolateral and lateral wall and the basal parts of the anterolateral wall. At 18.5 GA, the overall occupied volume still increases, with the most pronounced increase in the basal, mid and apical parts of the inferior, inferolateral, lateral and anterolateral wall.

Fig. 5.7, 3rd column, represents the coefficient of variation of the regional occupied volumes within the population, expressed as the percentage of the mean. At 14.5 GA, the occupied volume between subjects varies the most in the apex, the apical regions of the inferior and anterolateral wall and the basal parts of inferoseptal wall. By 15.5 GA, the variation increases in the apical and mid parts of the anterior, anterolateral and lateral wall. In 16.5 GA we observe an overall increase, where regions with the highest variability are located at the apex, the apical and mid parts of the anterolateral, lateral, inferior and inferoseptal wall, and the base and mid parts of the inferoseptal, septal and anteroseptal wall. At 17.5, we observe an overall decrease with regions of low variability at the apical, mid and basal parts of the inferolateral wall. At 18.5, a significant decrease of variation is observed in the whole inferior, inferolateral

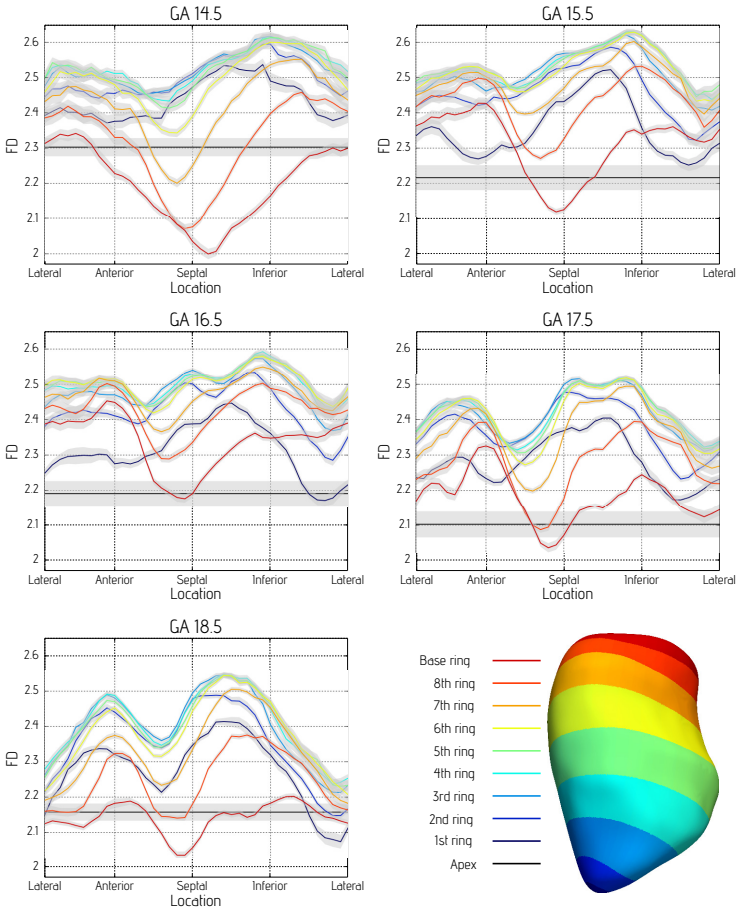


Figure 5.6: Plots of mean FD ($D_2$) per GA. Data is grouped into 9 longitudinal segments (apex-base). The X axis represents FD values of the circular regions in the order: lateral - anterior - septal - inferior - lateral wall. The gray bands represent $95\ \%$ average confidence intervals over the population.

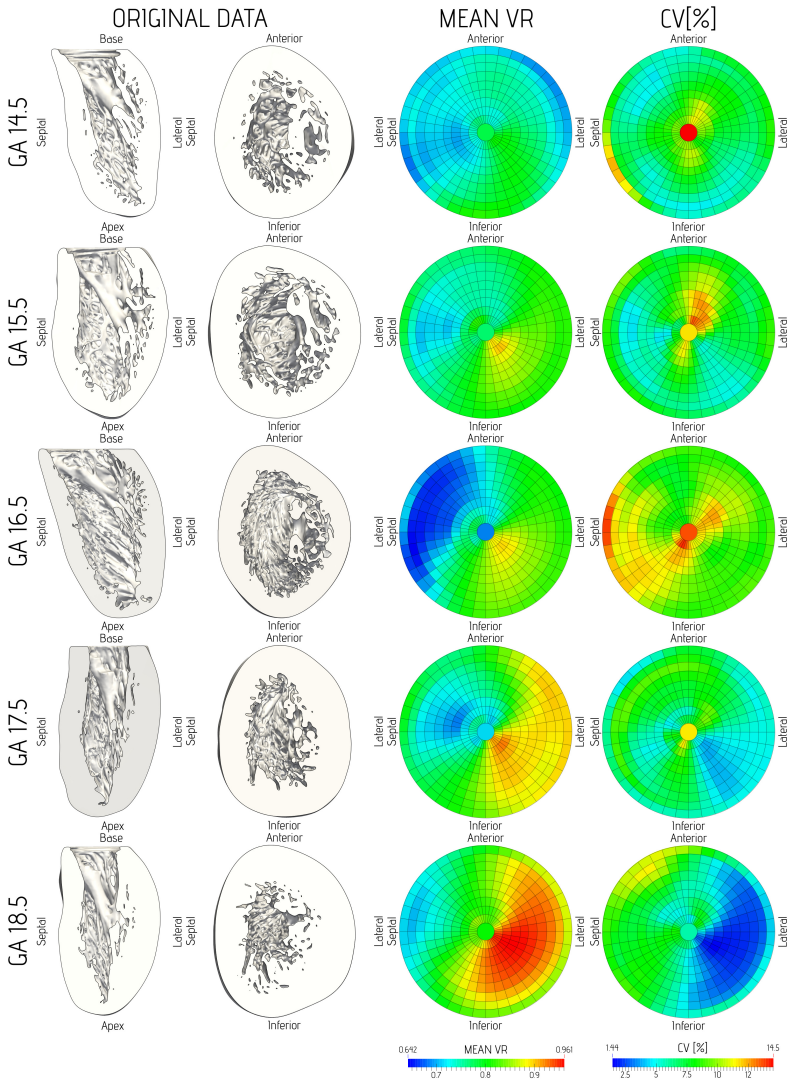


Figure 5.7: Continuous bull’s-eye plots of average regional occupied volume per GA (2nd column) and coefficient of variation of regional occupied volumes per GA (3rd column).

and lateral wall and the mid and basal part of the anterolateral wall. The regions of high variability in the basal parts throughout the GAs represent a segmentation artifact of the manual valve removal.

In Fig. 5.8, we show the mean and coefficient of variation of the regional surface area ratios. Higher values mean that the surface is more convoluted within the segment. At 14.5 GA, the highest mean regional surface area ratios are present at the mid and apical parts of the inferior and inferolateral wall and the mid part of the lateral and anterolateral wall. At 15.5 GA, it also increases in the mid part of the anterior, septal, inferoseptal wall, while it decreases in the apex, the apical and mid parts of the inferior and inferolateral wall and the mid part of the lateral wall. At 16.5 and 17.5 GA, we observe a further overall decrease, with the highest decrease in the apex and apical parts of the whole wall. Overall low surface ratio values, uniformly distributed over whole wall, are the results of myocardial compaction with a less convoluted surface of the tissue. By 18.5 GA, the value increases at the apex and is the highest at the apical and mid parts of the septal, inferoseptal and inferior wall, and the apical and mid parts of anterior wall.

The coefficient of variation of the regional surface area ratios at 14.5 GA has uniformly low values everywhere. At 15.5 GA, it increases at the apical, mid and basal parts of the inferoseptal, anterolateral and anterior wall and at the apical and mid parts of septal and anteroseptal wall. By 16.5 GA, the variation in surface area ratios concentrates at the apex, the basal and mid parts of the inferolateral, lateral and anterolateral wall, the apical, mid and basal parts of the septal wall and the basal parts of the anteroseptal wall. At 17.5 GA, there is a propeller-like pattern, where the higher values are located in the mid and apical parts of the inferoseptal, lateral and anteroseptal wall. The peak values are located at the apical and mid part of the anteroseptal and lateral wall. Finally, at 18.5 GA, the pattern of moderate values is located at the apical and mid parts of the septal wall, the basal parts of anteroseptal wall and the apical and mid parts of the anterior and anterolateral wall.

Fig. 5.9 shows a scatter plot of the myocardial volume versus surface area (not normalized by the segment volume and area) for all 361 seg-

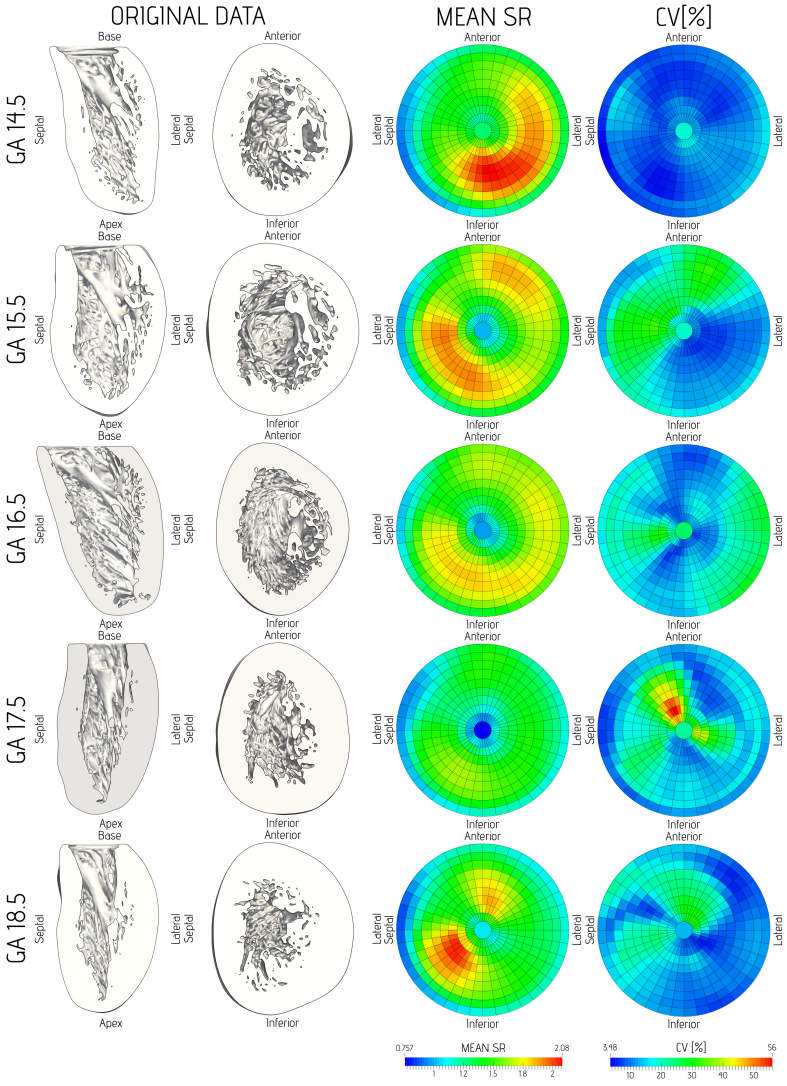


Figure 5.8: Continuous bull’s-eye plots representing average regional surface area ratios per GA (2nd column) and coefficient of variation of regional surface area ratios per GA (3rd column).

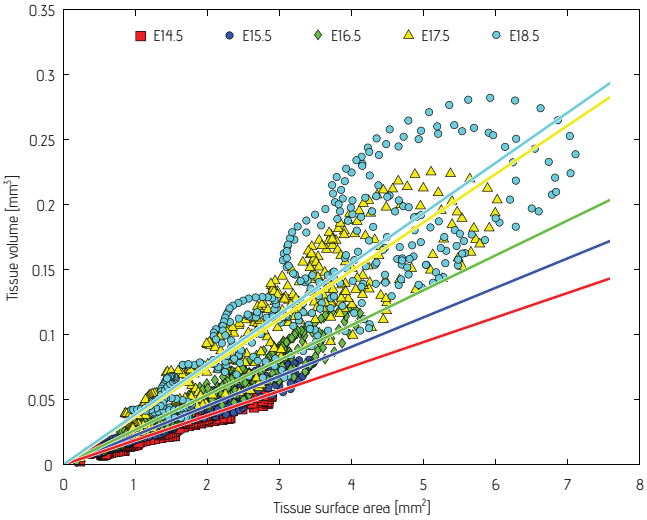


Figure 5.9: Regional volume versus surface area per GA.

ments of the 5 GAs. For each GA, we fit a line passing through the origin. We can observe that the slope of the line increases with gestational age, correlating with the apparent compaction and decrease in complexity with GA. Thus, if we look at surface to volume ratio, myocardial complexity is the highest at 14.5 GA and decreases towards 18.5 GA. The highest increase in the slope of 17.5 GA with respect to 16.5 GA could be explained due to myocardial compaction and likely nonlinear progression of complexity evolution, which we can observe in the bull’s eye plots. In particular, we can see that at 17.5 GA, the overall occupied volume increased, while the overall surface area decreased considerably, thus leading to a higher jump in the slope of the 17.5 GA regression line.

Similarly, Fig. 5.10 shows a scatter plot of the myocardial volume versus surface area for all 361 segments of the 5 GAs, normalized by the volume of the segment. Linear regression lines are obtained in the same way as for Fig. 5.9. We can observe the same trend in the regression lines as the GA increases, meaning that myocardial complexity decreases

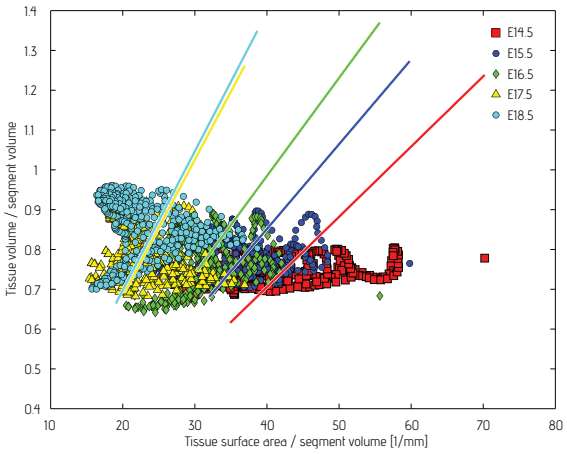


Figure 5.10: Regional volume versus surface area per GA, each normalized by segment volume.

with the increase of volume to surface ratio and increase of gestational age. FD values decrease with gestational age as well, while volume to surface ratio increases, as a result of the increasing occupied volume and decreasing surface area. From a visual inspection of the scatter plots, it is interesting to note that at the early GAs, the myocardium tends to occupy little volume with a high range of surface areas, which implies that there are many thin trabeculations. As the embryo grows, the surface area starts to decrease and the volume increase, which suggests that the trabeculations thicken or merge together.

Similarly, Fig. 5.11 represents a scatter plot of FD versus the myocardial volume surface area ratio for all 361 segments of the 5 GAs. The black line represent the regression line with correlation coefficient equal to $-0.5237$. The lower and upper bounds for a $95\ \%$ confidence interval for the coefficient are $[-0.5564, -0.4894]$.

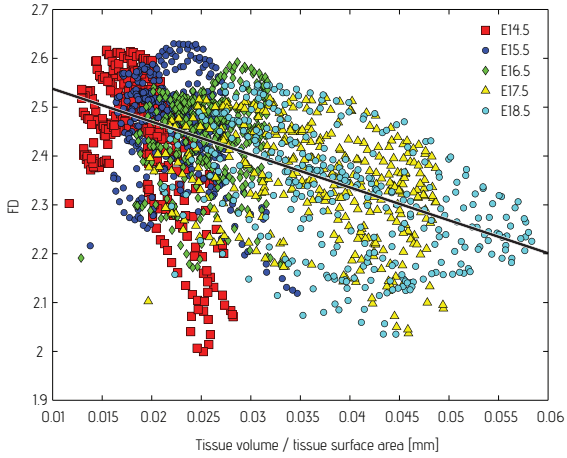


Figure 5.11: Regional FD versus volume-surface ratio per GA.

## 5.5 Conclusions

In this chapter, we presented a framework for regional cardiac ventricular myocardial complexity analysis and visualization using a standardized representation of the LV to ensure inter-individual as well as longitudinal comparison. We also extended the current state of the art method for FD-based evaluation of trabecular complexity analysis to 3D, where we perform the 3D fractal analysis locally on LV segments. The fractal analysis was extended with new proposed complexity measures such as surface ratios, occupied volume and surface-volume ratios. The obtained results are in agreement with the results obtained by Captur et al. (2016), where we get comparable results in trabecular complexity trends within the same gestational ages.

However, the *Captur et al.* method, performs 2D per-slice analysis and we have found no other reported results on regional trabecular complexity, defined either by the 17 AHA segments or any other variant. Therefore, to the best of our knowledge, this is the first study to perform a 3D regional myocardial complexity analysis, both spatially and longitu-

dinally. Our results confirm the known decrease in trabecular complexity with GA in normal (mouse) embryos, where the most complex regions at 18.5 embryonic day coincide with the regions where papillary muscles are established.

The proposed 3D fractal analysis, as compared to the 2D, allows for a more accurate quantification of the 3D myocardial wall and the proposed analysis framework allows to apply previously inaccessible methods of quantification. The 3D FD still inherits some of the drawbacks of the 2D approach. When applied to natural fractals, FD calculation has a lack of consensus with respect to the choice of parameters, which most of the times are chosen using visual inspection and based on a trial and error basis and the computational cost. The proposed area and volume measures provide a more clearly defined and more interpretable complexity measure: the increase in myocardial volume is related to the compaction or density increase, while surface area is simply the area of the interface between the blood and the tissue, directly proportional to the apparent complexity. The proposed approach allows for the quantification and comparison of normal, as well as abnormal, trabecular development and provides a way for the more objective quantification of alterations induced by genetic mutations.

# Chapter 6

# GENERAL CONCLUSIONS

During the realization of this thesis, I have investigated the relationship between the detailed cardiac ventricular anatomy and indices of global cardiac function, and developed a framework for statistical analysis and visualization of those structures.

In Chapter 2, a simplified model of LV trabeculations was constructed and utilized to show that a trabeculated ventricle can work at lower strains compared to a nontrabeculated one, to produce the same stroke volume. It is possible to find an optimal amount of trabeculations, where stroke volume is optimized while LV size remains within physiological ranges. The trabeculations can serve to aid the heart in increasing its stroke volume without increasing the strain. Simulation results demonstrate, from a geometrical point of view, why the trabeculations are necessary for a more efficient cardiac function, and that even a small amount of them can be beneficial. This can help in a better diagnosis of, e.g., patients with noncompaction cardiomyopathy as well as to understand why some dilated ventricles show hypertrabeculation while others do not.

In Chapter 3 and 4, I proposed two mapping methods which allow us to define a patient independent representation, where populational statistical analysis can be performed. The first method represents a fast, computationally inexpensive method for parametrization of ellipsoidal-like shapes such as the LV. Despite being fast, it is only applicable to

ellipsoidal-like shapes. As the calculation of the depth within the myocardium is performed along straight lines from the centroid of the mitral (tricuspid) annulus and the bounding surface, any strong deviation from ellipsoidal shape will result in parametrization errors. The second method is a generalization to any shell-like shape, including the RV, by calculating a non-divergent vector field inside the chamber, representing the flow from the bounding surface to the centroid of the mitral (tricuspid) annulus. This is achieved by solving the Laplace equation in the interior of the chamber. There is still one limitation, however. The use of a uniformly discretized domain for the solution of the Laplace equation and the high density of the streamlines in the vicinity of the centroid of the mitral or tricuspid annulus, might lead to a distorted triangulation with self intersections for any structures close to the centroids. A possible remedy for this problem could be a domain with adaptive element size, for instance with the resolution increasing radially towards the centroids, using octree or similar representations.

One of the advantages of the proposed parametrization is that they are not limited to the planar domain shapes we used in this thesis. The main reason for such domains was their widespread use by many authors for the visualization of any LV and RV information in the form of a bull's-eye plots. If necessary, the same methods can be used to represent the information on any convex planar domain, and, using the approach proposed by Sawhney and Crane (2017), can be extended to any shape. Moreover, the proposed methods allow mapping different kinds of information from one cardiac geometry to another, thus providing the means of including different extracted trabecular morphologies, myocardial fibers, Purkinje networks, scar patterns, to already available cardiac computational models.

Lastly, in Chapter 5, I have presented a framework for regional cardiac ventricular myocardial complexity analysis and visualization using a standardized representation of the LV to ensure inter-individual as well as longitudinal comparison. The current state of the art method for FD-based evaluation of trabecular complexity analysis was extended from 2D to 3D, where 3D fractal analysis was performed locally on LV segments.

Additionally, we proposed new complexity measures for cardiac ventricular myocardial complexity such as surface ratios, occupied volume and surface-volume ratios.

The 3D fractal analysis still inherits some of the drawbacks of the 2D approach, such as lack of consensus with respect to the choice of parameters, which are mostly chosen by visual inspection on a trial and error basis, trying to also optimize the computational cost. Therefore, we extend the myocardial complexity analysis with the proposed area and volume measures, which provide a more clearly defined and more interpretable complexity measure and do not have the drawbacks of the calculation of the fractal dimension.

Finally, the work carried out in Chapter 5, to the best of my knowledge, represents the first reported work on spatial and longitudinal analysis of the 3D regional myocardial complexity. The proposed framework allows for a 3D quantification and comparison of normal, as well as abnormal, trabecular development and provides a way for a more objective quantification of alterations induced by genetic mutations.

# Publications During the Thesis

## International Journals

1. **Paun B**, Bijnens B, Iles T, Iaizzo PA, Butakoff C, *Patient independent representation of the detailed cardiac ventricular anatomy*, Medical image analysis, 2017, 35:270-87. Impact factor: 4.565, quartile: Q1.

2. **Paun B**, Bijnens B, Butakoff C, *Relationship between the left ventricular size and the amount of trabeculations*, under review, 2017.

3. **Paun B**, Bijnens B, Cook AC, Mohun TJ, Butakoff C, *3D Quantification of the Detailed Cardiac Ventricular Anatomy Morphogenesis in the Mouse Embryo*, to be submitted, 2017.

4. Gonzalez-Tendero A, Zhang C, Balicevic V, Cárdenes R, Loncaric S, Butakoff C, **Paun B**, Bonnin A, Garcia-Cañadilla P, Muñoz-Moreno E, Gratacós E, Crispi F, Bijnens B, *Whole heart detailed and quantitative anatomy, myofibre structure and vasculature from X-ray phase-contrast synchrotron radiation-based micro computed tomography*, European Heart Journal - Cardiovascular Imaging, 2017. Impact factor: 4,293, quartile: Q1.

# International Conferences

1. **Paun B**, Bijnens B, Butakoff C, *Subject independent reference frame for the left ventricular detailed cardiac anatomy*, In Lecture Notes in Computer Science, 2015, Vol. 9126, pp. 240-247, Springer.

2. Balicevic V, Loncaric S, Cardenes R, Gonzalez-Tendero A, **Paun B**, Crispi F, Butakoff C, Bijnens , *Assessment of Myofiber Orientation in High Resolution Phase-Contrast CT Images*, In Lecture Notes in Computer Science, 2015, Vol. 9126, pp. 111-119, Springer.

# Bibliography

Agmon, Y., Connolly, H. M., Olson, L. J., Khandheria, B. K., and Seward, J. B. (1999). Noncompaction of the ventricular myocardium. *Journal of the American Society of Echocardiography*, 12(10):859–863.

Anderson, S. E., Hill, A. J., and Iaizzo, P. A. (2009). Microanatomy of human left ventricular coronary veins. *The Anatomical Record*, 292(1):23–28.

Anderson, S. E., Quill, J. L., and Iaizzo, P. A. (2008). Venous valves within left ventricular coronary veins. *Journal of Interventional Cardiac Electrophysiology*, 23(2):95–99.

Arbustini, E., Weidemann, F., and Hall, J. L. (2014). Left ventricular noncompaction: A distinct cardiomyopathy or a trait shared by different cardiac diseases? *Journal of the American College of Cardiology*, 64(17):1840–1850.

Ashikaga, H., Coppola, B. A., Yamazaki, K. G., Villarreal, F. J., Omens, J. H., and Covell, J. W. (2008). Changes in regional myocardial volume during the cardiac cycle: Implications for transmural blood flow and cardiac structure. *American Journal of Physiology-Heart and Circulatory Physiology*, 295(2):H610–H618.

Attene, M. and Falcidieno, B. (2006). ReMESH: An interactive environment to edit and repair triangle meshes. In *IEEE International Conference on Shape Modeling and Applications 2006 (SMI'06)*, pages 41–41.

Bernanke, D. H. and Velkey, J. M. (2002). Development of the coronary blood supply: Changing concepts and current ideas. *The Anatomical Record*, 269(4):198–208.

Bijnens, B., Cikes, M., Butakoff, C., Sitges, M., and Crispi, F. (2012). Myocardial motion and deformation: What does it tell us and how does it relate to function? *Fetal diagnosis and therapy*, 32(1-2):5–16.

Bishop, M., Plank, G., Burton, R., et al. (2010). Development of an anatomically detailed MRI-derived rabbit ventricular model and assessment of its impact on simulations of electrophysiological function. *American Journal of Physiology-Heart and Circulatory Physiology*, 298(2):699–718.

Captur, G., Flett, A., Jacoby, D., and Moon, J. (2013). Left ventricular non-noncompaction: The mitral valve prolapse of the 21st century? *International Journal of Cardiology*, 164(1):3–6.

Captur, G., Syrris, P., Obianyo, C., Limongelli, G., and Moon, J. C. (2015). Formation and malformation of cardiac trabeculae: Biological basis, clinical significance, and special yield of magnetic resonance imaging in assessment. *Canadian Journal of Cardiology*, 31(11):1325–1337.

Captur, G., Wilson, R., Bennett, M. F., Luxán, G., Nasis, A., la Pompa, J. L., Moon, J. C., and Mohun, T. J. (2016). Morphogenesis of myocardial trabeculae in the mouse embryo. *Journal of Anatomy*, 229(2):314–325.

Cerqueira, M. D., Weissman, N. J., Dilsizian, V., et al. (2002). Standardized myocardial segmentation and nomenclature for tomographic imaging of the heart a statement for healthcare professionals from the cardiac imaging committee of the Council on Clinical Cardiology of the American Heart Association. *Circulation*, 105(4):539–542.

Chen, Y., Vaccarino, V., Williams, C. S., Butler, J., Berkman, L. F., and Krumholz, H. M. (1999). Risk factors for heart failure in the elderly: A prospective community-based study. *The American Journal of Medicine*, 106(6):605–612.

Chin, T., Perloff, J., Williams, R., Jue, K., and Mohrmann, R. (1990). Isolated noncompaction of left ventricular myocardium. A study of eight cases. *Circulation*, 82(2):507–513.

CIBC (2015). Seg3D: Volumetric image segmentation and visualization. Scientific Computing and Imaging Institute (SCI), Downloaded from: http://www.seg3d.org [online: 10/08/2015].

Dawson, D. K., Maceira, A. M., Raj, V. J., Graham, C., Pennell, D. J., and Kilner, P. J. (2011). Regional thicknesses and thickening of compacted and trabeculated myocardial layers of the normal left ventricle studied by cardiovascular magnetic resonance. *Circulation: Cardiovascular Imaging*, 4(2):139–146.

de Boer, B. A., van den Berg, G., de Boer, P. A. J., Moorman, A. F. M., and Ruijter, J. M. (2012). Growth of the developing mouse heart: An interactive qualitative and quantitative 3D atlas. *Developmental Biology*, 368(2):203–213.

De Craene, M., Tobon-Gomez, C., Butakoff, C., et al. (2012). Temporal diffeomorphic free form deformation (TDFFD) applied to motion and deformation quantification of tagged MRI sequences. In *Proceedings of the Second International Conference on Statistical Atlases and Computational Models of the Heart: Imaging and Modelling Challenges, LNCS 7085*, pages 68–77.

Desbrun, M., Meyer, M., and Alliez, P. (2002). Intrinsic parameterizations of surface meshes. In *Computer Graphics Forum*, volume 21(3), pages 209–218.

Dores, H., Freitas, A., Malhotra, A., Mendes, M., and Sharma, S. (2015). The hearts of competitive athletes: An up-to-date overview

of exercise-induced cardiac adaptations. *Revista Portuguesa de Cardiologia*, 34(1):51–64.

Eggen, M. D., Swingen, C. M., and Iaizzo, P. A. (2012). Ex vivo diffusion tensor MRI of human hearts: Relative effects of specimen decomposition. *Magnetic Resonance in Medicine*, 67(6):1703–1709.

Floater, M. S. and Hormann, K. (2005). Surface parameterization: A tutorial and survey. In *Advances in Multiresolution for Geometric Modelling, Mathematics and Visualization*, pages 157–186.

Foroutan-Pour, K., Dutilleul, P., and Smith, D. (1999). Advances in the implementation of the box-counting method of fractal dimension estimation. *Applied Mathematics and Computation*, 105(2):195–210.

Freedom, R. M., Yoo, S. J., Perrin, D., Taylor, G., Petersen, S., and Anderson, R. H. (2005). The morphological spectrum of ventricular noncompaction. *Cardiology in the Young*, 15(4):345–364.

Friedberg, M., Ursell, P., and Silverman, N. (2005). Isomerism of the left atrial appendage associated with ventricular noncompaction. *The American Journal of Cardiology*, 96(7):985–990.

Gabrielli, L., Bijnens, B. H., Butakoff, C., Duchateau, N., Montserrat, S., Merino, B., Gutierrez, J., Paré, C., Mont, L., Brugada, J., and Sitges, M. (2014). Atrial functional and geometrical remodeling in highly trained male athletes: For better or worse? *European Journal of Applied Physiology*, 114(6):1143–1152.

Ganame, J., Ayres, N., and Pignatelli, R. (2006). Left ventricular noncompaction, a recently recognized form of cardiomyopathy. *Insuficiencia Cardíaca*, 1:119–124.

Gao, M., Chen, C., Zhang, S., et al. (2013). Segmenting the papillary muscles and the trabeculae from high resolution cardiac CT through restoration of topological handles. In *Proceedings of the Conference on*

*Information Processing in Medical Imaging, LNCS 7917*, pages 184–195.

Gao, M., Chen, C., Zhang, S., Qian, Z., Vannan, M., Rinehart, S., Metaxas, D., and Axel, L. (2014). Morphological analysis of the papillary muscles and the trabeculae. In *Biomedical Imaging (ISBI), 2014 IEEE 11th International Symposium on*, pages 373–376.

Garcia-Barnes, J., Gil, D., Badiella, L., et al. (2010). A normalized framework for the design of feature spaces assessing the left ventricular function. *IEEE Transactions on Medical Imaging*, 29(3):733–745.

Gati, S., Chandra, N., Bennett, R. L., Reed, M., Kervio, G., Panoulas, V. F., Ghani, S., Sheikh, N., Zaidi, A., Wilson, M., et al. (2013). Increased left ventricular trabeculation in highly trained athletes: Do we need more stringent criteria for the diagnosis of left ventricular noncompaction in athletes? *Heart*, 99(6):401–408.

Gati, S., Papadakis, M., Papamichael, N. D., Zaidi, A., Sheikh, N., Reed, M., Sharma, R., Thilaganathan, B., and Sharma, S. (2014). Reversible de novo left ventricular trabeculations in pregnant women: Implications for the diagnosis of left ventricular noncompaction in low-risk populations. *Circulation*, 130(6):475–483.

Gilbert, K., Lam, H., Pontré, B., Cowan, B., Occleshaw, C., Liu, J., and Young, A. (2015). An interactive tool for rapid biventricular analysis of congenital heart disease. *Clinical Physiology and Functional Imaging*.

Gledhill, N., Cox, D., and Jamnik, R. (1994). Endurance athletes' stroke volume does not plateau: Major advantage is diastolic function. *Medicine and Science in Sports and Exercise*, 26(9):1116–1121.

Goff, R. P., Spencer, J. H., and Iaizzo, P. A. (2015). MRI Reconstructions of human phrenic nerve anatomy and computational modeling of cryoballoon ablative therapy. *Annals of Biomedical Engineering*, pages 1–10.

Goñi, J., Sporns, O., Cheng, H., Aznárez-Sanado, M., Wang, Y., Josa, S., Arrondo, G., Mathews, V. P., Hummer, T. A., Kronenberger, W. G., et al. (2013). Robust estimation of fractal measures for characterizing the structural complexity of the human brain: Optimization and reproducibility. *NeuroImage*, 83:646–657.

Grant, R. (1926). An unusual anomaly of the coronary vessels in the malformed heart of a child. *Heart*, 13:273–283.

Gray, H. (1918). *Anatomy of the human body*. Lea & Febiger.

Gu, X., Wang, Y., Chan, T. F., et al. (2004). Genus zero surface conformal mapping and its application to brain surface mapping. *IEEE Transactions on Medical Imaging*, 23(8):949–958.

Haker, S., Angenent, S., Tannenbaum, A. R., et al. (2000). Conformal surface parameterization for texture mapping. *IEEE Transactions on Visualization and Computer Graphics*, 6(2):181–189.

Hall, C. (2005). NT-ProBNP: The mechanism behind the marker. *Journal of Cardiac Failure*, 11(5):S81–S83.

Hentschel, H. and Procaccia, I. (1983). The infinite number of generalized dimensions of fractals and strange attractors. *Physica D: Nonlinear Phenomena*, 8(3):435–444.

Hurdal, M. K., Stephenson, K., Bowers, P., et al. (2000). Coordinate systems for conformal cerebellar flat maps. *NeuroImage*, 11(5):S467.

Jelinek, H. F., Jones, C. L., Warfel, M. D., Lucas, C., Depardieu, C., and Aurel, G. (2006). Understanding fractal analysis? The case of fractal linguistics. *Complexus*, 3(1-3):66–73.

Jin, M., Kim, J., Luo, F., and Gu, X. (2008). Discrete surface ricci flow. *IEEE Transactions on Visualization and Computer Graphics*, 14(5):1030–1043.

Joshi, A. A., Shattuck, D. W., Thompson, P. M., et al. (2007). Surface-constrained volumetric brain registration using harmonic mappings. *IEEE Transactions on Medical Imaging*, 26(12):1657–1669.

Jost, C. H. A., Connolly, H. M., O'Leary, P. W., Warnes, C. A., Tajik, A. J., and Seward, J. B. (2005). Left heart lesions in patients with Ebstein anomaly. In *Mayo Clinic Proceedings*, volume 80, pages 361–368.

Kannel, W. (1987). Epidemiology and prevention of cardiac failure: Framingham study insights. *European Heart Journal*, 8(suppl F):23–26.

Karavides, T., Leung, K. E., Paclik, P., Hendriks, E. A., and Bosch, J. G. (2010). Database guided detection of anatomical landmark points in 3D images of the heart. In *SPIE Medical Imaging*, pages 76234Q–76234Q.

Karim, R., Ma, Y., Jang, M., et al. (2014). Surface flattening of the human left atrium and proof-of-concept clinical applications. *Computerized Medical Imaging and Graphics*, 38(4):251–266.

Karperien, A. L. and Jelinek, H. F. (2016). Box-counting fractal analysis: A primer for the clinician. In *The Fractal Geometry of the Brain*, pages 13–43. Springer.

Kharevych, L., Springborn, B., and Schröder, P. (2006). Discrete conformal mappings via circle patterns. *ACM Transactions on Graphics*, 25(2):412–438.

Kohli, S., Pantazis, A., Shah, J., Adeyemi, B., Jackson, G., McKenna, W., Sharma, S., and Elliott, P. (2008). Diagnosis of left-ventricular non-compaction in patients with left-ventricular systolic dysfunction: Time for a reappraisal of diagnostic criteria? *European Heart Journal*, 29(1):89–95.

Kovacevic-Preradovic, T., Jenni, R., Oechslin, E., Noll, G., Seifert, B., and Attenhofer Jost, C. (2008). Isolated left ventricular noncompaction

as a cause for heart failure and heart transplantation: A single center experience. *Cardiology*, 112(2):158–164.

Laboratory, T. V. H. (2015). [online: 10/08/2015].

Lévy, B., Petitjean, S., Ray, N., et al. (2002). Least squares conformal maps for automatic texture atlas generation. In *ACM Transactions on Graphics*, volume 21(3), pages 362–371.

Lilje, C., Rázek, V., Joyce, J. J., Rau, T., Finckh, B. F., Weiss, F., Habermann, C. R., Rice, J. C., and Weil, J. (2006). Complications of non-compaction of the left ventricular myocardium in a paediatric population: A prospective study. *European Heart Journal*, 27(15):1855–1860.

Lorensen, W. E. and Cline, H. E. (1987). Marching cubes: A high resolution 3D surface construction algorithm. In *ACM Siggraph Computer Graphics*, volume 21, pages 163–169.

Lu, X., Georgescu, B., Littmann, A., Mueller, E., and Comaniciu, D. (2009). Discriminative joint context for automatic landmark set detection from a single cardiac MR long axis slice. In *Proceedings of Conference on Functional Imaging and Modeling of the Heart, LNCS 5528*, pages 457–465.

Melchiorre, K., Sharma, R., and Thilaganathan, B. (2012). Cardiac structure and function in normal pregnancy. *Current Opinion in Obstetrics and Gynecology*, 24(6):413–421.

Miller, C. E. and Wong, C. L. (2000). Trabeculated embryonic myocardium shows rapid stress relaxation and non-quasi-linear viscoelastic behavior. *Journal of Biomechanics*, 33(5):615–622.

Misra, C. and Garg, V. (2013). Compacting the heart with Notch. *Nature Medicine*, 19(2):133.

Mohun, T. J. and Weninger, W. J. (2012). Embedding embryos for high-resolution episcopic microscopy (HREM). *Cold Spring Harbor Protocols*, 2012(6):pdb–prot069583.

Ng, T. C., Gu, X., and Lui, L. M. (2013). Computing extremal Teichmüller map of multiply-connected domains via Beltrami holomorphic flow. *Journal of Scientific Computing*, pages 1–27.

Oechslin, E. and Jenni, R. (2011). Left ventricular non-compaction revisited: A distinct phenotype with genetic heterogeneity? *European Heart Journal*, 32(12):1446–1456.

Oechslin, E. N., Attenhofer Jost, C. H., Rojas, J. R., Kaufmann, P. A., and Jenni, R. (2000). Long-term follow-up of 34 adults with isolated left ventricular noncompaction: A distinct cardiomyopathy with poor prognosis. *Journal of the American College of Cardiology*, 36(2):493–500.

Paun, B., Bijnens, B., and Butakoff, C. (2015). Subject independent reference frame for the left ventricular detailed cardiac anatomy. In *Proceedings of Conference on Functional Imaging and Modeling of the Hear, LNCS 9126*, pages 240–247.

Paun, B., Bijnens, B., Iles, T., Iaizzo, P. A., and Butakoff, C. (2017). Patient independent representation of the detailed cardiac ventricular anatomy. *Medical Image Analysis*, 35:270–287.

Penela, D., Bijnens, B., Doltra, A., Silva, E., Castel, M. A., Berruezo, A., Mont, L., Weidemann, F., Brugada, J., and Sitges, M. (2013). Noncompaction cardiomyopathy is associated with mechanical dyssynchrony: A potential underlying mechanism for favorable response to cardiac resynchronization therapy. *Journal of Cardiac Failure*, 19(2):80–86.

Peshkovsky, C., Totong, R., and Yelon, D. (2011). Dependence of cardiac trabeculation on neuregulin signaling and blood flow in zebrafish. *Developmental Dynamics*, 240(2):446–456.

Peters, D. C., Ennis, D. B., and McVeigh, E. R. (2002). High-resolution MRI of cardiac function with projection reconstruction and steady-state free precession. *Magnetic Resonance in Medicine*, 48(1):82–88.

Pinkall, U. and Polthier, K. (1993). Computing discrete minimal surfaces and their conjugates. *Experimental Mathematics*, 2(1):15–36.

Pluim, B. M., Zwinderman, A. H., van der Laarse, A., and van der Wall, E. E. (2000). The athlete s heart : A meta-analysis of cardiac structure and function. *Circulation*, 101(3):336–344.

Redfield, M. M., Rodeheffer, R. J., Jacobsen, S. J., Mahoney, D. W., Bailey, K. R., and Burnett, J. C. (2004). Plasma brain natriuretic peptide to detect preclinical ventricular systolic or diastolic dysfunction a community-based study. *Circulation*, 109(25):3176–3181.

Riemann, B. and Wilkins, D. R. (1851). *Grundlagen für eine allgemeine Theorie der Functionen einer veränderlichen complexen Grösse*. PhD thesis, EA Huth.

Ritter, M., Oechslin, E., Sütsch, G., Attenhofer, C., Schneider, J., and Jenni, R. (1997). Isolated noncompaction of the myocardium in adults. In *Mayo Clinic Proceedings*, volume 72, pages 26–31.

Roberts, W. C., Karia, S. J., Ko, J. M., Grayburn, P. A., George, B. A., Hall, S. A., Kuiper, J. J., and Meyer, D. M. (2011). Examination of isolated ventricular noncompaction (hypertrabeculation) as a distinct entity in adults. *The American Journal of Cardiology*, 108(5):747–752.

Russell, D. A., Hanson, J. D., and Ott, E. (1980). Dimension of strange attractors. *Physical Review Letters*, 45(14):1175–1178.

Samsa, L. A., Yang, B., and Liu, J. (2013). Embryonic cardiac chamber maturation: Trabeculation, conduction, and cardiomyocyte proliferation. In *American Journal of Medical Genetics Part C: Seminars in Medical Genetics*, volume 163, pages 157–168.

Sanghavi, M. and Rutherford, J. D. (2014). Cardiovascular physiology of pregnancy. *Circulation*, 130(12):1003–1008.

Sarma, R., Chana, A., and Elkayam, U. (2010). Left ventricular noncompaction. *Progress in Cardiovascular Diseases*, 52(4):264–273.

Sawhney, R. and Crane, K. (2017). Boundary first flattening. *arXiv preprint arXiv:1704.06873*.

Schroeder, W. M., Martin, K., and Lorensen, B. (2006). *The visualization toolkit: An object oriented approach to 3D graphics 3rd edition*. Kitware Inc.

Sedmera, D., Pexieder, T., Rychterova, V., Hu, N., and Clark, E. B. (1999). Remodeling of chick embryonic ventricular myoarchitecture under experimentally changed loading conditions. *The Anatomical Record*, 254(2):238–252.

Sedmera, D., Pexieder, T., Vuillemin, M., Thompson, R. P., and Anderson, R. H. (2000). Developmental patterning of the myocardium. *The Anatomical Record*, 258(4):319–337.

Sheffer, A., Praun, E., and Rose, K. (2006). Mesh parameterization methods and their applications. *Foundations and Trends in Computer Graphics and Vision*, 2(2):105–171.

Soto-Iglesias, D., Butakoff, C., Andreu, D., et al. (2013). Evaluation of different mapping techniques for the integration of electro-anatomical voltage and imaging data of the left ventricle. In *Proceedings of Conference on Functional Imaging and Modeling of the Hear, LNCS 7945*, pages 391–399.

Squillacote, A. H. (2008). *The ParaView guide: A parallel visualization application*. Kitware Inc., 3rd edition.

Staudt, D. W., Liu, J., Thorn, K. S., Stuurman, N., Liebling, M., and Stainier, D. Y. R. (2014). High-resolution imaging of cardiomyocyte

behavior reveals two distinct steps in ventricular trabeculation. *Development*, 141(3):585–593.

Stöllberger, C. and Finsterer, J. (2004). Left ventricular hypertrabeculation/noncompaction. *Journal of the American Society of Echocardiography*, 17(1):91–100.

Tizón-Marcos, H. (2012). Trabeculated myocardium in healthy adults: A first step in understanding the diagnosis of non-compaction.

Tobon-Gomez, C., Zuluaga, M. A., Chubb, H., Williams, S. E., Butakoff, C., Karim, R., Camara, O., Ourselin, S., and Rhode, K. (2015). Standardised unfold map of the left atrium: Regional definition for multimodal image analysis. *Journal of Cardiovascular Magnetic Resonance*, 17(1):1–3.

Towbin, J. (2010). Left ventricular noncompaction: A new form of heart failure. *Heart Failure Clinics*, 6(4):453–469.

Tutte, W. T. (1963). How to draw a graph. *Proceedings of the London Mathematical Society*, 13(3):743–768.

Vera, S., González Ballester, M. A., and Gil, D. (2014). Anatomical parameterization for volumetric meshing of the liver. In *Society of Photo-Optical Instrumentation Engineers (SPIE) Conference Series*, volume 9036, page 05.

Wang, Y., Shi, J., Yin, X., et al. (2012). Brain surface conformal parameterization with the Ricci flow. *IEEE Transactions on Medical Imaging*, 31(2):251–264.

Weninger, W. J., Geyer, S. H., Mohun, T. J., Rasskin-Gutman, D., Matsui, T., Ribeiro, I., Costa, L. d. F., Izpisua-Belmonte, J. C., and Müller, G. B. (2006). High-resolution episcopic microscopy: A rapid technique for high detailed 3D analysis of gene activity in the context of tissue architecture and morphology. *Anatomy and embryology*, 211(3):213–221.

Wessels, A. and Sedmera, D. (2003). Developmental anatomy of the heart: A tale of mice and man. *Physiological Genomics*, 15(3):165–176.

Wilcox, B. R., Cook, A. C., and Anderson, R. H. (2004). Anatomy of the cardiac chambers. In *Surgical anatomy of the heart*, pages 11–44.

Yezzi, A. J. and Prince, J. L. (2003). An Eulerian PDE approach for computing tissue thickness. *IEEE Transactions on Medical Imaging*, 22(10):1332–1339.

Yoo, T. S., Ackerman, M. J., Lorensen, W. E., Schroeder, W., Chalana, V., Aylward, S., Metaxas, D., and Whitaker, R. (2002). Engineering and algorithm design for an image processing API: A technical report on ITK - the insight toolkit. *Studies in health technology and informatics*, pages 586–592.

Young, A. A., Crossman, D. J., Ruygrok, P. N., and Cannell, M. B. (2011). Mapping system for coregistration of cardiac MRI and ex vivo tissue sampling. *Journal of Magnetic Resonance Imaging*, 34(5):1065–1071.

Young, A. A., French, B. A., Yang, Z., Cowan, B. R., Gilson, W. D., Berr, S. S., Kramer, C. M., and Epstein, F. H. (2006). Reperfused myocardial infarction in mice: 3D mapping of late gadolinium enhancement and strain. *Journal of Cardiovascular Magnetic Resonance*, 8(5):685–692.

Zhang, X., Cowan, B. R., Bluemke, D. A., Finn, J. P., Fonseca, C. G., Kadish, A. H., Lee, D. C., Lima, J. A. C., Suinesiaputra, A., Young, A. A., et al. (2014). Atlas-based quantification of cardiac remodeling due to myocardial infarction. *PLoS ONE*, 9(10):e110243.

Zheng, Y., Georgescu, B., and Comaniciu, D. (2009a). Marginal space learning for efficient detection of 2D/3D anatomical structures in medical images. In *Information Processing in Medical Imaging*, volume 5636, pages 411–422.

Zheng, Y., Georgescu, B., Ling, H., Zhou, S. K., Scheuering, M., and Comaniciu, D. (2009b). Constrained marginal space learning for efficient 3D anatomical structure detection in medical images. In *IEEE Conference on Computer Vision and Pattern Recognition*, pages 194–201.